Heat and Flow Phenomena in Liquid-Filled Thin Porous Materials: Design and Visualization Techniques

Tiara Nur Pratiwi
18703191

Department of Food and Energy Systems Science
Graduate School of Bio-Applications and Systems Engineering
Tokyo University of Agriculture and Technology
2023

Table of contents

List of Figures

List of Tables

Chapter 1: Introduction

Abbreviation

CA	Cellulose acetate
CNT	Carbon nanotubes
DMF	Dimethylformamide
GCS	Graphitic carbon spheres
HFP	Hexafluoropropylene
LED	Light-emitting diode
MMM	Mixed matrix membrane
MOF	Metal organic framework
MRI	Magnetic resonance imaging
NIR	Near-infrared
NMR	Nuclear magnetic resonance
OCT	Optical coherence tomography
PDA	Polydopamine
PES	Polyethersulfone
PI	Polyimide
PP	Polypropylene
PS	Polystyrene
PTT	Photothermal therapy
PVA	Polyvinyl alcohol
PVDF	Polyvinylidene fluoride

1.1 Preface

A study on the design of thin porous materials holds significant importance due to its wide range of applications in various technological applications such as separation, catalysis, energy storage, and sensing. By carefully designing the structure, pores distribution, and surface properties of thin porous materials, one can optimize their performance for specific applications, leading to improved efficiency, selectivity, and functionality [1,2]. Research incorporating thin porous media and particles has made significant progress in recent years. The combination of thin porous materials and particles has resulted in enhanced functionalities and improved performance in areas such as in mixed-matrix membranes [3,4], anti-fouling membranes [5–10], high quality paper production [11], anti-bacterial face mask [12], and photothermal membrane [13]. A simple, inexpensive, and integrated method to incorporate particles into a porous material matrix is therefore essential for the advancement of many technologies.

The development of non-invasive visualization techniques to monitor liquid flow in thin porous media is crucial in various scientific and engineering fields such as inkjet printing [14], development of smart-fabric [15], microfluidic paper-based analytical devices [16], and many more. It allows for the exploration of novel phenomena at the micro-scale, enabling the development of innovative materials with unprecedented capabilities. Many studies have proposed "visualization" techniques to monitor liquid flow in thin porous media, such as by using X-ray tomography [15], high speed camera [17], nuclear magnetic resonance (NMR) [18], magnetic resonance imaging (MRI) [19], fluorescence microscopy [20], optical coherence tomography (OCT) [21], etc. However, there is only a little amount of study on liquid movement in porous media under elevated temperature. Of which, to the best of our knowledge, no studies have succeeded in visualizing liquid movement in the depth direction of a porous media at an elevated temperature. An increase in temperature will affect the liquid flow in porous media such as reducing the viscosity of the liquid, induce phase change, enhance liquid diffusion, and may cause structure change in the porous media. Studying liquid flow at an elevated temperature by means of liquid flow visualization in porous media is therefore essential for understanding fluid behavior, heat and mass transfer prediction, performance optimization and for further development of advanced materials and technologies.

This chapter summarizes some key aspects on the design strategy of porous materials and methods for incorporation of particles into the matrix of thin porous materials along with the challenges needed to be addressed for each method. The state of the art insight on the

study of liquid flow movement in porous media is also summarized along with a review on the existing visualization methods. At the end of this chapter, the significance of this dissertation will be elaborated.

1.2 Definition of thin porous materials

A thin porous material is defined as a solid matrix that has void or pores whose thickness is much smaller than their lateral dimension (approximately one order of magnitude greater than its mean pore size) [1,2]. Research focused on thin porous material, including theoretical, numerical, and experimental, holds significant value across diverse engineering and environmental applications. Examples of thin porous material include membranes, biological materials, papers, textiles, filters, fuel cells, and thin composites [2]. In the present study, a fibrous and porous materials with a thickness of several hundred micro meter and a lateral dimension in few cm order will be of focus.

1.3 Some types of thin porous material and its application

Plant leaf is an example of thin porous material that can be readily found in nature. Leaf comprised of a solid matrix of cells and veins and contains tiny pores (a few micrometers) called stomata, which allow for gas exchange between the plant and its environment [22]. Leaf can be further processed to produce consumer products such as tea, tobacco products, natural dyes, essential oil, natural mulch to retain water moisture in gardening, and many more.

Paper is another important example of a thin porous material. Paper is made up of bonded cellulose fibers, typically derived from wood pulp. Besides for applications such as writing, printing, and food packaging, paper has attracted a growing interest for application as a microfluidic analytical device due to its low cost, porous structure, ease of surface modification, and biocompatibility [16].

Thin porous material in the form of membranes have found applications in numerous industries. Biopolymer membrane is a thin flexible sheet made from natural polymer such as cellulose, chitosan, carrageenan, or alginate [23–28] . Its application ranges from food packaging [29–33], wound dressing [24,25], and drug delivery [34,35]. The use of natural polymer for a wide range of applications of thin porous material is attractive due to its biodegradability, biocompatibility, and sustainability. Despite its high carbon footprint, the use of synthetic polymer as membrane matrix remains popular due to its versatility (can be engineered to have a wide range of properties, i.e. chemical and heat resistance), stability (can withstand harsher environmental conditions without losing their properties), and

compatibility with existing materials (can be easily integrated into existing products and systems). Polyvinylidene fluoride (PVDF), polyethersulfone (PES), and polyimide (PI) are some examples of widely used synthetic polymer for membranes application owing to their excellent thermal and mechanical properties, permeability, and good chemical resistance [36–38].

Since its first discovery in 1991 by Japanese physicist Sumio Iijima [39], carbon nanotube (CNT) has attracted many interest. Buckypaper is an example of a CNT-based membrane. Buckypaper is a thin sheet or film made from carbon nanotubes (CNTs) arranged in a random or aligned network. Buckypaper membranes demonstrate the ability to effectively separate water pollutants, encompassing both polar and non-polar contaminants. This remarkable capability is accompanied by a notable water permeability feature, showing a promising potential for implementation of buckypaper at the industry [40].

Early research on ceramic use as a thin membrane for gas separation dates back to mid-1980s [41]. Inorganic materials, such as aluminum oxide, titanium dioxide, and zirconium dioxides, are utilized to create ceramic thin membranes. These types of membranes are commonly used in operations that involve liquid filtration, including wastewater and water treatment, as well as in separations that involve harsh chemicals like strong solvents and acids [42,43]. Due to their exceptional thermal stability, ceramic thin membranes are ideal for high-temperature membrane operations [43].

Metal organic frameworks (MOFs) are organic-inorganic hybrid crystalline porous materials that have an extraordinarily large internal surface area [44–46]. Early synthesis of MOF was conducted in mid-1990s [47]. MOF thin membranes have potential applications in gas separation, water purification, electrochemical energy conservation, and catalysis [45,46]. Multifunctionality, high drug loading capacity, and adjustable pore size made some biocompatible MOFs a suitable candidate for drug delivery [45,46].

A membrane matrix can be combined with other materials such as particles to create a composite. A well-known example is a mixed matrix membrane (MMM). MMM is a type of membrane that combines two different materials, typically a polymer and a filler, to create a membrane with improved properties for separation applications. The common selection for filler includes zeolite, carbon molecular sieves, and other nano-sized particles [3]. Another example is photothermal membrane made by incorporating photothermal particles into a membrane matrix [13]. Photothermal particles can efficiently absorb light and convert it into heat. The heat generated by the photothermal membranes can be harnessed for various

applications, such as photothermal therapy (PTT) for cancer treatment [48], water desalination and purification [49–57], ice phobic surface [58], and antibacterial surface [59].

1.4 Design of thin porous materials

Some engineered thin porous materials draw inspiration from the intricate structures and functionalities found in natural systems. These materials mimic the design principles observed in biological organisms and natural surfaces to achieve unique properties and performance. Researchers have developed thin porous material that exhibit remarkable characteristics such as superwettability, antifouling capabilities, and enhanced mass transfer [1,2]. Depending on the purpose and application of the porous material, there are some key aspects that should be considered in the design such as, material selection, desired pore size distribution, desired surface properties, and other functionalities. The summary of the design in thin porous materials can be found in Figure 1.1.

Material selection. Selection of precursor materials to fabricate thin porous material is important to yield a product that has the desired chemical compatibility, mechanical strength, thermal stability, and desired surface properties.

Hierarchical pore size distribution. The pore size distribution and porosity of porous materials have a significant impact on their susceptibility to fouling. To improve the antifouling performance of the porous material, it is important to create hierarchical structures that feature a uniform distribution of pore sizes on their surfaces [2]. Furthermore, hierarchical pore structure can optimize the adsorption and transport properties of materials [1]. Natural porous structures such as butterfly wings, leaf, and woods becomes a source of inspiration for hierarchical porous design [60]. Some methods to create a hierarchical pore size includes templating, sol-gel, phase separation, zeolitization process, supercritical fluids, freeze drying, breath figures, and selective leaching [60].

Modification of surface properties. Surface properties of porous media determines the interaction between the porous media and liquid which contains fouling agents and contaminants. Improvement on the wettability property (i.e. superhydrophobicity and superhydrophilicity) can help to prevent fouling and improve transport and life-time of porous materials. Lotus leaf has served as an inspiration for a superhydrophobic substrate while fish scale inspired fabrication of superhydrophilic substrate [2]. Some methods to modify surface property of porous materials are listed in Table 1.1.

Table 1.1 Methods for surface modifications of some thin porous materials

Membrane matrix	Fabrication method	Target wettability	Key design features	Reference
Polypropylene (PP)	Plasma treatment, immersion in particle suspension	Superhydrophobic	Micro/nano structures by SiO_2 particles	[61]
Polyvinylidene fluoride (PVDF)	Delayed phase inversion	Superhydrophobic	Micro/ nano structures on membrane created by SiO_2	[62]
Some polymers	Chemical vapor deposition	Hydrophilic, hydrophobic	Micro/ nano structures on membrane	[63]
Polydimethylsiloxane (PDMS)	Bio-templating, layer by layer assembly	Hydrophilic	Microstructure from L. japonica and hydrophilic polymer layers	[64]
PVDF	Electrospinning	Superhydrophobic	PVDF nanospheres on PVDF fiber	[65]
Polyamide	3D printing and MOF growing	Superhydrophobic	Micro/nano structures from metal organic framework (MOF)	[66]

1.4.1 Particle incorporation in thin porous materials for enhanced functionalities

Addition of particles into thin porous materials aims to give or enhance specific properties on the materials to suit a certain application. For example, a polymeric membrane on its own have a general trade-off between permeability and selectivity for gas separation with an upper bound limit described in details by Robeson [67]. Particles such as zeolite and silica have permeability and selectivity properties lying far beyond the upper bound limits for polymer membranes. Addition of such particles into polymer matrix can achieve higher permeability, selectivity, or both, relative to polymer membrane without particles [3,4].

In water treatment field, addition of metal oxide particles such as TiO_2, Al_2O_3, SiO_2 are also found to enhance separation performance, improve anti-fouling properties of the membrane through self-cleaning or photocatalysis [5–10]. Additionally, for membranes made from partially biodegradable polymer such as cellulose acetate (CA), degradation of the membranes by microorganisms in water can happen. Addition of antibacterial particles such as silver nanoparticles is essential to ensure the longevity of the membranes [68].

Filler and pigment particles are added into paper to enhance certain characteristics such as opacity, brightness, printability, and the overall cost-effectiveness of the paper production process. The most frequently used filler in paper making includes kaolin or clay, talc, calcium carbonate, gypsum, and mica. Common types of pigment particles used to improve the optical property of paper includes TiO_2, $Al(OH)_3$ crystalline, SiO2, ZnO, and $BaSO_4$ particles [11].

TiO_2 is commonly utilized in the manufacture of face masks. It serves purposes such as enhancing stability against ultraviolet light, acting as a white colorant, or functioning as a matting agent. In response to COVID 19 pandemic, more textile companies are incorporating nanoparticles such as TiO_2, silver and graphene to give self-cleaning property and antibacterial effect [12].

On a more recent note, addition of photothermal particles into porous matrix has attracted considerable attention. The mechanism of photothermal conversion involves the following steps [13]:

1. Absorption of light: A photothermal material absorbs photons of light, which excite the electrons in the material's atoms to a higher energy state.
2. Conversion of light to heat: The excited electrons in the photothermal material then release their energy in the form of heat, which causes an increase in temperature in the material.
3. Thermal diffusion: The heat generated in the photothermal material diffuses into the surrounding environment through conduction or radiation.
4. Heat utilization: The heat generated by the photothermal material can be utilized for various applications.

One important application of photothermal membrane is photothermal therapy (PTT) for cancer treatment. The commonly used photothermal materials for cancer treatment are gold nanoparticles, carbon nanotubes, and graphene oxide. These materials have strong light absorption in the near-infrared (NIR) region, which is ideal for cancer treatment as NIR light can penetrate deep into tissue without causing damage. By using light-responsive

nanoparticles camouflaged with cell membranes, PTT reduces harm to healthy tissues, improves tumor delivery, and enhances the effectiveness of thermal ablation. The membrane matrix serves as a support for the photothermal material and also helps to control the release of the photothermal material. To increase the specificity of the treatment, the photothermal membranes can be modified with targeting ligands such as antibodies or peptides. These ligands can selectively bind to cancer cells, allowing the photothermal membranes to accumulate in the tumor. The photothermal membranes are activated by a light source such as a laser or a light-emitting diode (LED). The light source is typically applied externally to the body, allowing for non-invasive treatment. When the photothermal membrane is activated by the light source, the photothermal material heats up and generates hyperthermia, which can damage or kill cancer cells. This can lead to tumor shrinkage or destruction, depending on the severity of the cancer [48].

Photothermal membranes have also been studied for other potential use in energy conversion applications. The most used photothermal materials for energy conversion applications are carbon-based materials such as carbon nanotubes, graphene, and carbon black. These materials have strong light absorption in the UV, visible, and near-infrared regions, making them suitable for a wide range of light sources [13]. The heat generated by the photothermal membranes can be harnessed for various applications, such as water desalination and purification [49–57], ice phobic surface [58], and antibacterial surface [59]. The efficiency of the photothermal membranes depends on various factors such as the photothermal material used, the light source, and the membrane matrix. A schematic representation on photothermal conversion mechanism in a solar distillation membrane can be seen in Figure 1.2

Based on the types, photothermal particles can be classified into four categories: metallic, carbon-based, inorganic semiconductor, and polymeric particles [13]. Carbon-based photothermal particles is of interest due to its several advantages such as;

1. High photothermal conversion efficiency due to its black body like features
2. Biocompatibility
3. Versatility (can be easily functionalized)
4. Stability (generally more stable than metallic and inorganic particles which can undergo degradation or oxidation over time)
5. Cost-effectiveness

Some state-of-the-art studies on the use of carbon-based photothermal particles in polymer matrix for solar distillation purposes are summarized in Table 1.2.

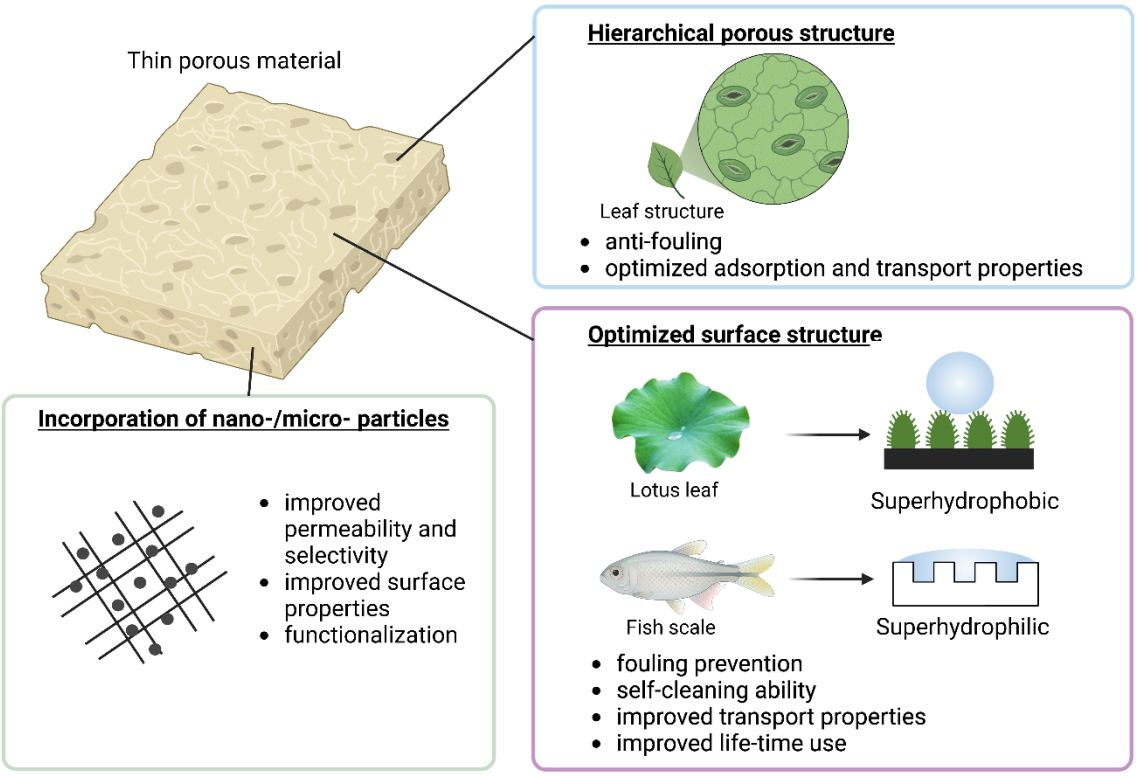

Figure 1.1 Overview of the design in thin porous materials

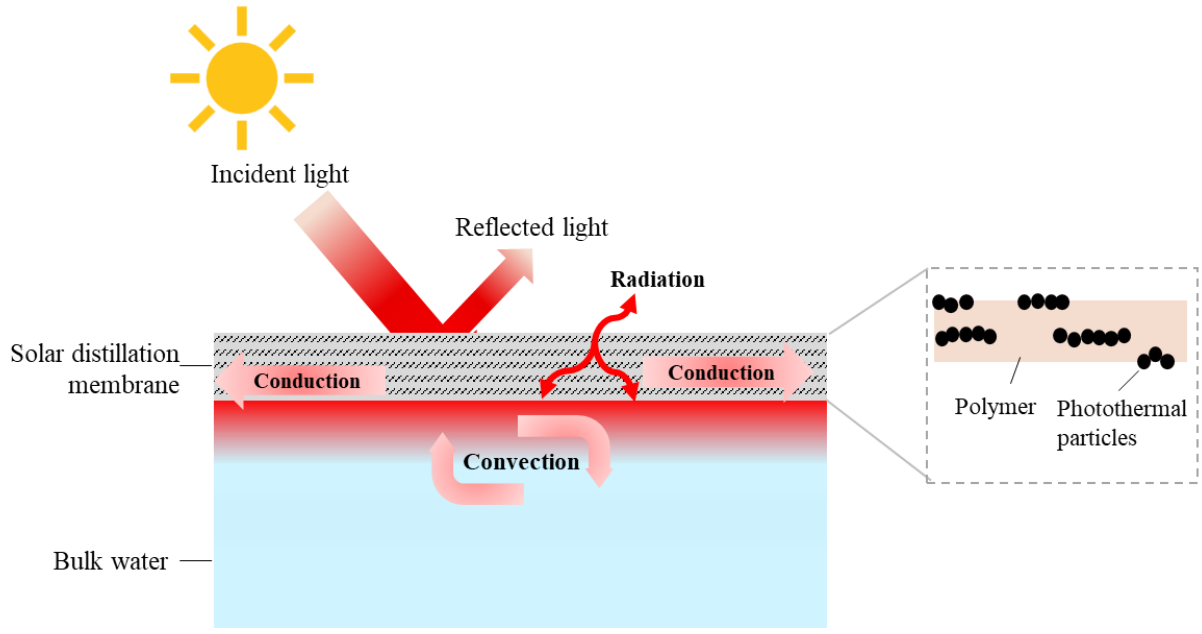

Figure 1. 2 Mechanism of photothermal conversion in a solar distillation membrane. Inspired from [13].

Table 1.2. State of the art studies on carbon-based photothermal membranes

Photothermal particles	**Matrix**	**Solar illumination (kWm^{-2})**	**Maximum surface temperature (^oC)**	**Photothermal efficiency (%)**	**Evaporation flux ($kg\ m^{-2}\ h^{-1}$)**	**Findings**	**Ref**
Diesel particulate matter	Cotton cloth, Polystyrene foam	1	43	91.75	1.5	Diesel soot particles help absorption of incident solar illumination, hydrophilicity of cotton cloth assists supply of water to produce constant steam, PS foam helps heat localization at the air-water interface	[50]
Candle soot	Cotton cloth, Polystyrene foam	1	44	80	1.19	Addition of PS foam as insulation to avoid heat loss to bulk water increases evaporation flux and photothermal efficiency	[49]

Table 1.2. State of the art studies on carbon-based photothermal membranes (cont.)

Carbon soot (from kerosene lamp)	Poly(ionic liquid) monolith	1	47.2	92.4	1.47	The mesoporous 3D architecture of the solar evaporator allows high localization and carbon soot gives excellent light absorption (92%)	[56]
Plant-derived carbon nanosphere	Polyvinyl alcohol (PVA) sponge	1	44.6	92.38	1.53	Indirect capillary pathway (no contact between the hot zone and bulk water) assists efficient solar distillation	[51]
Polydopamine (PDA)-derived graphitic carbon spheres	Polyvinylidene fluoride (PVDF) – Hexafluoropropylene (HFP)	1	45	92	1.29	Janus photothermal membrane design (top layer coated with hydrophobic photothermal material, bottom layer coated with hydrophilic PDA) yields efficient solar distillation	[69]

Table 1.2. State of the art studies on carbon-based photothermal membranes (cont.)

Candle soot	Cellulose membrane	1	44	75.1	1.16	Low thermal conductivity of the membrane localize heat at water surface and suppress heat loss to bulk water	[54]
Candle soot	Luffa sponge	1	36.2	64.79	1.30	Luffa sponge is hydrophilic and has low thermal conductivity which is important to maintain water flux and heat localization	[55]
Kerosene lantern soot	PVA	1	40.2	91.5	1.5	Optimization of the porous channel for fast water transportation is essential to improve photothermal performance	[57]

Table 1.2. State of the art studies on carbon-based photothermal membranes (cont.)

Candle soot	Adsorbent cotton	1	63.5	80.7	1.27	Introduction of 3D photothermal cone can separate the contact area between bulk water and the membrane to minimize heat loss and improve water evaporation rate	[53]
Diesel particulate matter	PVA-based hydrogel	1	42.1	-	3.01	3D microporous structure with vertically aligned water channel promote rapid water transport to the air-water interface	[52]

1.4.2 Methods to incorporate particles into thin porous materials

In this section, methods to incorporate particles into thin porous materials will be reviewed by using solar distillation membrane applications as a case study. Some known methods to incorporate carbon-based particles into polymer matrix is listed in Table 1.3. The schematic representation of the resulting photothermal membrane can be seen in Figure 1. 3. In method 1 and 6, the particles can be strongly embedded within the polymer matrix. However, achieving good dispersibility of carbon-based particles in polymer solution can be challenging. If the particle agglomerates or distribute unevenly, it can lead to inconsistent membrane properties and a reduced membrane performance. Chung et al [3] noted that particle sedimentation and agglomeration in polymer solution may result in inhomogeneous particles and polymer phases. The agglomeration of particles will cause pinholes that cannot be reached by polymer solution and form a defect. This may lead to inconsistent properties and reduced membrane performance. A way to mitigate this problem is by increasing the viscosity of the polymer to slow down particle sedimentation or by increasing the rate of membrane formation before particles settle at the bottom [3]. However, these two approaches may not be suitable for all kinds of purposes.

Method 2, 3, and 5 offer the most straightforward fabrication steps. However, it is feared that the resulting membrane will have only weak physical bonds with the photothermal particles. During the solar distillation process, there is a possibility of particles leaching or migrating out of the membrane. This can affect the membrane's stability and long-term performance.

In method 4, the control of the thickness of the polymer glue has not been properly addressed. The thickness of the glue layer may affect the optical properties of the photothermal layers. The glue layer may act as a medium that interacts with incoming light, such as by refracting or reflecting it. Controlling the thickness allows for optimizing light transmission or absorption, ensuring that the desired amount of light reaches the underlying light-absorbing surface and optimum light to heat conversion is reached.

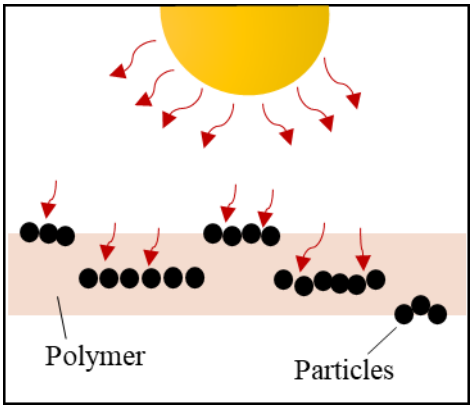

Method 1, 6

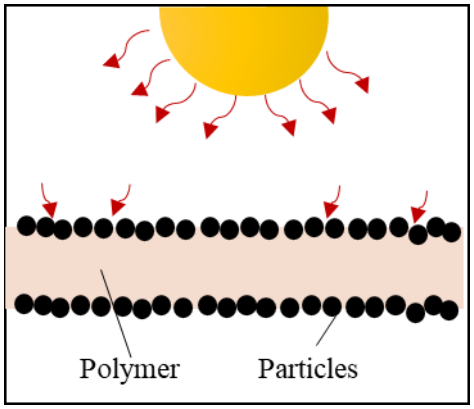

Method 2, 3, 5

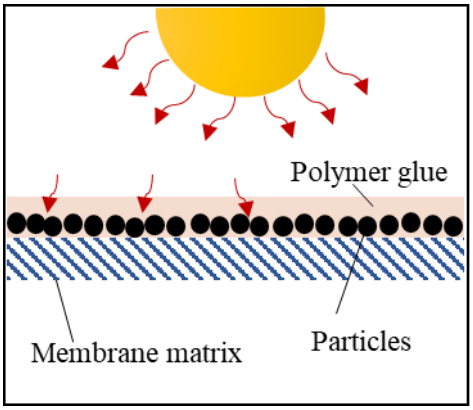

Method 4

Figure 1. 3 Illustration of the interaction between light and photothermal membrane resulting from different fabrication methods

Table 1.3. Some methods to incorporate carbon-based particles into thin porous matrix

No	Fabrication Method	Summary	Reference
1	Electrospinning of polymer-carbon-based particles suspension	1. Polymer (Polyvinylidene fluoride) is dissolved in solvents (Dimethyl formamide/Acetone) 2. Carbon-based particles (soot) is added to the solution 3. The good dispersibility of soot particles in polymer solution is achieved by adjusting the suitable polymer concentration and by continuous stirring for 6 hours 4. Electrospinning of the polymer-particle suspension	[70]
2	Dip coating of prefabricated porous membrane into carbon-based particles suspension	1. Collection of soot particles 2. Dispersion of soot particles into a solvent 3. The porous membrane is dipped into soot particles suspension and allowed to dry	[50,51,55]
3	Direct coating of prefabricated membrane by soot particles from a burning candle	1. A prefabricated membrane matrix (adsorbent cotton) is coated with soot particles by holding the membrane above a burning candle 2. Attaching the soot-embedded membrane to a 3D structure (foam sheet)	[49,53]
4	Direct coating of prefabricated membrane by soot particles from a burning candle and reinforcement by polymer glue	1. Selective deposition of soot particles from the inner flame of the candle on hydrophilic prefabricated membrane (cellulose filter paper) 2. Reinforcement of the bonding between soot particles and the membrane by applying polymer glue on the membrane surface	[54]

Table 1.3. Some methods to incorporate carbon-based particles into polymer matrix (cont.)

5	Attachment of carbon-based particles in a suspension by vacuum suction filtration	1. Fabrication of fibrous membrane by electrospinning 2. Fabrication of graphitic carbon-spheres (GCS) particles by hydrothermal method 3. Dispersing carbon-based particles in a solvent (nafion ethanol) by ultrasonication for 30 minutes 4. Attachment of carbon-based particles into the membrane by vacuum suction filtration	[69]
6	Salt-assisted method	1. Collection of soot particles 2. Mixing the carbon soot in polymer solution (Polyvinyl alcohol) by stirring 3. Adding the mixture dropwise onto a circular NaCl tablet and let to dry 4. NaCl tablet is removed by water, leaving the membrane film	[57]

1.5 Liquid flow in thin porous materials

Liquid flow in porous materials can occur in various natural and engineered systems, such as membranes, filters, papers, fabrics, microfluidic devices, and biological tissues. The behavior of liquid flow in thin porous materials is influenced by several factors, including the properties of the liquid (such as viscosity and surface tension), the characteristics of the porous material (such as pore size, thickness, and surface chemistry), and external conditions (such as temperature and humidity) [16].

1.5.1 Interaction between liquid and thin porous materials

The interactions between liquid and porous media can be classified into four fundamental phenomena, namely, impaction, spreading, penetration/ imbibition, and evaporation. The illustration of each phenomenon can be found in Figure 1.4.

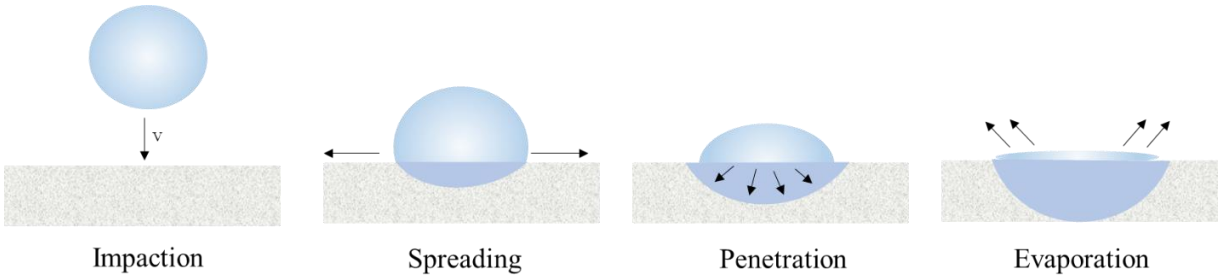

Figure 1. 4 Various interactions between liquid droplet (few millimeter) and porous media

1.5.1.1 Impaction

The study of droplet impact on porous surfaces has important practical applications in many fields. In environmental study for example, the infiltration of rain drops upon impaction on soil surface is important to understand nutrient and pollutant transport [71]. In agriculture, studying droplet impaction on plant leaves is crucial for optimizing spraying practices. This knowledge helps farmers and agricultural professionals make informed decisions on factors such as spray formulation, nozzle selection, application volume, plant species, and growth stage. By considering these factors, they can achieve desired outcomes while minimizing waste and reducing environmental impact. Additionally, studying droplet behavior on plant surfaces enhances our understanding of plant-environment interactions and how plants respond to external stimuli [78].

Related to air transport safety, study of droplet impact on canopy fabric is essential. Droplet impact on canopy fabric cannot be avoided in cases such as airdropping relief supplies or pilot ejection escape in rainy conditions. The droplet impact will have a great

effect on the parachute working process. In the alpine region, the presence of supercool droplets can lead to localized icing on the parachute, potentially resulting in recovery difficulties or airborne failure. Therefore, understanding the spreading characteristics of droplets on canopy fabric is important for improving the safety and effectiveness of these applications [72].

There are several factors that affect droplet dynamics upon impaction [73];

1. Surface temperature: Surface temperature plays a major role in droplet dynamics, particularly at super-heated or super-cooled temperatures.
2. Surface wettability: The wettability of the surface can affect the degree to which a droplet spreads or recoils upon impact. Weber number is a dimensionless parameter used to describe the ratio of inertial forces to surface tension forces in fluid mechanics. Weber number is often used to characterize the impact regime and predict droplet behavior. Weber number can be calculated by equation (1.3).

   $$\boldsymbol{We} = \frac{\boldsymbol{\rho v^2 L}}{\boldsymbol{\sigma}} \text{.....(1.3)}$$

   Where We is the weber number, ρ is the density of the fluid, v is the velocity of the fluid, L is a characteristic length, and σ is the surface tension of the fluid. When Weber number is higher than 200, wettability effect is secondary because of the increase in inertial force [74].
3. Impact velocity: The velocity at which the droplet impacts the surface can affect whether it spreads, splashes, rebounds or recedes. The behavior of a droplet upon impact is heavily influenced by its velocity during impact. At low impact velocities, the droplet tends to spread and create a thin film on the surface. As the impact velocity increases, the droplet can undergo a phenomenon called splashing, where small droplets are ejected from the main droplet due to the impact-induced deformation. At even higher velocities, the droplet may experience atomization, breaking up into numerous small droplets. The distribution of kinetic energy after impact also plays a role in determining the spreading and splashing behavior. Following the recoil from the surface, the droplet may exhibit rebounding depending on factors like surface wettability, temperature, and the remaining kinetic energy.
4. Droplet shape and volume. Generally, asymmetrical droplets require a higher impact velocity for rebounding.

5. Liquid properties: Properties such as liquid surface tension and viscosity can also play a role in determining the behavior of droplets upon impact. A higher viscosity can lead to a slower spreading regime and a shorter recoiling regime. The surface tension of the liquid also affects droplet dynamics, as it determines the contact angle between the droplet and surface.

1.5.1.2 Spreading

Liquid spreading in porous media is influenced by several factors such as, the wettability of the porous media, the surface tension of the liquid, pore size of the porous media, roughness of the porous media, and the temperature of the porous media. Contact angle is a commonly used parameter to assess the wettability of a surface, be it porous or not. The surface tension of a liquid is a measure of its cohesive forces, or how strongly its molecules are attracted to each other. There is an inverse relationship between surface tension and contact angle: as surface tension decreases, the contact angle increases. This means that liquids with lower surface tensions will tend to spread out more on a solid surface, while liquids with higher surface tensions will tend to bead up and form a larger contact angle with the solid surface [79]. In the case where particles are incorporated into the matrix of a porous media, the presence of nano-roughness on particles surface helps to increase the wettability of the porous media and eventually enhances the spreading behavior of drops on porous surfaces [75].

According to the modified model proposed by Adamson [76], there should be a critical temperature for spreading, which is a temperature above which the contact angle is zero. This critical temperature of wetting is predicted not to remain linear but rather to show increasing curvature with increasing temperature, with a final steep descent to $\theta = 0$ at a T_c.

1.5.1.3 Penetration and Imbibition

Flow of liquid through porous media has been explained by several models. One of them is Darcy's law. Darcy's Law is widely used in various fields, including hydrogeology, petroleum engineering, and civil engineering, to study groundwater flow, fluid transport in porous media, and the design and analysis of wells, aquifers, and subsurface systems. Mathematically, Darcy's Law can be expressed as:

$$\boldsymbol{q} = \frac{-\boldsymbol{k}\,\boldsymbol{A}\,\Delta\boldsymbol{h}}{\boldsymbol{\mu}\,\boldsymbol{L}} \qquad \text{.....(1.4)}$$

Where q is the volumetric flow rate of the fluid, A is the cross-sectional area through which the fluid flows, Δh is the hydraulic gradient, which represents the change in hydraulic head

over a given distance, k is the intrinsic permeability of the porous medium, which quantifies how easily the fluid can flow through it, L is the length of the flow path, and μ is the dynamic viscosity of the fluid [77].

Washburn equation is an empirical equation that relates the capillary pressure to the flow rate of a liquid through a porous medium. The equation assumes that the porous medium is homogeneous and isotropic, and that the pores are cylindrical and non-intersecting. When a liquid with a dynamic viscosity (η) and surface tension (γ) flows through a capillary with a pore radius (r), it will penetrate a distance (L) into the capillary. This relationship can be described by the following equation:

$$\boldsymbol{L = \sqrt{\frac{\gamma r t \cos\theta}{2\eta}}} \ldots\ldots\ldots (\mathbf{1.5})$$

θ represents the angle formed between the tube wall and the penetrating liquid [78]. The presence of internal cavity in porous media such as paper is partially responsible for the limited accuracy of the Washburn equation in real-world application [78].

When a droplet comes into contact with thin porous media such as paper, the liquid infiltration starts through several mechanisms: (1) spreading across the surface and filling surface pores and pits, (2) capillary transport within the pores and on the fiber surfaces, (3) capillary transport into the micro pores and cracks of the fibers, and (4) diffusion within the fiber structure [77].

The structure of thin porous materials plays a significant role in liquid penetration. Factors such as pore volume, pore size distribution, and tortuosity are crucial in determining fluid transport within thin porous materials. Additionally, the physico-chemical properties of the liquid can also influence this phenomenon. During the imbibition process, the liquid displaces air within the pores and cavities of thin porous media, leading to changes in light reflection as wetting transforms air-fiber interfaces into liquid-fiber interfaces [77].

Additionally, a study found that heat is released at the wetting front during capillary filling of cellulosic micro-substrates. Heat is released due to the solid-liquid interaction. The magnitude of the temperature rise is mainly influenced by the energetics of the imbibition compounds, particularly the acid-base interactions. Liquids that can be characterized as Lewis acids, such as water and chloroform, interact strongly with the basic cellulosic fibers, leading to a significant temperature rise. On the other hand, liquids that are energetically similar to cellulose, such as ethanol, exhibit a lower temperature rise [79].

1.5.1.4 Evaporation

Evaporation rate of liquid from porous media is affected by temperature, relative humidity (RH), droplet size, wetting properties of the porous media, and porosity [80]. Capillary action is found to accelerate evaporation process of liquid in porous media through distribution of liquid over a wide area of porous media [81]. Study on the evaporation profile of liquid from porous media can give insight into several drying profile that is important to understanding moisture removal process, assessing drying efficiency, determining product quality, and optimizing drying conditions.

The study on evaporation of water from glass beads describes three stages of evaporation: the constant rate period, characterized by shrinking evaporating patches (a region where evaporation is actively taking place) on the surface and a gradual reduction in evaporation rate; the falling rate period, marked by a rapid decrease in evaporation rate due to reduced liquid content and increased air-filled porosity; and the final drying period, where only a small amount of liquid remains and drying primarily occurs through diffusion [82].

Similarly, the drying process of latex particles suspension can be divided into three distinct stages: initial drying, intermediate drying, and final drying. In the initial drying stage, the global drying rate remains constant and comparable to that of de-ionized water. In the intermediate drying stage, the global drying rate decreases as the particle packing density increases. In the final drying stage, the global drying rate increases again due to a decrease in particle mobility. [83].

The evaporation profile of liquid droplets from porous media such as buckypaper (a thin sheet or film composed of carbon nanotubes) can be used to develop a new type of sensor. The electrical resistance of the buckypaper changes during the evaporation process, and this change can be used to detect the presence of a liquid. This makes it possible to use buckypaper as a sensing material for various applications, such as environmental monitoring or medical diagnostics [84].

Heating is sometimes applied to study evaporation profile of liquid form porous media. In a study [84], heating by a Peltier element was applied to maintain a constant temperature throughout the experiment. This constant temperature ensured that the evaporation process occurred under controlled conditions, which is important for accurate measurements of electrical resistance and weight loss of the drying nanotube membrane. Additionally, heating can accelerate the evaporation process, which can be useful for

applications where rapid solvent removal is desired [84]. Another study [81], applied IR heating to mimic natural conditions at soil-air boundary (heating by sunlight).

1.5.2 The effect of heat on liquid flow in porous materials

An increase in temperature will affect the liquid flow in porous media such as reducing the viscosity of the liquid, induce phase change, enhance liquid diffusion, and may cause structure change in the porous media. Studying liquid flow at an elevated temperature by means of liquid flow visualization in porous media is therefore essential for understanding fluid behavior, heat and mass transfer prediction, performance optimization and for further development of advanced materials and technologies.

Some liquid transport in porous media occurred at an elevated temperature. For example, the transport of moisture in textile layers. Slight increase in the temperature of the porous media may occur during physical activities of the wearer. The transport of moisture in textile layers plays an important role in the conveyance of thermal energy through those layers. To maintain a constant core temperature during physical activity, the dissipation of thermal energy is crucial. The process of moisture transport in textile layers directly impacts the rate and effectiveness of heat transfer between the body and the surrounding environment. Therefore, understanding moisture transport behavior is important for optimizing thermal comfort and performance in clothing systems [16].

Liquid transport at high temperature environment is important for stope leaching study. Stope leaching is a mining technique used for extracting minerals from underground ore deposits. In stope leaching, a leaching solution is applied to the exposed ore surfaces within the stopes. The leaching solution typically contains a solvent or reagent that dissolves the desired mineral from the ore. High temperature is required to increase solubility of certain metals in the leaching solution, increase leaching reaction kinetics, and reduce viscosity of leaching solution. With an increase in temperature, the intra-particle liquid capillary rise increases slightly, whereas the liquid distribution profile remains unchanged [19].

Radiative heating influences heat and mass transfer in porous media such as soil and solar distillation membrane. In evaporation study of moisture from soil, IR heating is applied to simulate the heat fluxes that occur in real-world applications [86, 87].

1.5.3 Visualization of liquid flow in porous materials

Porous materials play a significant role in various natural and industrial processes involving fluid flow. Visualizing the interaction between liquid and porous materials helps in understanding the mechanisms and dynamics of fluid transport within the materials. This knowledge is crucial for optimizing processes such as filtration, groundwater flow, oil recovery, and chemical reactions occurring within porous structures. Some studies on liquid flow visualization methods are summarized in Table 1.4. The difference in spatial resolution and the penetration depth is summarized in Figure 1.5.

In the case of liquid flow monitoring in solar distillation membrane, a suitable visualization method allows for membrane's performance evaluation, membrane fouling detection, optimization of operating conditions, and system diagnosis and maintenance. By monitoring the interaction, one can assess the efficiency and effectiveness of the solar distillation process and make necessary adjustments to improve performance. Additionally, one can identify the conditions that maximize water production, energy efficiency, and overall system productivity.

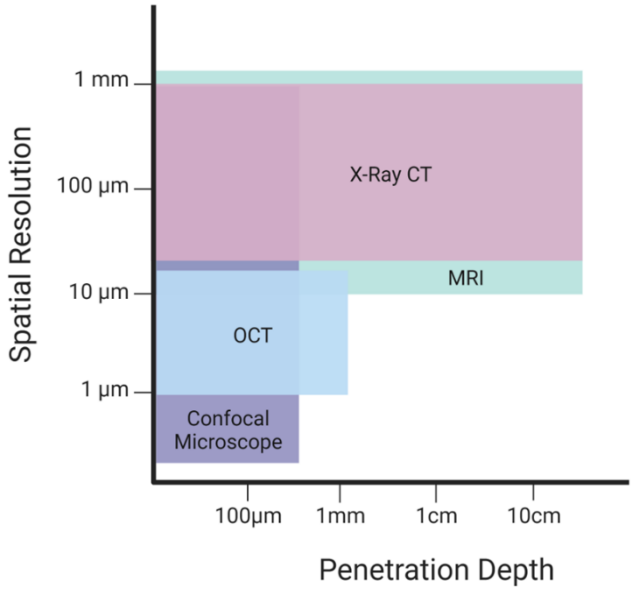

Figure 1. 5 Comparison of the spatial resolution and penetration depth of various liquid flow visualization method

Table 1.4. State of the art research on liquid flow monitoring in porous material

Type of porous media	Pore size	Thickness	Type of liquid	Phenomenon being investigated	Methods for monitoring	Reference
Multi-layered clothing system	-	~6.5 mm	Water	Penetration and evaporation	X-Ray Tomography	[15]
Metallic porous layers	25-400 μm	50-440 μm	Water, acetone, and glycerol-water mixture	Impaction	High-speed video camera	[71]
Micro- and nano-particles that are sintered together to form a porous structure	Few hundred nanometers	2 mm	Water	Impaction, spreading, and penetration	Video camera	[75]
Canopy fabric (polyamide grid silk)	-	80 μm	Deionized water	Impaction and spreading	High-speed camera	[72]
Buckypaper (mesoporous, self-supporting, electrically conducting mat of multiwall carbon nanotubes)	25-40 nm	140 μm	Acetone, 1-propanol, or N,N-dimethylformamide	Spreading, penetration, and evaporation	Simultaneous electrical resistivity measurement, weight measurement, and high-speed camera	[84]
Paper	-	~300 μm	Distilled water, silicon oil	Imbibition	Camera-assisted observation of liquid flow through horizontally placed paper strip	[78]

Table 1.4. State of the art research on liquid flow monitoring in porous material (cont.)

Paper	0.1 – 0.8 µm	-	Milli-Q water, aqueous glycerol, and hexelene glycol	Spreading and imbibition	Camera	[85]
Vertically aligned carbon nanotubes array	-	-	Ethanol and acetone	Spreading	High-speed camera	[86]
Single layer textiles	~ 3 µm (inter-fiber pore), ~150 µm (inter-yarn pore)	~ 300 µm	Silicone fluids	Penetration	X-ray computed tomography	[87]
Paper	-	~ 400 µm (non-pressed), ~275 µm (pressed)	Glycerol	Penetration	Optical coherence tomography (OCT)	[21]
Multi-layered liquid repellent fabrics	-	-	Oil	Penetration	Nuclear magnetic resonance (NMR)	[18]

Table 1.4. State of the art research on liquid flow monitoring in porous material (cont.)

Paper	Around 1.35 ~ 3.87 µm	Around 67 – 80 µm	Mineral oil, deionized water, and isopropanol	Penetration	Diffuse light reflection	[77]
Paper	Inter-fiber pores: 1-5 µm, intra-fiber pores: 10-100 nm	~ 200 µm	Water-based black ink	Penetration	Optical microscope, confocal laser scanning microscopy, trasnmission electron microscope (TEM)	[88]
Glass beads bed	-	-	Water mixed with fluorescent dye	Evaporation	Weighing balance, IR imaging, fluorescence dye mixed with water to visualize drying fronts and evaporation site	[82]
Cylindrical rock samples	-	100 mm	Distilled water	Capillary spread and rise	Magnetic Resonance Imaging (MRI)	[19]
Sintered copper materials	-	70 – 100 µm	Water	Liquid flow near nano- and micro-porous layer	Optical microscope	[89]
Glass beads bed	-	21.5 mm	Water	Evaporation	Fluorescence dye, IR camera, precision balance	[81]

Table 1.4. State of the art research on liquid flow monitoring in porous material (cont.)

Paper	-	-	Water	Imbibition	Mathematical modelling based on empirical data from other research	[90]
Porous stones	-	-	Water	Spreading, Imbibition	High-speed imaging and neutron radiography	[91]
Cellulosic micro-substrates	-	242 µm	Water	Imbibition	Optical and thermal imaging	[79]
Porous fabrics	-	4 mm	Deionized water	Spreading and imbibition	X-ray computed tomography	[92]
Commercial filter paper	-	~0.2 mm	Silicone oil	Imbibition	Camera-assisted observation of liquid flow through horizontally placed paper strip and theoretical modelling	[17]
Multi-layers washi paper and tobacco sheet	5-10 µm	218-221 µm	50% glycerol solution	Penetration	Fluorescent particles with fluorescence microscopy	[20]
Tobacco sheet	~5 µm	218-221 µm	Water	Evaporation (drying)	Spectral Domain – Optical Coherence Tomography (SD-OCT)	[93]
Paper and glass microfiber filter	-	104 – 260 µm	Aqueous co-solvent solutions	Spreading, penetration, and evaporation	Infrared thermography, capacitance measurement	[14]

1.6 Objective and significance of this dissertation

As mentioned in section 1.1, a fabrication method to enable robust design of functionalized thin porous materials is essential for many engineering applications. There is a growing body of knowledge aiming to develop low-cost and efficient fabrication methods to incorporate particles for enhanced functionalities of porous materials (Section 1.3). However, as discussed in section 1.3, the presently available fabrication methods still have some drawbacks which may hamper the development of materials for advanced applications. Additionally, as discussed in section 1.4, the development of a visualization technique to track liquid movement inside a thin porous materials under elevated temperature is important for performance optimization and further development of thin porous materials. The objective and significance of each chapter are described as follows.

Chapter 2: In this chapter, a tunable design of thin porous media is realized through a novel one-step membrane fabrication method by simultaneous electrospinning and carbon-based particles production through candle burning. The fabricated membrane holds potential applications as solar distillation membrane. A modification on the position of carbon-based photothermal particles relative to the membrane's fiber matrix was done by tuning photothermal particle introduction position along the electrospinning jet. Analysis on the water evaporation rate from the membrane and heat localization ability by the membrane was conducted to test the efficacy of the present membrane's design.

Chapter 3: In this chapter, a proof of concept on liquid flow visualization method on a fibrous porous media under the influence of heating was conducted by using optical coherence tomography (OCT). A porous tobacco layer is used as a model for this dissertation. Porous tobacco substrates has similar material properties as papers, filters, and membranes, such as similar thickness, with pores and fibrous structures. Additionally, these samples were cost-effective and readily available. Liquid movement inside thin porous media was monitored by observing the change in the attenuation coefficient from the OCT scan result of the sample. Dynamics of liquid flow at an elevated temperature can serve as an inspiration to many natural and engineering phenomena.

Chapter 4 (conclusion): in this chapter, the insights obtained in chapter 1, 2, and 3 are summarized. This dissertation reveals a facile fabrication method to incorporate particles in thin porous materials with tunable design and demonstrate a novel liquid flow visualization

system for sample under heating based on OCT. The structure of this dissertation is depicted in Figure 1.6.

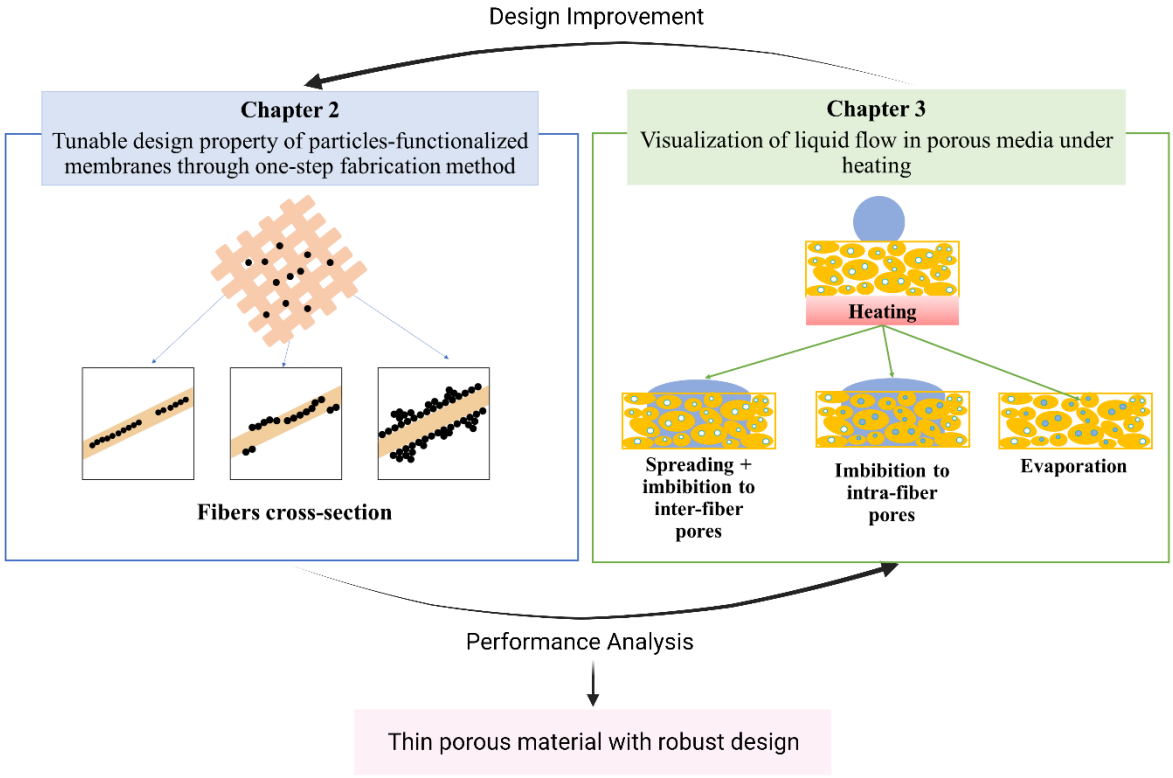

Figure 1. 6 The structure of this dissertation

1.7 References

[1] P. Trogadas, M.M. Nigra, M.O. Coppens, Nature-inspired optimization of hierarchical porous media for catalytic and separation processes, New J. Chem. 40 (2016) 4016–4026. https://doi.org/10.1039/c5nj03406j.

[2] X. Zhang, J. Ma, J. Zheng, R. Dai, X. Wang, Z. Wang, Recent advances in nature-inspired antifouling membranes for water purification, Chem. Eng. J. 432 (2022) 134425. https://doi.org/10.1016/j.cej.2021.134425.

[3] T. Chung, L. Ying, Y. Li, S. Kulprathipanja, Mixed matrix membranes (MMMs) comprising organic polymers with dispersed inorganic fillers for gas separation, Prog. Polym. Sci. 32 (2007) 483–507. https://doi.org/10.1016/j.progpolymsci.2007.01.008.

[4] T.C. Merkel, B.D. Freeman, R.J. Spontak, Z. He, I. Pinnau, P. Meakin, A.J. Hill, Ultrapermeable, Reverse-Selective Nanocomposite Membranes, Science. 296 (2002) 519–522. https://doi.org/10.1126/science.1069580.

[5] A. Razmjou, E. Arifin, G. Dong, J. Mansouri, V. Chen, Superhydrophobic modification of TiO_2 nanocomposite PVDF membranes for applications in membrane distillation, J. Memb. Sci. 415–416 (2012) 850–863. https://doi.org/10.1016/j.memsci.2012.06.004.

[6] L. Yan, Y. Shui, C. Bao, S. Xianda, Effect of nano-sized Al2O3 -particle addition on PVDF ultrafiltration membrane performance, J. Memb. Sci. 276 (2006) 162–167. https://doi.org/10.1016/j.memsci.2005.09.044.

[7] D.M. Warsinger, S. Chakraborty, E.W. Tow, M.H. Plumlee, C. Bellona, S. Loutatidou, L. Karimi, A.M. Mikelonis, A. Achilli, A. Ghassemi, L.P. Padhye, S.A. Snyder, S. Curcio, C.D. Vecitis, H.A. Arafat, J.H.L. V, Progress in Polymer Science A review of polymeric membranes and processes for potable water reuse, Prog. Polym. Sci. 81 (2018) 209–237. https://doi.org/10.1016/j.progpolymsci.2018.01.004.

[8] S.J. Oh, N. Kim, Y.T. Lee, Preparation and characterization of PVDF / TiO 2 organic – inorganic composite membranes for fouling resistance improvement, J. Memb. Sci. 345 (2009) 13–20. https://doi.org/10.1016/j.memsci.2009.08.003.

[9] M. Padaki, R.S. Murali, M.S. Abdullah, N. Misdan, A. Moslehyani, M.A. Kassim, N. Hilal, A.F. Ismail, Membrane technology enhancement in oil – water separation . A review, Desalination. 357 (2015) 197–207. https://doi.org/10.1016/j.desal.2014.11.023.

[10] E. Bet-moushoul, Y. Mansourpanah, K. Farhadi, M. Tabatabaei, TiO_2 nanocomposite based polymeric membranes : A review on performance improvement for various applications in chemical engineering processes, Chem. Eng. J. 283 (2016) 29–46. https://doi.org/10.1016/j.cej.2015.06.124.

[11] J.E. Otterstedt, D.A. Brandreth, Small Particles in Paper, in: Small Part. Technol., Springer, Boston, 1998: pp. 407–429. https://doi.org/10.1007/978-1-4757-6523-6_4.

[12] E. Verleysen, M. Ledecq, L. Siciliani, K. Cheyns, C. Vleminckx, M.N. Blaude, S. De Vos, F. Brassinne, F. Van Steen, R. Nkenda, R. Machiels, N. Waegeneers, J. Van Loco, J. Mast, Titanium dioxide particles frequently present in face masks intended for general use require regulatory control, Sci. Rep. 12 (2022) 1–9. https://doi.org/10.1038/s41598-022-06605-w.

[13] N.S. Fuzil, N.H. Othman, N.H. Alias, F. Marpani, M.H.D. Othman, A.F. Ismail, W.J.

Lau, K. Li, T.D. Kusworo, I. Ichinose, M.M.A. Shirazi, A review on photothermal material and its usage in the development of photothermal membrane for sustainable clean water production, Desalination. 517 (2021) 115259. https://doi.org/10.1016/j.desal.2021.115259.

[14] M.G. Wijburg, S. Wang, A.A. Darhuber, Transport and evaporation of aqueous co-solvent solutions in thin porous media, Colloids Surfaces A Physicochem. Eng. Asp. 656 (2023) 130268. https://doi.org/10.1016/j.colsurfa.2022.130268.

[15] M. Weder, P.A. Brühwiler, A. Laib, X-Ray Tomography Measurements of the Moisture Distribution in Multilayered Clothing Systems, Text. Res. J. 76 (2006) 18–26. https://doi.org/10.1177/0040517506053910.

[16] A.W. Martinez, S.T. Phillips, G.M. Whitesides, E. Carrilho, Diagnostics for the developing world: Microfluidic paper-based analytical devices, Anal. Chem. 82 (2010) 3–10. https://doi.org/10.1021/ac9013989.

[17] S. Chang, J. Seo, S. Hong, D.G. Lee, W. Kim, Dynamics of liquid imbibition through paper with intra-fiber pores, J. Fluid Mech. 845 (2018) 36–50. https://doi.org/10.1017/jfm.2018.235.

[18] M. Bencsik, H. Adriaensen, S.A. Brewer, G. McHale, Quantitative NMR monitoring of liquid ingress into repellent heterogeneous layered fabrics, J. Magn. Reson. 193 (2008) 32–36. https://doi.org/10.1016/j.jmr.2008.04.003.

[19] Z. Xue, D. Gan, Y. Zhang, Z. Liu, Analysis of intra - particle liquid capillary spread mechanisms in high - temperature stope leaching using MRI, Sci. Rep. (2022) 1–11. https://doi.org/10.1038/s41598-022-09154-4.

[20] Y. Asanuma, T.N. Pratiwi, M. Wada, T. Iwai, I.W. Lenggoro, Liquid Transport of Heated Glycerol-Water Mixtures with Colloidal Fluorescent Particles through Multiple Biomass Layers, E-Journal Surf. Sci. Nanotechnol. 20 (2022) 13–19. https://doi.org/10.1380/ejssnt.2022-008.

[21] T. Fabritius, R. Myllylä, Liquid sorption investigation of porous media by optical coherence tomography, J. Phys. D. Appl. Phys. 39 (2006) 4668–4672. https://doi.org/10.1088/0022-3727/39/21/025.

[22] B.B. Buchanan, W. Gruissem, R.L. Jones, eds., Biochemistry and Molecular Biology

of Plants, 2nd Edition, John Wiley & Sons, Chichester, 2015.

[23] S. Olivera, H.B. Muralidhara, K. Venkatesh, V.K. Guna, K. Gopalakrishna, Y. Kumar K., Potential applications of cellulose and chitosan nanoparticles/composites in wastewater treatment: A review, Carbohydr. Polym. 153 (2016) 600–618. https://doi.org/10.1016/j.carbpol.2016.08.017.

[24] S. Homaeigohar, A.R. Boccaccini, Antibacterial biohybrid nanofibers for wound dressings, Acta Biomater. 107 (2020) 25–49. https://doi.org/10.1016/j.actbio.2020.02.022.

[25] A. Moeini, P. Pedram, P. Makvandi, M. Malinconico, G. Gomez d'Ayala, Wound healing and antimicrobial effect of active secondary metabolites in chitosan-based wound dressings: A review, Carbohydr. Polym. 233 (2020) 115839. https://doi.org/10.1016/j.carbpol.2020.115839.

[26] R.A. Ilyas, H.A. Aisyah, A.H. Nordin, N. Ngadi, M. Yusoff, M. Zuhri, M. Rizal, M. Asyraf, S.M. Sapuan, E.S. Zainudin, S. Sharma, H. Abral, M. Asrofi, E. Syafri, Nanocomposites for Various Advanced Applications, Polymers (Basel). 14 (2022) 1–36. https://doi.org/ 10.3390/polym14050874.

[27] V. Vatanpour, M.E. Pasaoglu, H. Barzegar, O.O. Teber, R. Kaya, M. Bastug, A. Khataee, I. Koyuncu, Cellulose acetate in fabrication of polymeric membranes: A review, Chemosphere. 295 (2022). https://doi.org/10.1016/j.chemosphere.2022.133914.

[28] P.R. Yaashikaa, P. Senthil Kumar, S. Karishma, Review on biopolymers and composites – Evolving material as adsorbents in removal of environmental pollutants, Environ. Res. 212 (2022) 113114. https://doi.org/10.1016/j.envres.2022.113114.

[29] H.M.C. Azeredo, M.F. Rosa, L.H.C. Mattoso, Nanocellulose in bio-based food packaging applications, Ind. Crops Prod. 97 (2017) 664–671. https://doi.org/10.1016/j.indcrop.2016.03.013.

[30] E. Diaz-Montes, R. Castro-Munoz, Edible films and coatings s food-quality preservers: an overview, Foods. 10 (2021) 249. https://doi.org/ 10.3390/foods10020249.

[31] P. Rai, S. Mehrotra, S. Priya, E. Gnansounou, S.K. Sharma, Recent advances in the sustainable design and applications of biodegradable polymers, Bioresour. Technol. 325 (2021) 124739. https://doi.org/10.1016/j.biortech.2021.124739.

[32] R. Zhang, W. Lan, T. Ji, D.E. Sameen, S. Ahmed, W. Qin, Y. Liu, Development of polylactic acid/ZnO composite membranes prepared by ultrasonication and electrospinning for food packaging, Lwt. 135 (2021) 110072. https://doi.org/10.1016/j.lwt.2020.110072.

[33] S. Tanpichai, A. Boonmahitthisud, N. Soykeabkaew, L. Ongthip, Review of the recent developments in all-cellulose nanocomposites: Properties and applications, Carbohydr. Polym. 286 (2022) 119192. https://doi.org/10.1016/j.carbpol.2022.119192.

[34] Y. Luo, Q. Wang, Recent development of chitosan-based polyelectrolyte complexes with natural polysaccharides for drug delivery, Int. J. Biol. Macromol. 64 (2014) 353–367. https://doi.org/10.1016/j.ijbiomac.2013.12.017.

[35] A. Anitha, S. Sowmya, P.T.S. Kumar, S. Deepthi, K.P. Chennazhi, H. Ehrlich, M. Tsurkan, R. Jayakumar, Chitin and chitosan in selected biomedical applications, Prog. Polym. Sci. 39 (2014) 1644–1667. https://doi.org/10.1016/j.progpolymsci.2014.02.008.

[36] P. Saxena, P. Shukla, A comprehensive review on fundamental properties and applications of poly(vinylidene fluoride) (PVDF), Adv. Compos. Hybrid Mater. 4 (2021) 8–26. https://doi.org/10.1007/s42114-021-00217-0.

[37] N.A. Alenazi, M.A. Hussein, K.A. Alamry, A.M. Asiri, Modified polyether-sulfone membrane: A mini review, Des. Monomers Polym. 20 (2017) 532–546. https://doi.org/10.1080/15685551.2017.1398208.

[38] K.S.Y. Lau, 10 - High-Performance Polyimides and High Temperature Resistant Polymers, in: H. Dodiuk, S. H. Goodman (Eds.) Handbook of Thermoset Plastics (Third Edition), William Andrew Publishing, 2014, pp. 297-424. https://doi.org/10.1016/B978-1-4557-3107-7.00010-5.

[39] S. Iijima, Helical microtubules of graphitic carbon, Nature. 354 (1991) 56–58. Third Edit, Elsevier Inc., 2014. https://doi.org/10.1016/B978 1 4557 3107 7.00010 5.

[40] S. Homaeigohar, T. Strunskus, J. Strobel, L. Kienle, M. Elbahri, A Flexible Oxygenated Carbographite Nanofilamentous Buckypaper as an Amphiphilic Membrane, Adv. Mater. Interfaces. 5 (2018) 1–10. https://doi.org/10.1002/admi.201800001.

[41] M. Asaeda, L.D. Du, Separation of Alcohol/ Water Gaseous Mixtures by Thin

Ceramic Membrane, J. Chem. Eng. Japan. 19 (1986) 72–77. https://doi.org/10.1252/jcej.19.72.

[42] F. Lin, S. Zhang, G. Ma, L. Qiu, H. Sun, Application of Ceramic Membrane in Water and Wastewater Treatment, E3S Web Conf. 53 (2018) 4–7. https://doi.org/10.1051/e3sconf/20185304032.

[43] C. Yacou, D. Wang, J. Motuzas, X. Zhang, S. Smart, J.C. Diniz da Costa, Thin-Film Ceramic Membranes, in: E. M. V. Hoek, V. V. Tarabara (Eds.) Encyclopedia of Membrane Science and Technology, 2013, pp. 1-36. https://doi.org/10.1002/9781118522318.emst042.

[44] T.Y. Liu, H.G. Yuan, Y.Y. Liu, D. Ren, Y.C. Su, X. Wang, Metal-Organic Framework Nanocomposite Thin Films with Interfacial Bindings and Self-Standing Robustness for High Water Flux and Enhanced Ion Selectivity, ACS Nano. 12 (2018) 9253–9265. https://doi.org/10.1021/acsnano.8b03994.

[45] V.F. Yusuf, N.I. Malek, S.K. Kailasa, Review on Metal-Organic Framework Classification, Synthetic Approaches, and Influencing Factors: Applications in Energy, Drug Delivery, and Wastewater Treatment, ACS Omega. 7 (2022) 44507–44531. https://doi.org/10.1021/acsomega.2c05310.

[46] L. Figueroa-Quintero, D. Villalgordo-Hernandez, J.J. Delgado-Marin, J. Narciso, V.K. Velisoju, P. Castano, J. Gascon, E. V. Ramoz-Fernandez, Post-Synthetic Surface Modification of Metal-Organic Frameworks and Their Potential Applications, Small Methods. (2022). https://doi.org/10.1002/smtd.202201413.

[47] O.M. Yaghi, H. Li, Hydrothermal Synthesis of a Metal-Organic Framework Containing Large Rectangular Channels, J. Am. Chem. Soc. 117 (1995) 10401–10402. https://doi.org/10.1021/ja00146a033.

[48] S.B. Aboeleneen, M.A. Scully, J.C. Harris, E.H. Sterin, E.S. Day, Membrane-wrapped nanoparticles for photothermal cancer therapy, Nano Converg. 9 (2022). https://doi.org/10.1186/s40580-022-00328-4.

[49] H.M. Wilson, S. Rahman A.R., A.E. Parab, N. Jha, Ultra-low cost cotton based solar evaporation device for seawater desalination and waste water purification to produce drinkable water, Desalination. 456 (2019) 85–96.

https://doi.org/10.1016/j.desal.2019.01.017.

[50] H.M. Wilson, S. Rahman AR, T. Garg, N. Jha, Recycling of hazardous diesel soot particles into a high performance solar evaporation device, Appl. Surf. Sci. 487 (2019) 951–961. https://doi.org/10.1016/j.apsusc.2019.05.080.

[51] H.M. Wilson, Tushar, S. Raheman Ar, N. Jha, Plant-derived carbon nanospheres for high efficiency solar-driven steam generation and seawater desalination at low solar intensities, Sol. Energy Mater. Sol. Cells. 210 (2020) 110489. https://doi.org/10.1016/j.solmat.2020.110489.

[52] H.M. Wilson, S. Raheman A. R, H.W. Lim, S.J. Lee, Conversion of Hazardous Diesel Soot Particles into a Novel Highly Efficient 3D Hydrogel for Solar Desalination and Wastewater Purification, ACS Omega. 8 (2022) 2740-2751. https://doi.org/10.1021/acsomega.2c07430.

[53] L. Zhang, B. Bai, N. Hu, H. Wang, Low-cost and facile fabrication of a candle soot/adsorbent cotton 3D-interfacial solar steam generation for effective water evaporation, Sol. Energy Mater. Sol. Cells. 221 (2021) 1–9. https://doi.org/10.1016/j.solmat.2020.110876.

[54] M.U. Rashid, Z. Tahir, S. Kim, J.I. Jang, Y.S. Kim, Selective Deposition of Candle Soot on a Cellulose Membrane for Efficient Solar Evaporation, ACS Omega. 6 (2021) 31366–31374. https://doi.org/10.1021/acsomega.1c05348.

[55] A.M. Saleque, S. Ma, S. Ahmed, M.I. Hossain, W. Qarony, Y.H. Tsang, Solar Driven Interfacial Steam Generation Derived from Biodegradable Luffa Sponge, Adv. Sustain. Syst. 5 (2021) 1–12. https://doi.org/10.1002/adsu.202000291.

[56] C. Xiao, W. Liang, L. Chen, J. He, F. Liu, H. Sun, Z. Zhu, A. Li, Janus Poly(ionic liquid) Monolithic Photothermal Materials with Superior Salt-Rejection for Efficient Solar Steam Generation, ACS Appl. Energy Mater. 2 (2019) 8862–8870. https://doi.org/10.1021/acsaem.9b01856.

[57] H. Sun, Y. Li, J. Li, Z. Zhu, W. Zhang, W. Liang, C. Ma, A. Li, Facile Preparation of a Carbon-Based Hybrid Film for Efficient Solar-Driven Interfacial Water Evaporation, ACS Appl. Mater. Interfaces. 13 (2021) 33427–33436. https://doi.org/10.1021/acsami.1c06226.

[58] S. Wu, Y. Du, Y. Alsaid, D. Wu, M. Hua, Y. Yan, B. Yao, Y. Ma, X. Zhu, X. He, Superhydrophobic photothermal icephobic surfaces based on candle soot, Proc. Natl. Acad. Sci. 117 (2020) 11240–11246. https://doi.org/10.1073/pnas.2001972117.

[59] P. Pallavicini, G. Chirico, A. Taglietti, Harvesting Light To Produce Heat: Photothermal Nanoparticles for Technological Applications and Biomedical Devices, Chem. - A Eur. J. 27 (2021) 15361–15374. https://doi.org/10.1002/chem.202102123.

[60] X. Yang, L. Chen, Y. Li, J.C. Rooke, C. Sanchez, B. Su, Hierarchically porous materials : synthesis strategies and structure design, Chem. Soc. Rev. 46 (2017) 481–558. https://doi.org/10.1039/C6CS00829A.

[61] X. Jiang, Y. Shao, J. Li, M. Wu, Y. Niu, X. Ruan, X. Yan, X. Li, G. He, Bioinspired Hybrid Micro / Nanostructure Composited Membrane with Intensi fi ed Mass Transfer and Antifouling for High Saline Water Membrane Distillation, ACS Nano. 14 (2020) 17376–17386. https://doi.org/10.1021/acsnano.0c07543.

[62] C. Wei, F. Dai, L. Lin, Z. An, Y. He, X. Chen, L. Chen, Simplified and robust adhesive-free superhydrophobic SiO_2 -decorated PVDF membranes for efficient oil/ water separation, 555 (2018) 220–228. https://doi.org/10.1016/j.memsci.2018.03.058.

[63] A. Khlyustova, Y. Cheng, R. Yang, Vapor-deposited functional polymer thin films in biological applications, J. Mater. Chem. B. 8 (2020) 6588–6609. https://doi.org/10.1039/D0TB00681E.

[64] L. Zhao, R. Chen, L. Lou, X. Jing, Q. Liu, J. Liu, J. Yu, P. Liu, J. Wang, Layer-by-Layer-Assembled antifouling films with surface microtopography inspired by Laminaria japonica, Appl. Surf. Sci. 511 (2020) 145564. https://doi.org/https://doi.org/10.1016/j.apsusc.2020.145564.

[65] J. Wu, Y. Ding, J. Wang, T. Li, H. Lin, J. Wang, F. Liu, Facle fabrication of nanofiber- and micro/nanosphere-coordinated PVDF membrane with ultrahigh permeability of viscous water-in-oil emulsion, J. Mater. Chem. A. 6 (2018) 7014–7020. https://doi.org/10.1039/c8ta01539b.

[66] S. Yuan, J. Zhu, Y. Li, Y. Zhao, J. Li, P. Van Puyvelde, B. Van der Bruggen, Structure architecture of micro/nanoscale ZIF-L on 3D printed membrane for superhydrophobic and underwater superoleophobic surface, J. Mater. Chem. A. 2 (2019) 2723–2729.

https://doi.org/10.1039/C8TA10249J.

[67] L.M. Robeson, Correlation of separation factor versus permeability for polymeric membranes, J. Memb. Sci. 62 (1991) 165–185.

[68] W. Chou, D.-G. Yu, M.-C. Yang, The preparation and characterization of silver-loading cellulose acetate hollow fiber membrane for water treatment, Polym. Adv. Technol. 16 (2005) 600–607. https://doi.org/10.1002/pat.630.

[69] W. Li, L. Deng, H. Huang, J. Zhou, Y. Liao, L. Qiu, H. Yang, L. Yao, Janus Photothermal Membrane as an Energy Generator and a Mass-Transfer Accelerator for High-Efficiency Solar-Driven Membrane Distillation, ACS Appl. Mater. Interfaces. 13 (2021) 26861–26869. https://doi.org/10.1021/acsami.1c01072.

[70] T. Lei, J. Xiong, J. Huang, T. Zheng, X. Cai, Facile transformation of soot nanoparticles into nanoporous fibers via single-step electrospinning, AIP Adv. 7 (2017) 085212. https://doi.org/10.1063/1.4996397.

[71] C. Boscariol, S. Chandra, D. Sarker, C. Crua, M. Marengo, Drop impact onto attached metallic meshes: liquid penetration and spreading, Exp. Fluids. 59 (2018) 1–13. https://doi.org/10.1007/s00348-018-2640-y.

[72] H. Cheng, C. Qiu, C. Zhou, X. Sun, R. Yang, Experimental study of spreading characteristics of droplet impacting on canopy fabric surface, Mod. Phys. Lett. B. 31 (2017) 1–11. https://doi.org/10.1142/S0217984917503250.

[73] S. Moghtadernejad, C. Lee, M. Jadidi, An introduction of droplet impact dynamics to engineering students, Fluids. 5 (2020) 1–18. https://doi.org/10.3390/fluids5030107.

[74] X. Liu, K. Wang, Y. Fang, R.J. Goldstein, S. Shen, Study of the effect of surface wettability on droplet impact on spherical surfaces, Int. J. Low-Carbon Technol. 15 (2021) 414–420. https://doi.org/10.1093/IJLCT/CTZ077.

[75] W. Yang, J. Xu, Drop spreading and penetrating on micro/nano particle sintering porous with multiscale structure, Colloids Surfaces A Physicochem. Eng. Asp. 516 (2017) 9–22. https://doi.org/10.1016/j.colsurfa.2016.12.005.

[76] A.W. Adamson, Potential Distortion Model for Contact Angle and Spreading, J. Colloid Interface Sci. 44 (1972) 273–281.

[77] T. Karppinen, I. Kassamakov, J. Aaltonen, H. Pajari, E. Hæggstrom, Measuring liquid penetration in the thickness direction of paper, Eur. Phys. J. Appl. Phys. 32 (2005) 65–71. https://doi.org/10.1051/epjap.

[78] S. Chang, W. Kim, Dynamics of water imbibition through paper with swelling, J. Fluid Mech. 892 (2020). https://doi.org/10.1017/jfm.2020.219.

[79] A. Terzis, E. Roumeli, K. Weishaupt, S. Brack, H. Aslannejad, J. Groß, S.M. Hassanizadeh, R. Helmig, B. Weigand, Heat release at the wetting front during capillary filling of cellulosic micro-substrates, J. Colloid Interface Sci. 504 (2017) 751-757. https://doi.org/10.1016/j.jcis.2017.06.027.

[80] S. Hasan, K. Sobolev, M. Nosonovsky, Evaporation of droplets capable of bearing viruses airborne and on hydrophobic surfaces, J. Appl. Phys. 129 (2021) 024703. https://doi.org/10.1063/5.0023501.

[81] N. Kumar, J.H. Arakeri, Evaporation From Layered Porous Medium in the Presence of Infrared Heating, Water Resour. Res. 54 (2018) 7670–7687. https://doi.org/10.1029/2017WR021954.

[82] N. Kumar, J.H. Arakeri, Evaporation From Confined Porous Media Due to Controlled IR Heating From Above, Transp. Porous Media. 125 (2018) 311–340. https://doi.org/10.1007/s11242-018-1120-4.

[83] H. Huang, Y. Huang, W. Lau, H.D. Ou-Yang, C. Zhou, M.S. El-Aasser, Integrating optical coherence tomography with gravimetric and video analysis (OCT-Gravimetry-Video method) for studying the drying process of polystyrene latex system, Sci. Rep. 8 (2018) 1–13. https://doi.org/10.1038/s41598-018-30914-8.

[84] G. Schuszter, E.S. Bogya, D. Horváth, Á. Tóth, H. Haspel, Á. Kukovecz, Liquid droplet evaporation from buckypaper: On the fundamental properties of the evaporation profile, Microporous Mesoporous Mater. 209 (2015) 105–112. https://doi.org/10.1016/j.micromeso.2015.02.025.

[85] A. Clarke, T.D. Blake, K. Carruthers, A. Woodward, Spreading and Imbibition of Liquid Droplets on Porous Surfaces, Langmuir. 18 (2002) 2980–2984. https://doi.org/10.1021/la0117810.

[86] Y. Huang, Q. Chen, R. Wang, Visualization study on capillary-spreading behavior of

liquid droplet in vertically aligned carbon nanotube array, Int. J. Heat Mass Transf. 120 (2018) 1055–1064. https://doi.org/10.1016/j.ijheatmasstransfer.2017.12.122.

[87] G. Zhang, R. Parwani, C.A. Stone, A.H. Barber, L. Botto, X-ray Imaging of Transplanar Liquid Transport Mechanisms in Single Layer Textiles, Langmuir. 33 (2017) 12072–12079. https://doi.org/10.1021/acs.langmuir.7b02982.

[88] B.A. Arthur, R.P. Smith, S. Lavrykov, B. V. Ramarao, Imaging of ink jet penetration in uncoated paper using microscopic techniques, Tappi J. 10 (2011) 35–40. https://doi.org/10.1016/B978-0-12-394626-3.00009-0.

[89] H. Sun, Z. Kawara, Y. Ueki, T. Naritomi, T. Kunugi, Consideration of heat transfer enhancement mechanism of nano- and micro-scale porous layer via flow visualization, Heat Transf. Eng. 32 (2011) 968–973. https://doi.org/10.1080/01457632.2011.556382.

[90] J. Songok, P. Salminen, M. Toivakka, Journal of Colloid and Interface Science Temperature effects on dynamic water absorption into paper, J. Colloid Interface Sci. 418 (2014) 373–377. https://doi.org/10.1016/j.jcis.2013.12.017.

[91] J.B. Lee, A.I. Radu, P. Vontobel, D. Derome, J. Carmeliet, Absorption of impinging water droplet in porous stones, J. Colloid Interface Sci. 471 (2016) 59–70. https://doi.org/10.1016/j.jcis.2016.03.002.

[92] M. Gonçalves, J.Y. Kim, Y. Kim, N. Rubab, N. Jung, T. Asai, Droplet evaporation on porous fabric materials, Sci. Rep. 12 (2022) 1–11. https://doi.org/10.1038/s41598-022-04877-w.

[93] T. Makino, H. Ujino, I.W. Lenggoro, T. Iwai, Imaging and quantitative analysis of water evaporation process using spectral-domain optical coherence tomography under illumination with two near-infrared wavelengths, Opt. Rev. 30 (2023) 158–165. https://doi.org/10.1007/s10043-023-00792-1.

Chapter 2: Heat and Flow Phenomena in Liquid-Filled Soot Particle–Embedded Porous Membranes: Fabrication by Candle Burning–Assisted Electrospinning

Abbreviation

DMF	Dimethylformamide
FE-SEM	Field emission-scanning electron microscopy
M	Middle
NC	Near collector
NIR	Near Infrared
NM	No membrane
NS	Near syringe
PVDF	Polyvinylidene fluoride
RH	Relative humidity
TEM	Transmission electron microscopy
WHO	World Health Organization

2.1 Introduction

Freshwater scarcity is a significant global challenge that affects millions of people [1]. Although water bodies cover two-thirds of the earth's surface, only 2.53% of them contain freshwater [2]. The imbalance between freshwater withdrawal and natural renewal rates has been caused by climate change, as well as the exploitation of freshwater due to population growth and economic activities [3, 4]. Projections indicate that by 2050, approximately 57% of the world's population will reside in areas where water scarcity will be experienced for at least one month annually [5]. In order to ensure a sustainable water supply, it is crucial to develop a cost-effective and efficient method for producing freshwater from seawater and contaminated water sources.

The desalination of brackish and seawater holds promise as a potential solution to address the growing global water demand [6, 7]. As of 2019, there were 15,906 active desalination plants in operation across 177 countries [6]. Desalination methods such as reverse osmosis, multistage flash distillation, and multi-effect distillation show potential. However, their suitability for implementation in developing nations remains a subject of debate due to concerns regarding their high operational costs, significant greenhouse gas emissions, and the generation of toxic waste, which can have adverse effects on marine ecosystems [7].

Solar distillation, a promising technique for water purification and desalination, utilizes solar energy as the sole driving force to separate water from contaminated sources [8]. The absorption of water primarily occurs in the infrared (IR) light range with wavelengths longer than 1200 nm, while the solar spectrum exhibits high intensity in the visible region (400-700 nm) [9]. These disparities across different wavelength regions hinder the natural process of solar distillation. To address this, photothermal materials have emerged as light-absorbing substances capable of converting visible solar light into heat [10]. By employing these materials at the interface between air and water, heat localization can be achieved, leading to efficient solar distillation [10]. Examples of such materials include metallic nanostructures [11], carbon-based materials [12], inorganic semiconductors [13], and polymer materials [14]. Carbon-based photothermal materials, in particular, have gained significant attention due to their black body-like characteristics, including high light absorption efficiency, chemical stability, abundance in sources, and easy fabrication methods [10, 15].

Carbon-based photothermal materials can be derived from the soot particles generated during the incomplete combustion of a candle flame. These particles demonstrate excellent

efficiency in converting light into heat [16–18]. The process of obtaining candle soot is straightforward, cost-effective, and easily scalable, unlike the fabrication processes involved in producing graphene or carbon nanotubes [16].

Previous research has primarily utilized two methods to incorporate soot particles into a matrix. The first method involves direct deposition, where the particles are deposited from the flame onto a matrix surface coated with a polymeric adhesive [18, 19]. The second method is a two-step process, where the soot particles are initially dispersed in a solvent, and then the polymer is dip-coated into the soot particle suspension [9], [15–17], [20–22]. However, both methods require a preexisting matrix. The direct deposition approach [18] does not account for the potential impact of polymer coating on the photothermal conversion efficiency of the soot particles. On the other hand, the two-step method [19] has not adequately addressed the stability of the soot particle suspension. To ensure the prevention of morphological defects and uneven particle distribution in polymer fibers and membranes, it is crucial to maintain particle stability within the precursor polymer solution (suspension) by preventing particle aggregation and settling [23]. It is believed that achieving an even distribution of photothermal particles within the polymer matrix and fibers is vital for efficient solar distillation utilizing a photothermal membrane.

Electrospinning is a versatile technique widely employed for the production of polymer fibrous membranes, offering a large surface area and customizable morphology [24]. This method can also be utilized to create a polymer matrix embedded with photothermal materials. Specifically, carbon-based nanomaterials can be integrated into fibers through the electrospinning process using a mixed solution of polyvinylidene fluoride (PVDF) and candle soot particles [24]. To ensure the stability of the soot particles within the initial liquid, it is crucial to determine an appropriate polymer concentration and maintain continuous mixing of the solution [24]. The properties of the electrospun fiber are influenced by significant parameters such as size distribution, surface wettability, concentration, and stability of the dispersed particles in the mixed solution [25]. Given the complexity of simultaneously controlling all these parameters when fabricating various particle and polymer combinations, Li et al. [25] proposed a method involving simultaneous electrospinning (for polymer fibers) and electrospraying (for aerosol particles). This approach allows for the incorporation of particles into polymer fibers without modifying their surface properties by separating the polymer and particle sources [25].

In this chapter, a novel approach called candle burning–assisted electrospinning is presented, which enables the production of "fresh" carbon-based aerosols. These aerosols are

subsequently incorporated into polymer fibers to fabricate membranes suitable for solar distillation. This method eliminates the necessity of employing extra chemicals or procedures to achieve particle dispersion in the solution. The resulting membranes have the capability to produce desalinated potable water [26] from brackish water sources.

2.2 Materials and methods

2.2.1 Preparation of polymer solution

Polyvinylidene fluoride (PVDF) (Polysciences, Inc., USA) was dissolved in an N, N-dimethylformamide (DMF) (Wako Pure Chemical Industries, Ltd., Japan)/acetone (Wako Pure Chemical Industries, Ltd., Japan) mixture to obtain 20 wt.% of PVDF solution. The DMF to acetone volume ratio was 7:3. The mixture was stirred (150 rpm) at 70℃ for 2 h before use. PVDF was chosen due to its good thermal stability, UV resistance, and mechanical strength {Formatting Citation}.

2.2.2 Candle burning-assisted electrospinning

Membranes were fabricated by introducing soot particles into a polymer jet during electrospinning. Various concentrations of soot particles were obtained by burning candles inside and outside the electrospinning chamber. Commercial paraffin wax candles (Daiko Co. Ltd., Japan) with 175 mm height, 15 mm diameter, and 100 g weight were used to produce soot particles in this study. Soot particles were introduced at three introduction points for electrospinning: near the syringe (NS), in the middle of the needle tip and collector (M), and near the collector (NC). The variations of the introduction point of the aerosols allowed different positionings of the photothermal materials relative to the polymer fiber. The membranes produced using the soot particles obtained from the candles burning inside and outside the chamber are termed “in-membranes” and “out-membranes,” respectively. For in-membranes (Figure 2.1), candle was burned inside the electrospinning chamber, whereas for out-membranes, a conductive silicone tube was used to transport soot particles from outside the chamber where the candle was burned, to the desired position in the electrospinning chamber.

Soot particles are transported to the electrospinning jet by means of convective flow. Candle burning is an exothermic process (releasing heat). The heat released by this process increases the air temperature in the surrounding. The rise in air temperature increases its kinetic energy, which leads to an increase in the frequency of the gas molecular collision.

High energy collisions between gas molecules and soot particles (primary particle size around 25-30 nm) can propel soot particles to move in the direction of temperature gradient (towards areas with lower temperatures where gas kinetic energy is lower) [26].

Electrospinning was performed by applying a voltage of +15.38 kV to a stainless-steel needle (inside diameter: 0.603 mm, outside diameter: 0.9081 mm) attached to a syringe filled with polymer solution using a high-voltage power supply (HAR-20R1.5, Matsusada Precision, Inc., Japan). The polymer solution was supplied at a flow rate of 0.5 mL/h using a syringe pump (KDS100, KD Scientific Inc., USA). An electrically grounded, 100 × 100 mm^2 aluminum foil fixed on a wooden stand was used as the collector for the fiber. The tip-to-collector distance was maintained at 200 mm. The relative humidity (RH) inside the chamber was controlled at 30% using a humidity control unit (PAU-300S, Apiste Corp., Japan). The temperature was maintained at approximately 22℃.

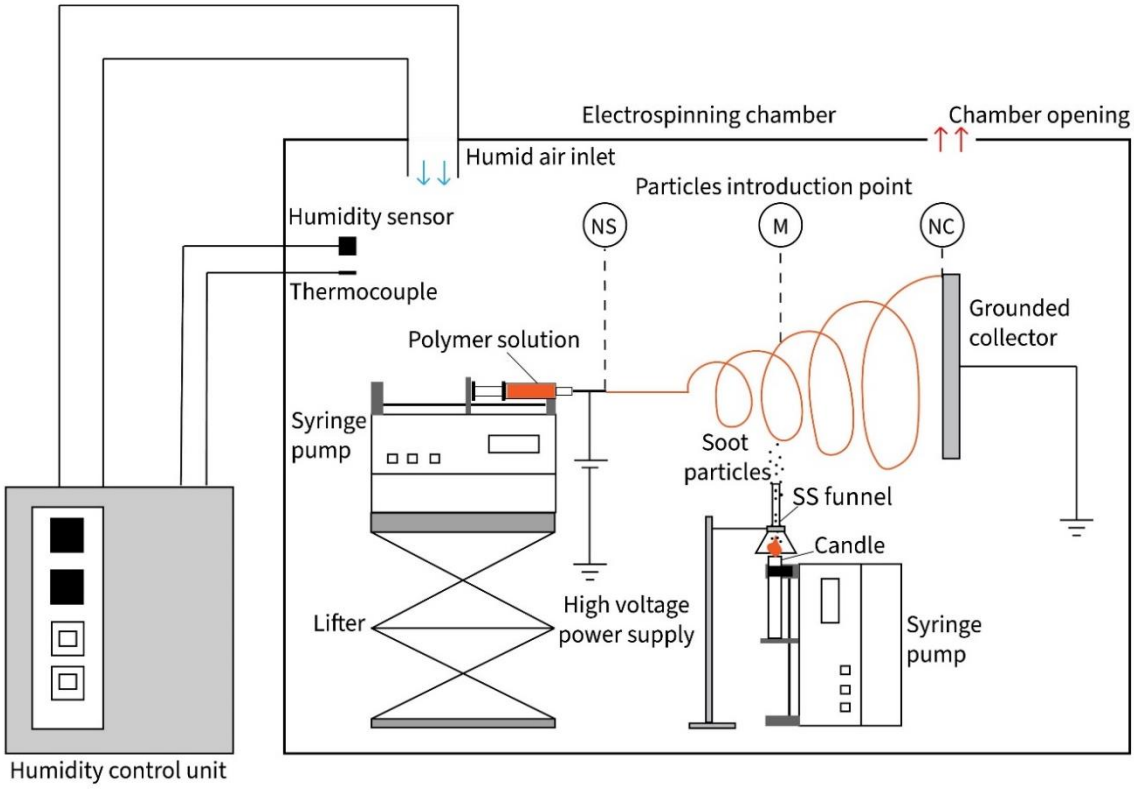

Figure 2. 1 A schematic illustration for simultaneous electrospinning and candle combustion

The candle flame was covered with a stainless-steel funnel to promote incomplete combustion for producing more soot particles. The vertical distance between the tip of the funnel to the center of the needle was kept at 200 mm. Another syringe pump (KDS 100, KD

Scientific Inc., USA) was used to adjust the vertical position of the candle for maintaining the flame position relative to the funnel.

2.2.3 Measurement of the rate of soot particle production from candle burning and approximation of membrane loading efficiency

The number concentration of aerosol particles produced by the candle was measured in real-time using a condensation particle counter (CPC; Model 3775, TSI Inc., USA). A dilution was needed, especially for the particles from the in-membrane production route due to the high particle concentrations. The schematic of particle counting measurement with a dilution line is depicted in Figure 2.2. The gas stream from the electrospinning chamber t 1.5 $L.min^{-1}$ was mixed with air with low particle concentration ($<10^2$ $particles.cm^{-3}$) at a rate of 12.8 $L.min^{-1}$ in the dilution tube. Clean air was obtained through filtration of the air in the experiment room by using a HEPA filter (HEPA-CAP, Whatman, USA) which can retain 99.97% of particles with a diameter larger than or equal to 0.3 μm.

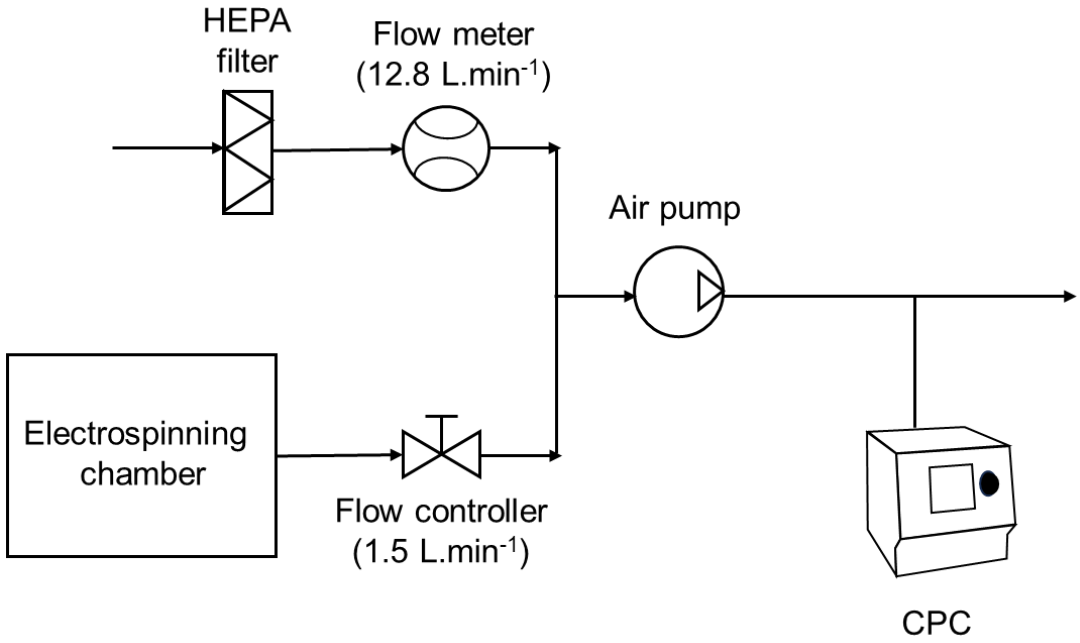

Figure 2.2 Schematic of a dilution line for particle counting of the in-membrane production route using a condensation particle counter (CPC)

The primary particle of candle soot (around 25-30 nm) and its aggregates (a few hundred nanometers) were within the range of detectable particle size of the CPC instrument (4 nm - 3 μm). Aerosol sampling by CPC instrument was conducted for 5 minutes, with a sampling flow rate of 1.5 $L.min^{-1}$.

The rate of soot particle production inside the electrospinning chamber is calculated from CPC measurement results using equations (1) and (2),

$n_c = (n_t - n_0) \times f$…….. (1)

$\dot{n_c} = n_c \times \dot{Q}$ ……..…….. (2)

where n_c is the average number concentration of particles produced by the candle burning per unit volume, n_0 is the average of initial number concentration of particles present in the chamber per unit volume, n_t is the average of total number concentration of particles measured by CPC when the candle was burned inside the electrospinning chamber, and f is the dilution factor, that was 9.5. To obtain the average rate of soot particle production from candle per unit of time ($\dot{n_c}$), the calculated n_c value is multiplied by the sampling flowrate, which was set at 1.5 L.min^{-1}.

The result of the aerosol measurement after multiplication with a diluting factor of 9.5 can be found Figure 2.3 a-d. Number concentration measurement results processed by equation 1 and 2 revealed that the rate of soot particles production by the candle inside the electrospinning chamber on average is around 2.55 x 10^9 ± 3 x 10^7 particles/ min, whereas the rate of soot particles at the outlet of silicone rubber tube for the out-route is around 8.12 x 10^7 ± 2.28 x 10^7 particles/ min, which is 3.19% of the in-route particle rate. The out-membrane production method was carried out to demonstrate the possibility of solar distillation membrane production with a separate electrospinning and particle production site. This method is expected to give more flexibility to control the condition for particle production without interfering with the electrospinning process.

The particle loading efficiency of the membrane (ε) was approximated using equation 3, where n_{et} is the average of the total number of particles measured by CPC during the electrospinning and candle burning experiment and n_{e0} is the average number of particles measured by CPC during electrospinning without candle burning.

$$\varepsilon = \frac{[n_c - ((n_{et} - n_{e0}) \times f)]}{n_c} \times 100\% \text{……..} \qquad (3)$$

It was found that the loading efficiency of the NS-Out, M-Out, and NC-Out membranes is 95.3%, 93.9%, and 98.6%, respectively. The loading efficiency of the NS-In and M-In membranes is close to the loading efficiency of the NS-Out and M-Out membranes, which is 95.8% and 94.3%, respectively. In comparison, the loading efficiency of the NC-In membrane is 91.8%. There is a possibility of particle deposition to the wall of the electrospinning chamber or other surfaces, which cannot be quantified by the present analysis method.

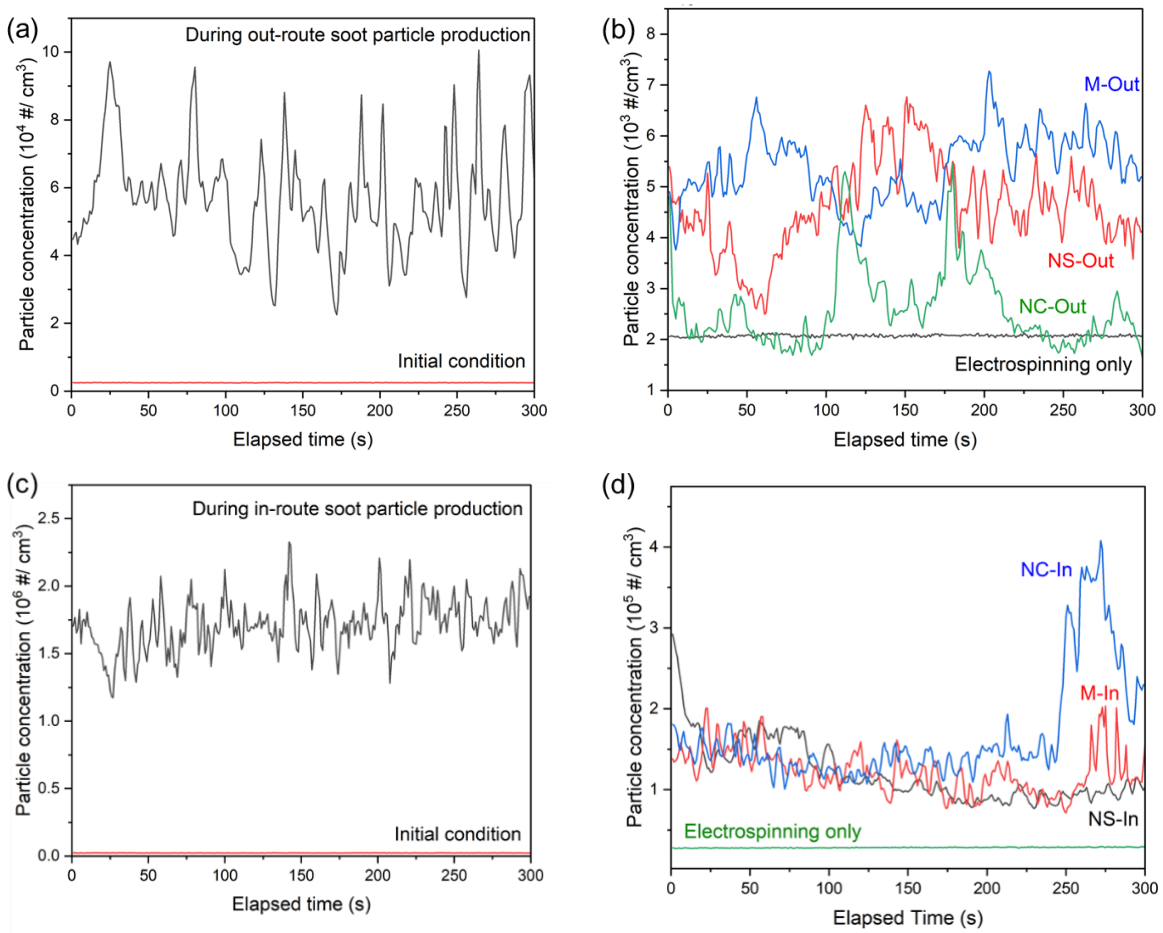

Figure 2.3 Particle number concentration as measured by CPC (a) out-route particle production, (b) remaining particles in the air during different particle introduction points in out-membrane production, (c)in-route particle production, and (d) remaining particles in the air during different particle introduction points in in-membrane production

2.2.4 Membrane characterization

The membrane morphology was observed using a field emission scanning electron microscope (FE-SEM, JSM-6330FS, JEOL, Ltd., Japan). The membrane surfaces were coated with a thin layer of gold nanoparticles using a sputtering device (IB-3 Ion Coater, Eiko Engineering Ltd., Japan) before FE-SEM observation to enhance their electrical conductivity. The fiber diameters were analyzed using an open-source image processing and analysis software, Image J (NIH, USA). The static contact angle of the membrane was measured using a contact angle meter (Drop Master Series, Kyowa Interface Science Co., Ltd., Japan). Membrane reflectance was analyzed using a UV–Vis–NIR microspectrophotometer (MSV-370, Jasco Corp., Japan) at UV-to-NIR wavelength range (190–2500 nm). Each membrane was cut into 20 x 20 mm pieces and put on top of a solid sample holder with an aperture for

reflectance analysis. The sample is mounted perpendicular to the incident light. The instrument uses a double-beam, single-monochromator system with a wavelength accuracy of ± 0.3 nm. Deuterium and halogen lamps (automated switching) are used as the light source in the instrument. The sampling area for the observation is 30 x 30 μm. All measurements were performed by using a gold mirror (Jasco Corp., Japan) as the baseline.

2.2.5 Water evaporation test

The 100 × 100 mm^2 membrane was cut into dozens of 10 × 10 mm^2 samples for water evaporation tests. A saline water sample was prepared by mixing NaCl (Wako Pure Chemical Industries, Ltd., Japan) with distilled water until an electroconductivity of 5 S/m was obtained (approximately 3.24 wt.%). This electroconductivity was similar to that of seawater. Distilled water (0.391 mS/m) obtained from distillation equipment (Eyela Still Ace SA-2100E, Tokyo Rikakikai Co., Ltd., Japan) and saline water were used to test the ability of the membrane to evaporate liquid. The water sample was contained inside a cuvette sealed with an insulator foam to direct the light from the solar light simulator to the liquid body from the top of the cuvette. The membrane floated on the surface of the water. Solar light (Solax, Seric Co., Ltd., Japan) irradiance was controlled at 1 kW/m^2 (1 sun) throughout the experiment. The experimental setup is shown in Figure 2.4a.

The water evaporation rates were determined by measuring the changes in the liquid's mass over time. The initial mass of the liquid was recorded, and after 1 hour of exposure to simulated solar light, the final mass was measured using an analytical balance (HR-202i, AND, Co., Ltd., Japan). To assess the temperature variations, the surface water temperature (5 mm below the surface) and bulk water temperature (40 mm below the surface) were monitored using an ultrafine T-type thermocouple (φ = 0.127 mm, As One Corp., Japan) and recorded by a data logger (midi Logger GL200, Graphtec Co., Ltd., Japan). The temperature measurement setup is depicted in Figure 2.4b. The ability of the membrane to concentrate heat at the water surface was quantitatively evaluated by calculating the area between the water surface temperature curve and the bulk water temperature curve for each membrane. The area between the curves was computed using numerical integration with the trapezoidal rule in MATLAB (Mathworks, USA). The temperature on the membrane surface was captured using a thermal infrared camera (SGT, As One Corp., Japan). The quality of the desalinated water was assessed through a desalination experiment utilizing the NS-In membrane under 1-sun solar light irradiation. The desalinated water was collected using a

custom-built apparatus shown in Figure 2.4c. The electrical conductivity of the desalinated water was measured using a handheld conductivity meter (CM-21P, DKK-TOA Corp., Japan).

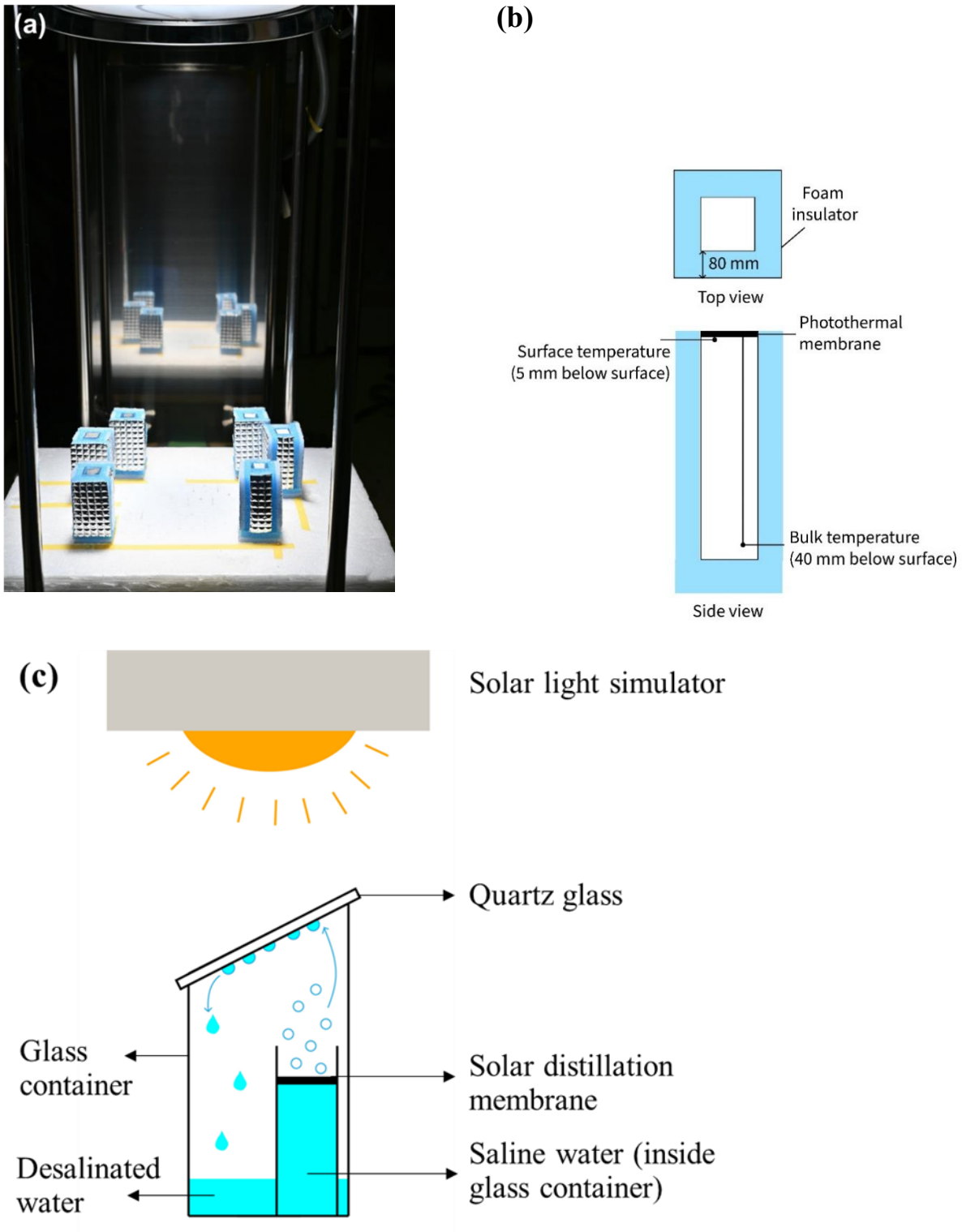

Figure 2.4 (a) Set-up for observation of water evaporation rate, (b) thermocouple position during measurement of bulk and surface water temperature, and (c) homebuilt apparatus to

collect desalinated water from solar distillation membrane

2.2.5 Statistical analysis

To assess the significance of differences within each group of the response variable, a Duncan's multiple range test ($p \leq 0.05$) was performed. The statistical analysis was conducted using IBM SPSS Statistics Software (IBM SPSS Statistics Ver. 25, IBM Corp., USA).

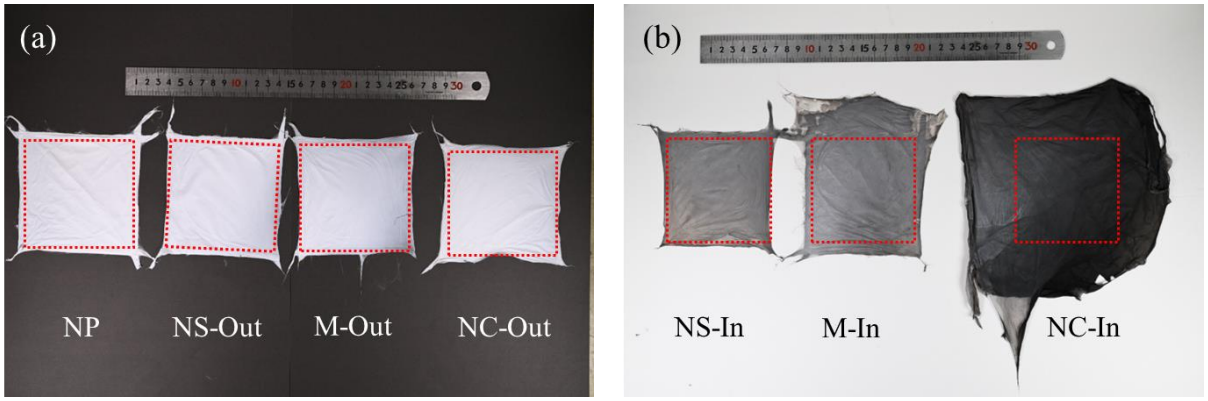

Figure 2.5 Appearance of the as-fabricated electrospun membranes (scale: 30 cm): (a) membranes without particles (NP) and out-membranes at various particle introductionpoints and (b) in-membranes at various particle introduction points; the red dash lines represent the size and shape of the aluminum collector (100 × 100 mm).

2.3 Results and discussion

2. 3. 1 Characterization of the fabricated membranes

The sizes of the membrane without particle deposition (NP), out membrane, and NS-in membrane fit well with that of the grounded aluminum collector (red dashed line), as shown in Figure 2. 5. The M-in and NC-in membranes are 1.45- and 3.63-fold larger in size than the aluminum collector (100 × 100 mm^2), respectively. Candle burning produces both positively and negatively charged soot particles [27]. A high concentration of these charged particles inside the electrospinning chamber may create an electric field that can manipulate the electric field surrounding the charged polymer jet. At the NS position, the electric field of the polymer jet was the strongest [28]. Although a high concentration of soot particles was introduced at the NS-In position, the electric field created by these charged soot particles could not strongly influence the electric field of the polymer jet. This is evidenced by the similar size of the NS-In membrane to that of the NP membrane. The electric field weakened as the jet moved away from the NS position [28] and the electric field created by the charged

soot particles could strongly influence the electric field surrounding the polymer jet. This electric field manipulation may deflect the jet trajectory, resulting in fiber deposition outside of the electrically grounded aluminum collector and producing larger membranes at the M-In and NC-In positions.

One of the key features for achieving high solar distillation performance is high solar light absorption at a wide range of wavelengths [10]. Soot particles absorb solar radiation at all wavelengths [29]. Deposition of soot particles on the polymer membrane is expected to increase the membrane's light absorption and decrease the intensity of the reflected light. This result is confirmed via the reflectance spectra obtained in the UV-to-near-IR (NIR) region, as shown in Figure 2. 6.

NP membrane has a low (below ~3%) light reflectance in the NIR region from 831–2500 nm. The addition of particles from outside the electrospinning chamber further reduces the maximum reflectance in this region to ~1.5%. For in-membranes, the reflectance approaches zero. Light reflectance of all membranes increases at ≤830 nm.

The M-Out membrane shows slightly higher reflectance in the UV-to-visible region compared with other out-membranes. This trend is also similar for the NS-In membrane (compared to M-In and NC-In membranes). At 500 nm, the reflectance of the NP membrane is 22.5%. Reflectance values of the NS-Out, M-Out, and NC-Out membranes are 13.5%, 16.5%, and 14.3%, respectively, whereas those of NS-In, M-In, and NC-In are 3.2%, 0.8%, and 0.7%, respectively. Membrane reflectance at 500 nm must be characterized because maximum solar radiation intensity occurs at approximately this wavelength [30]. As the light reflectance of an opaque body decreases, its light absorption increases. Water has low light absorption in the visible region [9]; therefore, increasing the light absorption in this region using a photothermal membrane can increase the temperature at the air–water interface and improve water distillation performance of the membrane. The decrease in light reflectance at all wavelengths from NP to out-membranes, NS-In, and finally M-In and NC-In membranes indicates the increase in photothermal conversion.

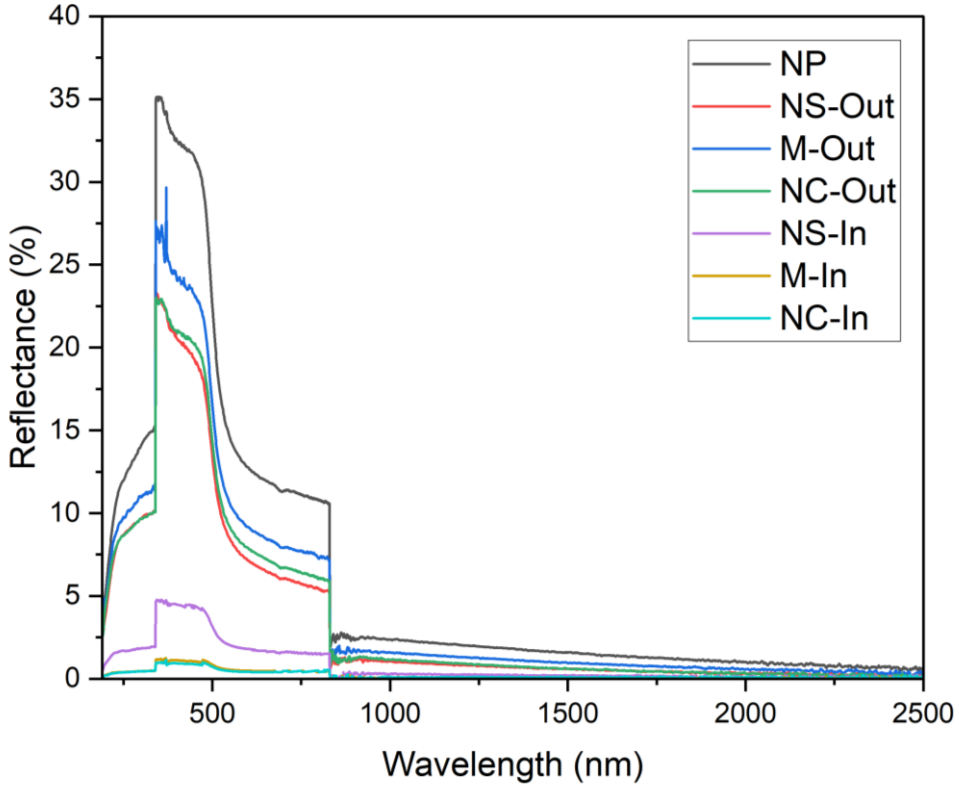

Figure 2. 6 Reflectance spectra of solar distillation membranes in the UV–Vis–NIR region. Automatic switching of light source for reflectance analysis happened at the boundary between NIR to the visible region (~800 nm) and at the boundary between visible to UV region (~300 nm).

Soot particles collected from the tip of the flame are hydrophilic, whereas those collected from the middle of the flame are hydrophobic [31]. These production points of the particles were not strictly controlled herein. Thus, both hydrophilic and hydrophobic particles can be produced and deposited on the membrane. The static contact angles were almost similar for membranes without and with the deposited soot particles (Figure 2. 7). The membrane without any particles had a contact angle of 127.4 ± 4.6°. The contact angle of NS-Out, M-Out, and NC-Out membranes were 130.8 ± 1.3°, 129.8 ± 4.6°, and 127.6 ± 0.3°. The contact angle of NS-In, M-In, and NC-In membranes were 131 ± 0.25°, 128.6 ± 5.2°, and 130.8 ± 5.2°, respectively. The measured contact angles show that all the membranes are hydrophobic.

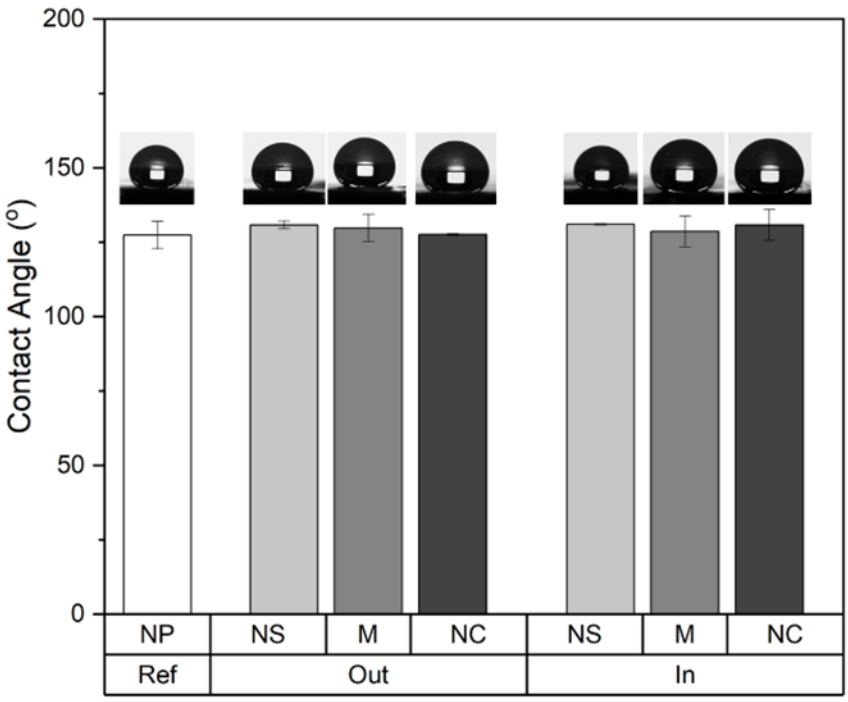

Figure 2. 7 Static contact angle of a water droplet on the electrospun membranes

An additional experiment (Figure A1.1) was conducted by introducing hydrophobic only (mostly), hydrophilic only (mostly), and a mixture of hydrophilic and hydrophobic soot particles into the prefabricated PVDF membrane for 5 min. The result (Figure A1.2 a, b) shows that the contact angles of membranes without particles particle, with hydrophobic-only particles, with hydrophilic-only particles, and those containing both particles are 127.4 ± 4.6°, 138.5 ± 0.6°, 133.6 ± 1.6°, and 135.9 ± 1.8°, respectively. The measured contact angles of all solar distillation membranes (Figure 2.7) were within the range of the contact angles of the membranes with hydrophilic-only particles and those with a mixture of both hydrophilic and hydrophobic particles. This result confirms the presence of hydrophilic soot particle networks in the solar distillation membrane although the contact angle measurement indicates it as hydrophobic.

All membranes in the present study are hydrophobic but have a strong attachment to impinging water [32], see Figure 2.8. This hydrophobic property allows the membrane for self-floating at the air-water interface and to have sufficient contact with the water surface for an efficient heat transfer [14]. The result suggests that the presence of hydrophilic soot particles in a hydrophobic membrane matrix adds merit to the presently fabricated membrane. Hydrophilic particles can assist water supply by providing additional sites for liquid adhesion and promoting the movement of liquid through the membrane pores. The combination of

hydrophobic and hydrophilic properties in solar distillation membranes is expected to promote efficient mass and heat transfer.

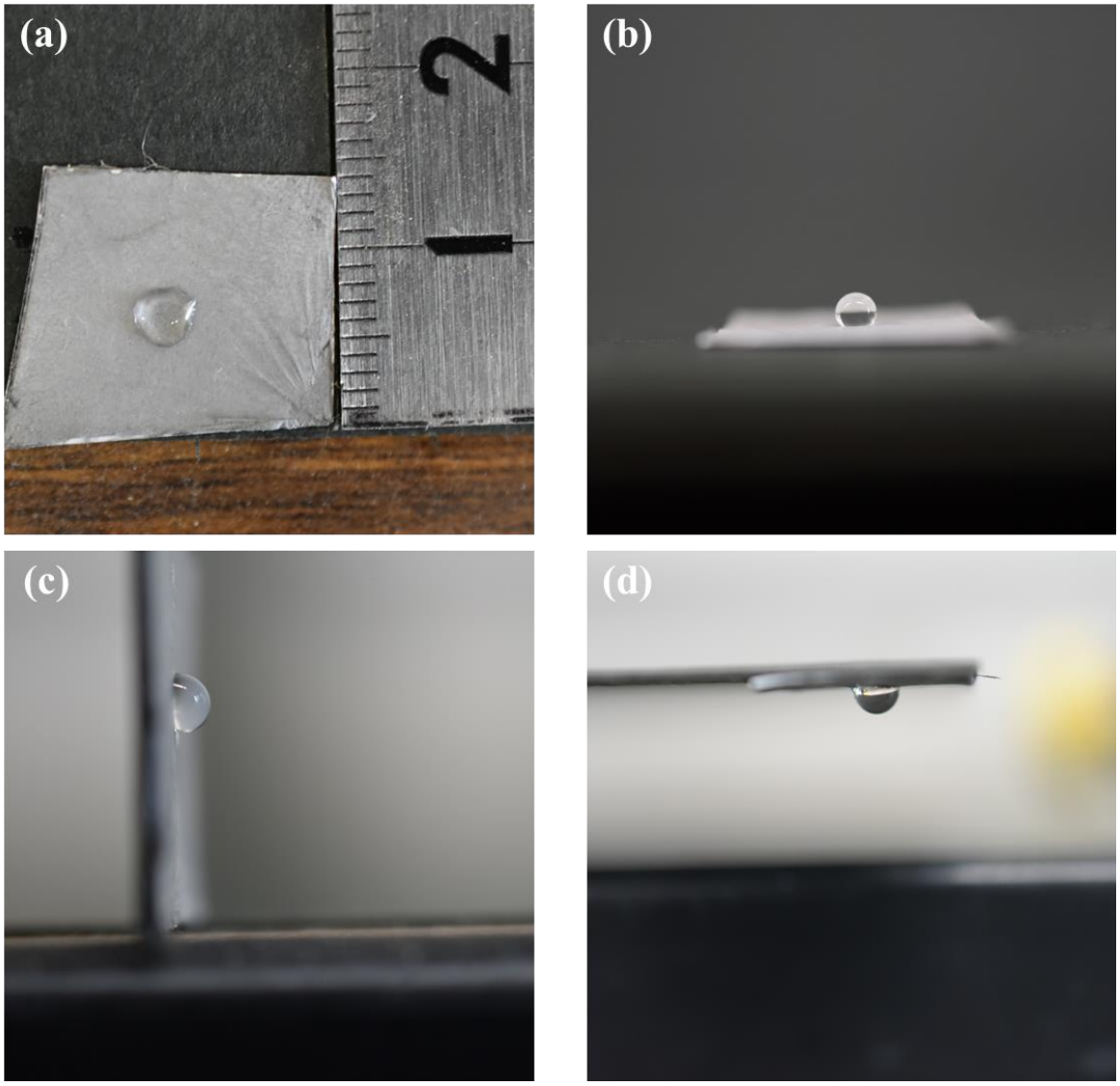

Figure 2.8 Adhesion of water droplet on the surface of a membrane (M-In); top view (a), side view (b), membrane rotated 90º (c), and membrane rotated 180º (d)

The morphology of the particle networks on the polymer fiber and the fiber size distribution are shown in Figure 2. 9. The primary particle size of the soot is ~25–30 nm [33]. Soot particle aggregates ranging from tens to hundreds of nanometers (sub-microns) in size are found on polymer fibers at different concentrations between in-membrane and out-membrane (indicated by red arrows in Figure 2. 9). Micro-meter sized polymer beads were formed in the membrane due to jet instability resulting from the competition between surface tension of the polymer solution and the electrostatic repulsion during electrospinning [34].

These beads occupy around 2.5% of the membrane area (Figure A1.5). Further studies are necessary to understand the influence of the polymer beads on water distillation performance.

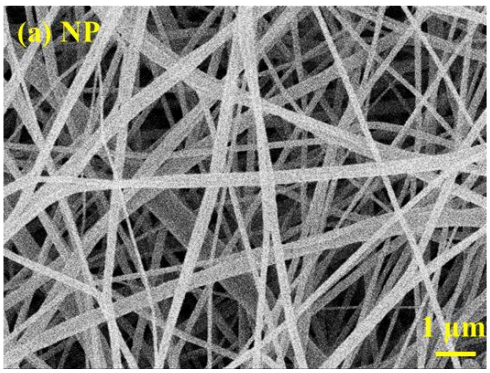

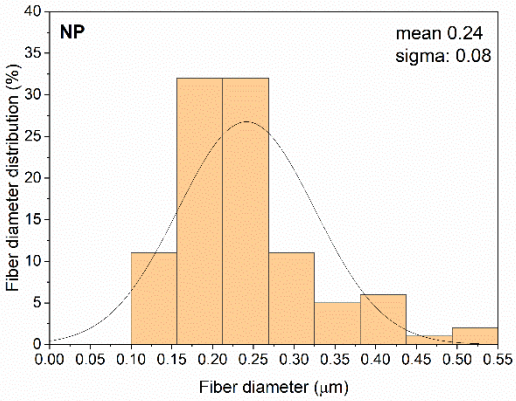

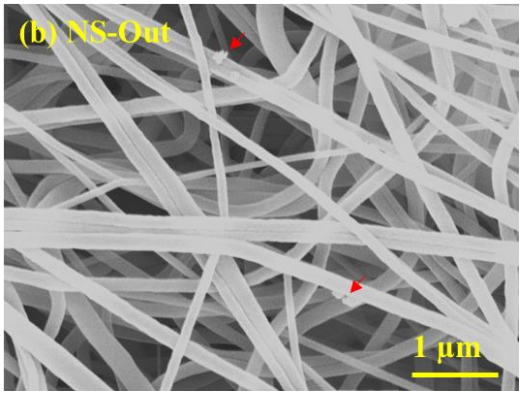

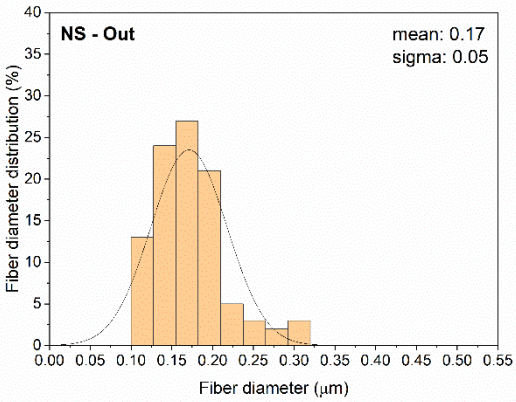

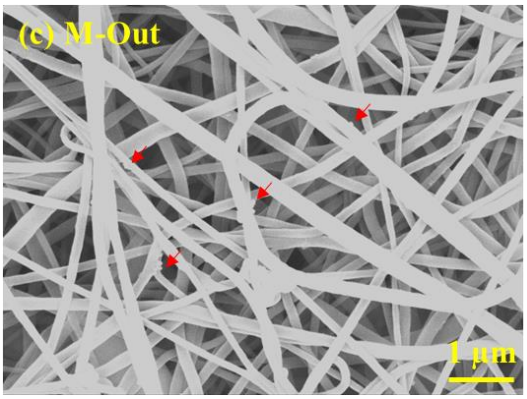

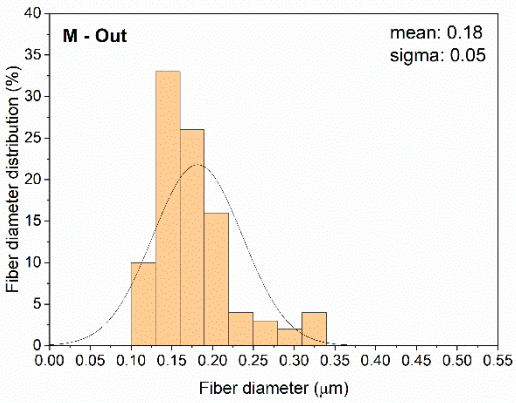

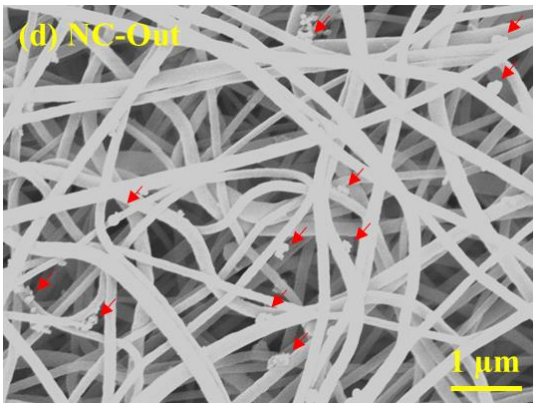
(d) NC-Out
1 µm

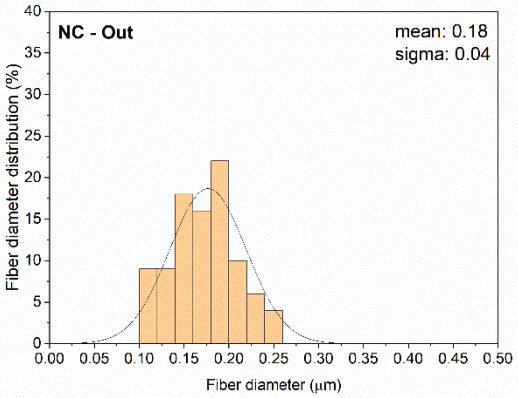
NC - Out
mean: 0.18
sigma: 0.04
Fiber diameter distribution (%)
Fiber diameter (µm)

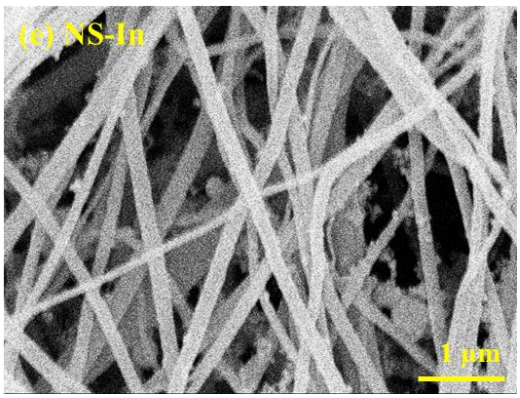
(e) NS-In
1 µm

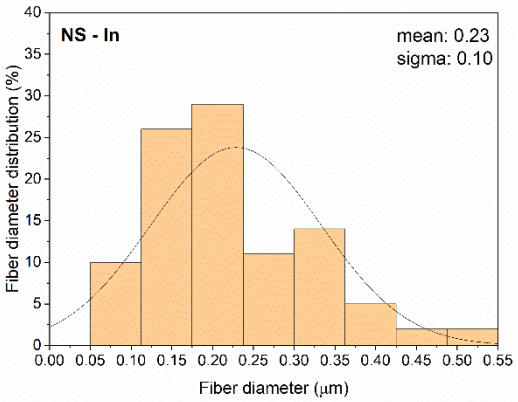
NS - In
mean: 0.23
sigma: 0.10
Fiber diameter distribution (%)
Fiber diameter (µm)

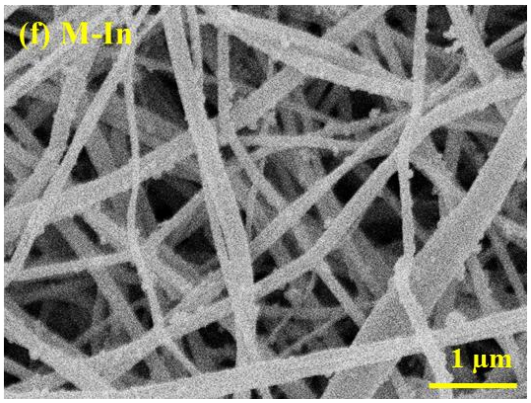
(f) M-In
1 µm

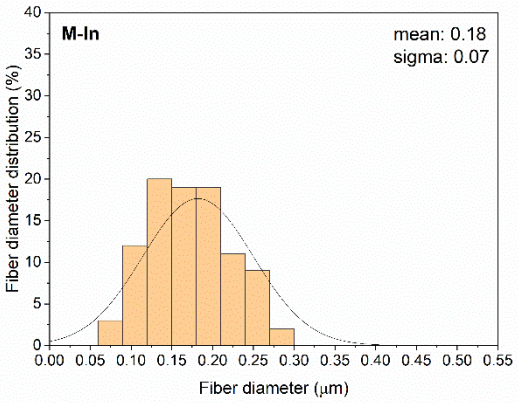
M-In
mean: 0.18
sigma: 0.07
Fiber diameter distribution (%)
Fiber diameter (µm)

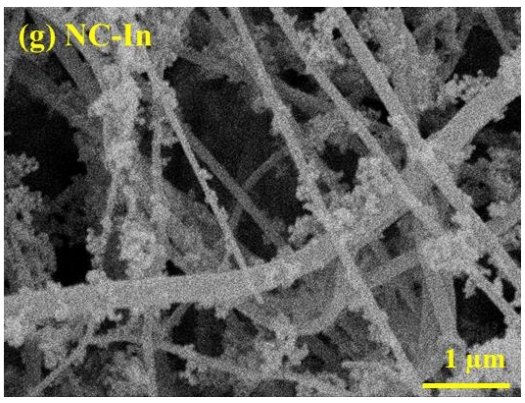
(g) NC-In
1 µm

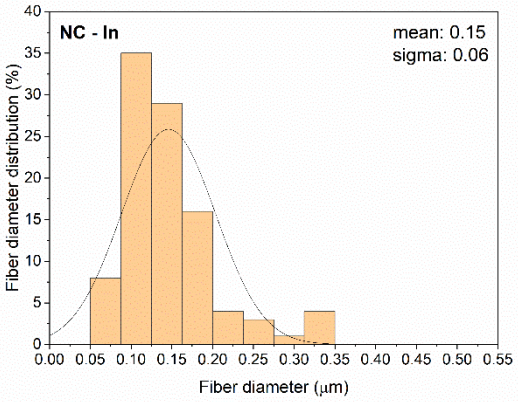
NC - In
mean: 0.15
sigma: 0.06
Fiber diameter distribution (%)
Fiber diameter (µm)

Figure 2. 9 FE-SEM micrographs and fiber diameter distribution of the electrospun membranes; (a) with no particles (NP), (b) with particles introduced near syringe-inside the electrospinning chamber (NS-Out), (c) middle-outside (M-Out), (d) near-collector outside (NC-Out), (e) near syringe-inside (NS-In), (f) middle-Inside (M-In), and (g) near collector-inside (NC-In)

In the case of NS-Out membranes, because the polymer jet having relatively low temperature operation is still wet, we believe that the soot particles can transport into the interior of the polymer jet during electrospinning, resulting in a membrane with photothermal materials positioned inside the polymer fiber. As for M-Out membranes, the polymer jet is relatively drier. Thus, although the particles can still possibly be embedded inside the polymer fiber, a large number of particles are deposited on the polymer surface. Comparison of the FE-SEM micrographs of the NS-Out and M-Out membranes revealed an increase in particle deposition on the surface of the polymer fiber. The number of deposited soot agglomerates in the M-Out membrane is two-fold that in the NS-Out membrane. At the NC position, the polymer jet may reach a stable surface charge and surface tension [35]. Due to the evaporation process during spinning, polymer jet at the NC (near the collector) position is the "driest" and "thinnest" among other samples. making it difficult for the soot particles to be embedded into the fiber's interior and resulting in the high deposition of particles at the fiber's surface (Figures 2. 9c and 2. 9d). The amount of soot agglomerates on the polymer fiber surface in the NC-Out membrane is three-fold that on the M-Out membrane. Supporting FE-SEM observational data of the membrane's cross-section to clarify the position of the particles relative to the fiber for NS-, M-, and NC- membranes can be found in the section 2 of the Appendix 1.

The distribution curve of the fiber diameter in Figure 2.9 shows a decrease in the average fiber diameter of the membranes after soot particles are introduced. On average, the fiber diameter of the out-membranes decreased by ~26% compared to the NP membranes. Whereas NS-In, M-In, and NC-In membranes average diameter decreased by around 4%, 25%, and 37.5% compared to the NP membranes. The decrease in the average fiber diameter for the in-membranes can be attributed to the increase in the temperature of the jet trajectory due to the upstream of heated flow from the burning candle. The average temperature of the jet trajectory at 20 cm above the burning candle inside the electrospinning chamber was ~51^{o}C, higher than outside the chamber (~22^{o}C). This temperature increase can accelerate the evaporation rate of the solvent from the polymer fiber, resulting in a smaller fiber diameter.

However, the average temperature of 51ºC is considerably lower than thermal degradation temperature of the PVDF membrane, which occurs above 400ºC [36]. For out membranes, the temperature of the jet trajectory is around 27ºC. A graph of the temperature profile at the jet trajectory during the experiment is shown in Figure A1.7. The disproportional correlation between the increase in temperature at the jet trajectory and decrease in the average fiber diameter suggests that another mechanism influences the fiber diameter. Electric field manipulation of the polymer jet by charged soot particles may decrease the average polymer fiber diameter. Herein, the fibers could not be cut for performing cross-sectional observations using techniques such as transmission electron microscopy (TEM).

2. 3. 2 Effect of particle position relative to the fiber on the photothermal conversion performance of composites

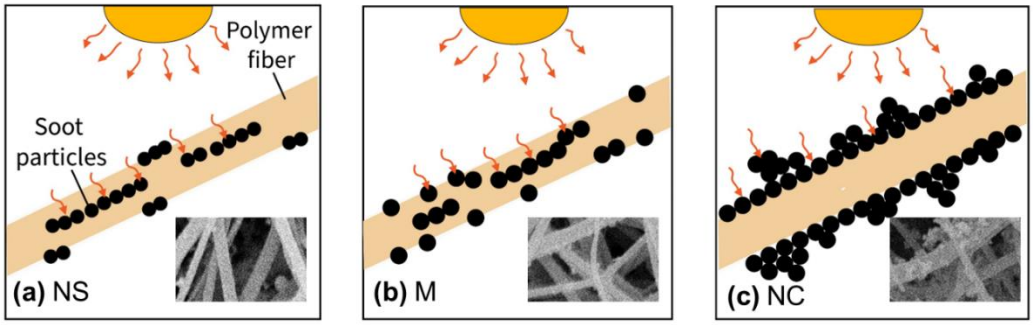

Figure 2. 10 Schematic of particle position on the fiber cross-section based on the particle introduction points and its interactions with the incident light

Figure 2. 10 summarizes the interaction of particles on the polymer fiber with the incident light. In the case wherein soot particles are positioned inside the membrane fiber (NS membrane), incident light will first interact with the polymer fiber surface before reaching the soot particles; the incident light may reflect or scatter before reaching the particles, resulting in reduced photothermal conversion. This process may also occur in the case of the M membrane, with the addition of the possibility that the light directly hits the particles. In the case of the NC membrane, however, the particles are positioned on the surface of the fiber; therefore, the incident light can directly interact with them and can directly absorb and convert into thermal energy without much loss. Surface and bulk water temperature profiles of samples with and without the solar distillation membrane are shown in Figure A1. 8. The differences in the final surface water temperature among the sample without the solar distillation membrane (NM), that with the NP membrane, that with the out membrane, and that with the in-membrane are statistically insignificant. The membrane surface temperature measured using a thermal camera (Figure A1. 9) also shows <1^{o}C difference between the final temperature on the surface of the in membrane and the bulk water temperature of samples without membranes.

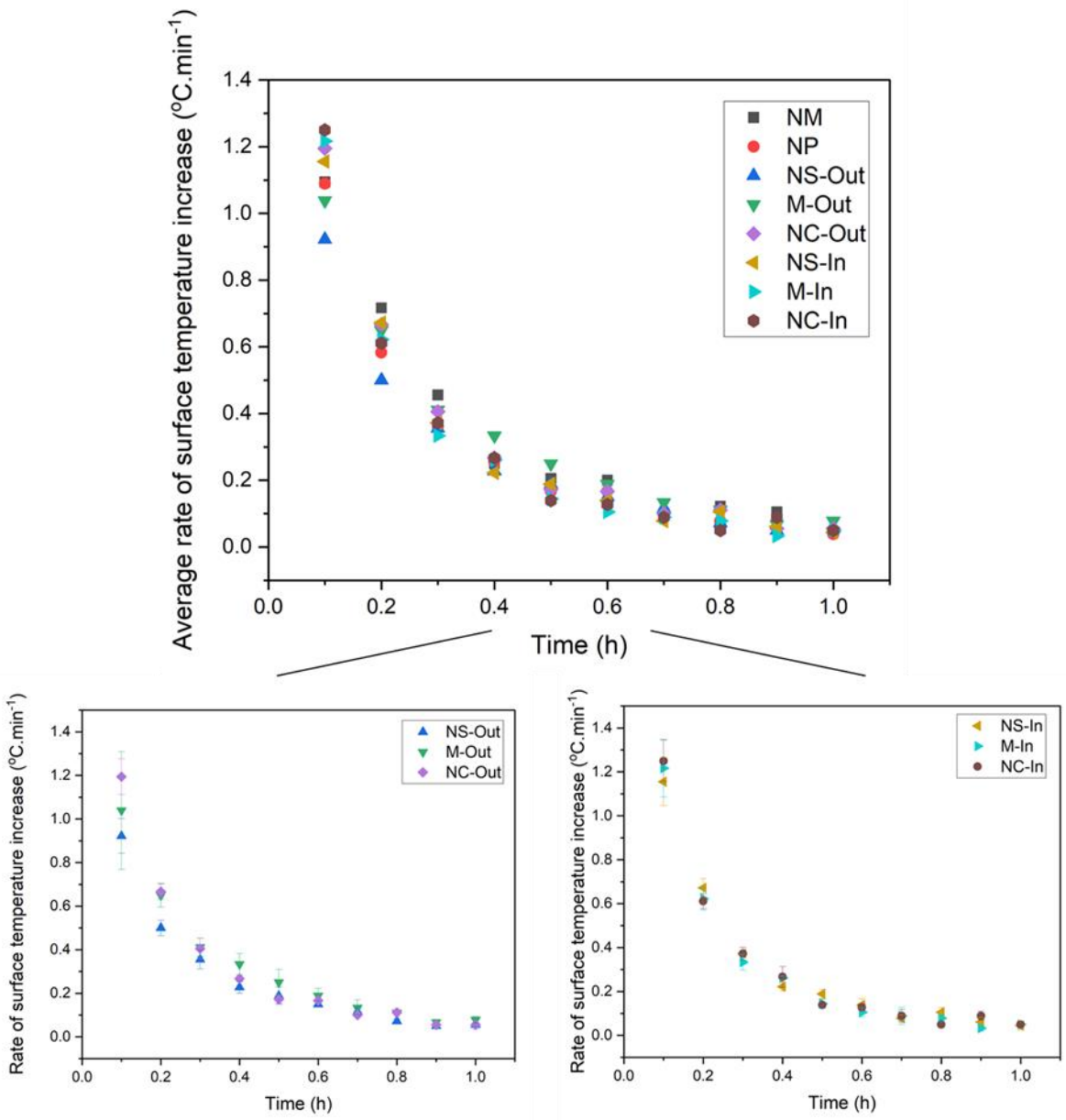

Figure 2. 11 Changes in the rate of surface temperature in different solar distillation membranes. The inset shows the results for out-membranes (left) and in-membranes (right).

To further prove the proposed hypothesis regarding the improvement of photothermal conversion by changing the position of particles on the membrane, the rate of increase in the surface water temperature over the time of solar light irradiation was plotted (Figure 2. 11). The rate of temperature increase for each membrane was obtained by calculating the slope of surface temperature profile curve (Figure A1. 8a) at 10 discrete regions from 0 to 1 h with an interval of 0.1 h.

At the beginning of the experiment (0–0.1 h), the NC-In membrane showed a rapid increase in temperature at a rate of 1.25°C min^{-1} followed by the M-In, NC-Out, NS-In, NM, NP, M-Out, and NS-Out membranes. The rate of temperature increase for the NS-Out membrane was 0.92°C min^{-1}. As time progressed, the solar evaporation system approached equilibrium, decreasing the rate of temperature. Despite a seemingly higher temperature rate of the NC membranes compared to the other membranes at the beginning of the experiment (inset of Figure 2. 11), statistical analysis ($p \leq 0.05$) from the three measured data for each membrane ($n = 3$) shows that the difference in the temperature increase rate among NC, M, and NS membranes is insignificant. Thus, the effect of particle position relative to the polymer fiber on its photothermal conversion performance cannot be confirmed. Notably, the diameter of the polymer fibers (hundreds of nanometer regions) was approximately 4.7–7.2 times larger than those of the primary soot particles (approximately 25–30 nm). Further study with a larger fiber diameter must be conducted to test our hypothesis. Additionally, the insignificant temperature difference between the NP, out-, and in-membranes despite an indication of the improved light absorption performance from the UV–Vis–NIR spectra (Figure 2. 6) possibly confirms heat loss from the membranes to the surrounding. This heat loss may be caused by unoptimized design parameters such as the thickness, pore size, and porosity of membranes. A membrane design that promotes optimal thermal insulation at the surface is desired for solar distillation [10]. The distribution of the thickness of each membrane can be found in Figure A1.10).

The ability of each membrane to localize heat on the surface of a water body was analyzed by plotting the surface and bulk water temperatures, as shown in Figure 2. 12. The heat localization ability of the membranes can be determined based on the temperature gradient between the surface and bulk water temperatures. After 1 h of 1-sun solar light irradiation, the temperature gradient between surface and bulk temperatures for the sample without membrane (NM) and those with NP and NS-Out membranes is only 0.1°C. Temperature gradients for M-Out and NC-Out membranes are 0.7°C and 0.5°C, respectively. The in-membranes have the strongest heat localization ability; the temperature gradient is 1°C for the NS-In membrane and 1.4°C for the M-In and NC-In membranes at the end of the experiment.

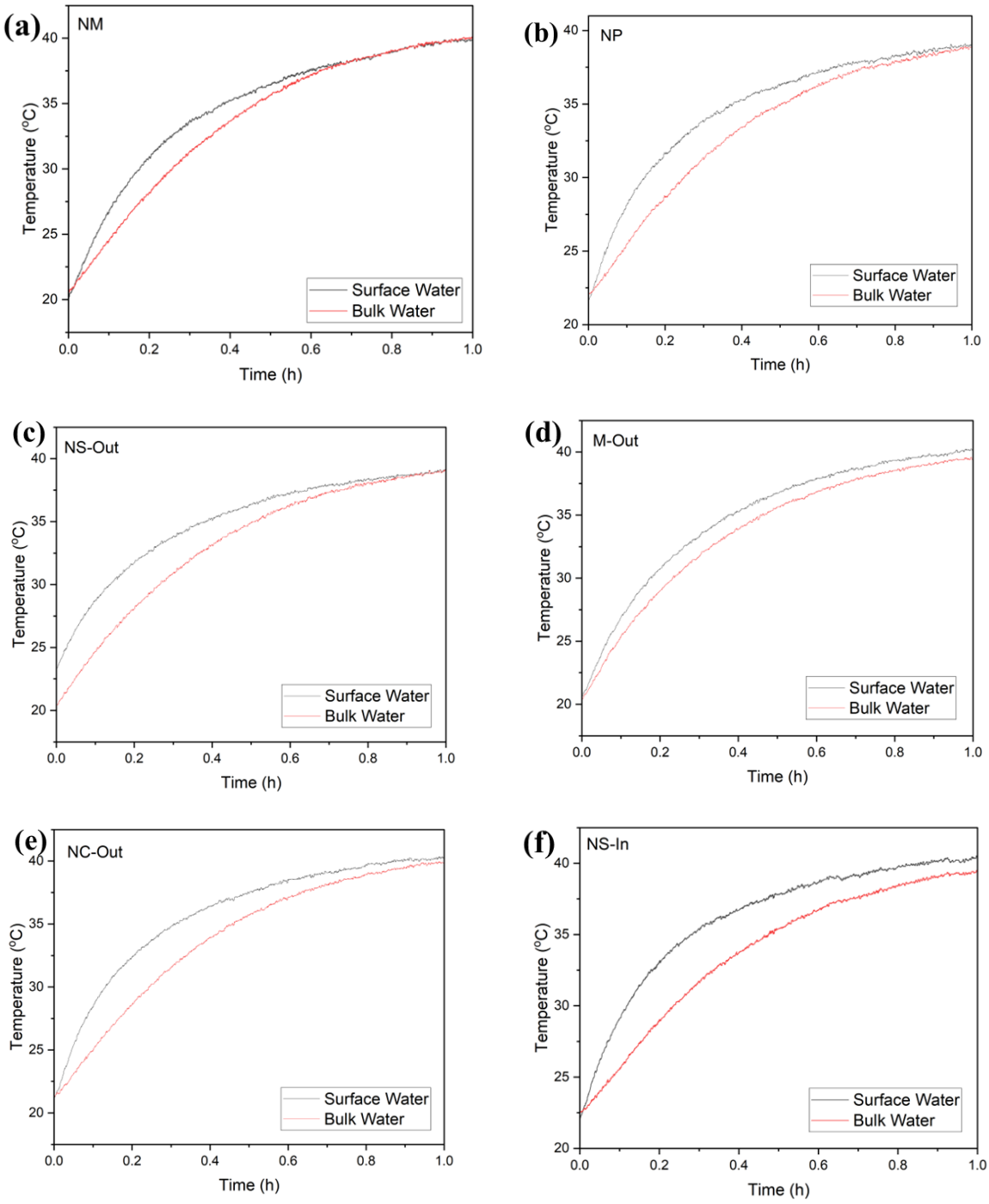
(a)
NM
Temperature (°C)
Time (h)
Surface Water
Bulk Water
(b)
NP
Temperature (°C)
Time (h)
Surface Water
Bulk Water
(c)
NS-Out
Temperature (°C)
Time (h)
Surface Water
Bulk Water
(d)
M-Out
Temperature (°C)
Time (h)
Surface Water
Bulk Water
(e)
NC-Out
Temperature (°C)
Time (h)
Surface Water
Bulk Water
(f)
NS-In
Temperature (°C)
Time (h)
Surface Water
Bulk Water

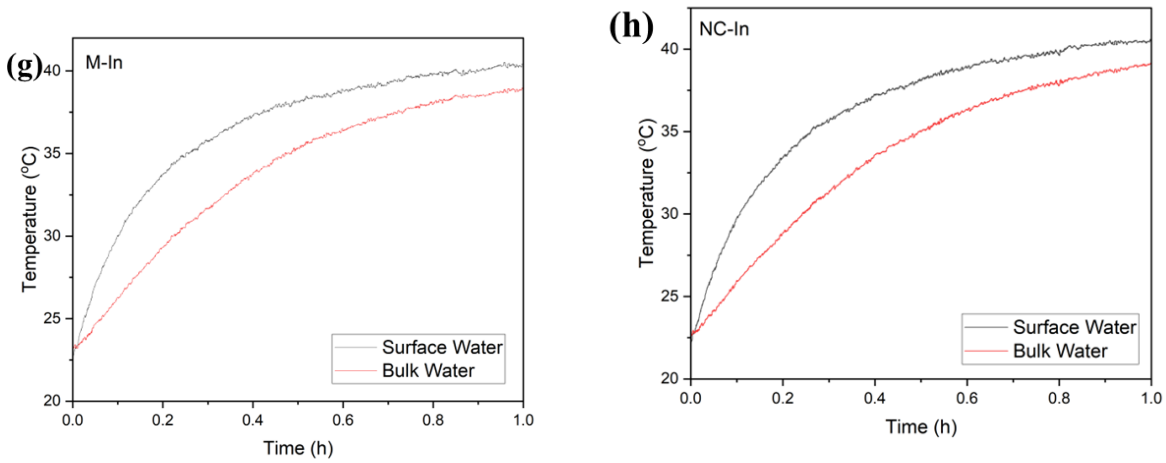

Figure 2. 12 Average surface and bulk water temperature profiles of each sample under 1-sun solar light irradiation.

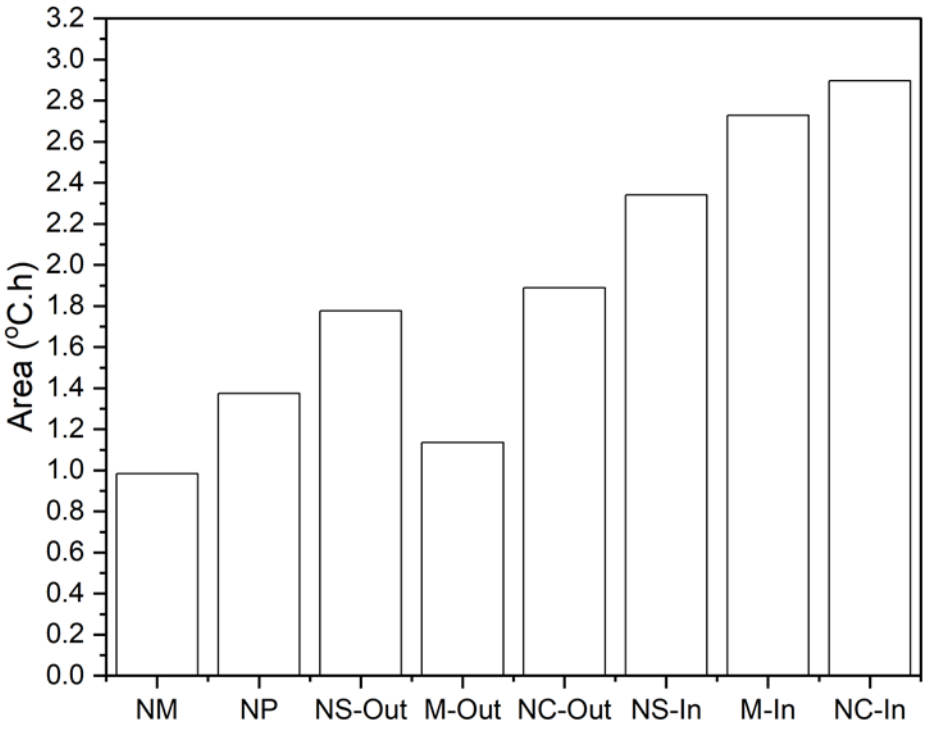

Figure 2. 13 Area between the curve of the surface and bulk water temperatures in Figure 2.12

The area between the curve of surface and bulk water temperatures is calculated to quantitatively compare the heat localization ability of each membrane (Figure 2. 13). Compared with the NM membrane, the NP membrane improves heat localization by 39.7%. NS-Out and NC-Out membranes improve heat localization to 80.6% and 92.2%, respectively. The M-Out membrane only improves it by 15.4%, which can be correlated to its higher

reflectance in the UV–Vis region compared to the other out-membranes. Moreover, the M-Out membrane is the thinnest of all membranes (Figure A1.10), which hampers its heat localization ability. The NS-In, M-In, and NC-In membranes show superior increase in the heat localization ability by 138%, 177.5%, and 194.5%, respectively. The extensive photothermal particle networks of the in-membranes help localize the heat at the water surface.

2. 3. 3 Effect of particle position relative to the fiber on the photothermal conversion performance of composites

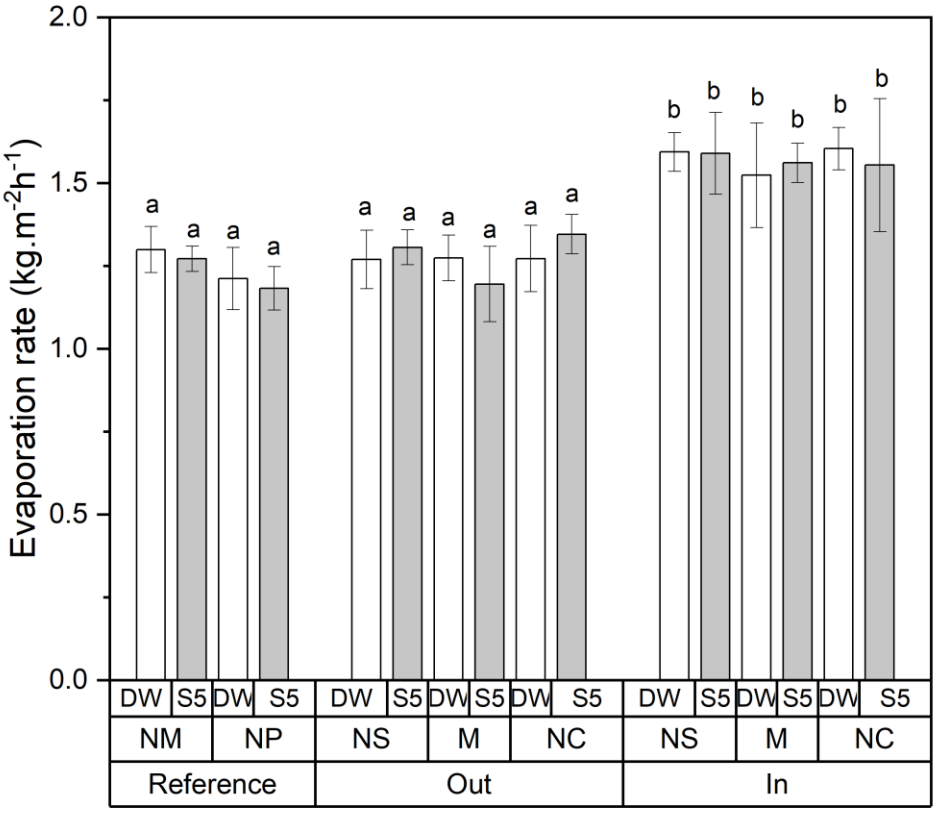

Figure 2. 14 Water evaporation and desalination rates of each sample. DW: distilled water and S5: saline water with an electroconductivity of 5 S/m (32.4 mg of NaCl/ mL distilled water), similar to the electroconductivity of seawater. The letters (a, b) are assigned from the statistical analysis and used to indicate significantly different means

Figure 2. 14 shows the water evaporation and desalination rates of each sample obtained by measuring the change in mass of the test water under each solar distillation membrane at 1-h time interval. Three experiments were conducted for each condition (n = 3). Statistical analysis ($p \leq 0.05$) was conducted by comparing the reference value to the out-

membranes and in-membranes to determine the samples with significant differences in evaporation rates. Samples with the same alphabetical index belong to the same statistical group (not significantly different from each other), whereas those indicated by different alphabetical indexes belong to different statistical groups and are thus significantly different.

The evaporation rate of distilled water (DW) and saline water (S5) without any membranes (NM) were ~1.30 and ~1.27 kg $m^{-2}h^{-1}$, respectively. There are no significant increases in evaporation rate when membranes without particles (NP) and the out-membranes were applied on the water surface based on statistical analysis. The water evaporation rate significantly increases compared to NM by 22.6%, 17.3%, and 23.4% on average for NS-, M-, and NC-In membranes. The desalination rate of the S5 solution was also increasing by 25%, 22.7%, and 22.2% on average for NS-, M-, and NC-In membranes, respectively.

In addition to the superior heat localization ability, the improved evaporation rate of the in-membranes is suspected to be caused by the presence of a network of hydrophilic soot particles within the hydrophobic membrane (explained in previous section), which facilitates water transport into the membrane. Water affinity of hydrophilic soot particles may be lost in cases wherein soot particles are generated outside the electrospinning chamber (out-membranes). An aerosol measurement study [37] found that the exposure of conductive silicone rubber tubes to high temperatures can emit organic contaminants containing siloxane that can be adsorbed by soot particles passing through the tube. These adsorbed contaminants make the soot particles hydrophobic.

Herein, the water evaporation rate under 1-sun solar irradiation is comparable or higher (~ 1.16 kg $m^{-2}h^{-1}$) than that reported for cellulose filter paper membranes embedded with the candle-derived soot particles obtained using the two-step method [18]. The electroconductivity of water after the desalination process using the NS-In membrane under 1-sun solar irradiation was 0.115 mS/m, which is below the maximum allowable electrical conductivity standard for drinking water reported by WHO [38].

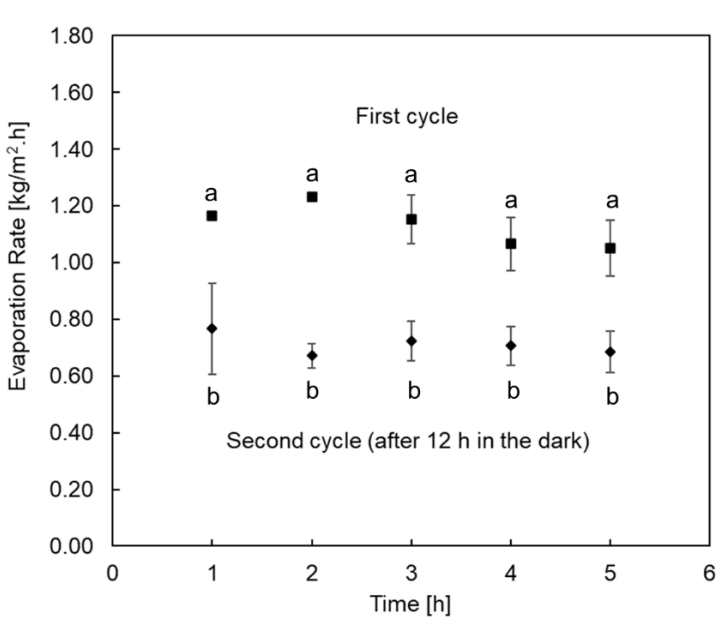

Figure 2. 15 Two cycles of saline water desalination using a photothermal membrane (NS-In). The letters (a, b) are assigned from the statistical analysis and used to indicate significantly different means.

The self-recyclability of photothermal membranes is an important factor affecting their practical applications. Figure 2. 15 shows two cycles of desalination using the NS-In membrane. The first cycle ends after 5 h of desalination. The second cycle begins after 12 h of remaining in the dark (without light), and then continues for the next 5 h (at 1 sun). No significant decrease of evaporation rate was observed during the 5 h of each cycle. The membrane performance significantly decreased within 12 h of being let in the dark. The self-recyclability of the membrane [18] was not observed herein because the salt solution could flow into the pores of the membrane through the hydrophilic soot particle network even under dark conditions. Because of the absence of sunlight, the water evaporation rate significantly decreases and the temperature gradient in the water body becomes nonexistent. This condition allows the salt solution to be stationary and is retained in the membranes pores for a long time. This long residence time allows the salt crystal to grow within the membrane. The salt crystal is difficult to redissolve, particularly when the membrane matrix (polymer fibrous matrix) is hydrophobic. The cycle performance of the membranes in the present study is summarized in Table A1.1 in the appendix and compared with that of other related studies. Figure 2. 16 shows the growth of salt crystals in the photothermal membrane pores.

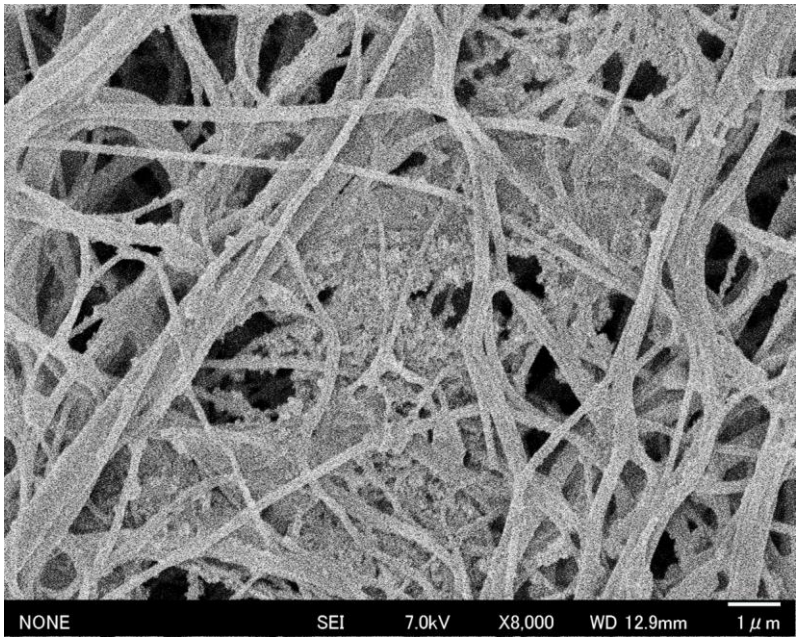

Figure 2. 16 Growth of salt particles in the photothermal membrane pores.

No soot particles were visibly detected to be detached from the solar distillation membrane. Additional analysis based on the absorbency of the water body (the remaining water that were not evaporated during evaporation test) was conducted to detect soot particle release from the membrane to the water body (see section 8 of Appendix 1). This analysis was conducted to judge whether the decrease in evaporation rate is strongly influenced by the loss of photothermal particles from the membrane. It was found that significant change in absorbance value in comparison to the reference was detected after 5 hours of evaporation test in distilled water (Figure A1.12). The conversion of the change in absorbance value to particle concentration was obtained by using a conversion curve (Figure A1.11). It was found that the highest concentration of particle loss was around 1.6 ppm in the test water where NS-Out and M-Out membrane was applied. The membrane which is suspected to have the highest number of particles at the fiber surface (NC-In), shows particle loss of around 0.9 ppm after 5 hours. This suggests that the soot particles can be strongly bonded to the fiber surface using the proposed one-step membrane fabrication method.

The result of the absorbance test for the remaining S5 (saline water) solutions after the first and second cycle of evaporation tests are shown in Figure A1.14 and A1.15. The results indicate that there is a decrease in absorbance of most of the samples where significant change of absorbance was detected in comparison to the absorbance value of the reference membrane (NM). A conversion curve relating the change in absorbance with the concentration of carbonaceous particles in the solution cannot be established due to the

instability of soot particles in S5 solution. However, given no observable particle sedimentation and no color change during the test, we believe that there was only little particle loss, as obtained on the result with evaporation test in distilled water. The role of salt crystal growth in the pores of the membrane is more dominant in causing a decrease in the desalination rate after the light-dark cycle rather than the detachment of soot particles from the membrane. Further study is required to investigate the mechanism of particle loss from the polymer membrane.

2.4 Conclusion

In this chapter, soot particles were embedded in fibrous polymer membranes using a novel method that involved burning candles and electrospinning simultaneously. Using this method, solar distillation membranes can be fabricated in a single step without any additional chemicals. The position of the soot particles was controlled relative to the polymer fiber by changing the location of the aerosol particle injection through the polymer jet. Results revealed that the position of the soot particles did not affect the photothermal conversion performance; moreover, the fiber diameter was in the range of hundreds of nanometers. By applying the as-fabricated solar distillation membranes on the water surface, a heat localization enhancement of 194.5% was achieved compared to the water samples without a membrane. Under 1-sun solar irradiation, the NC-Out membranes exhibited water evaporation and desalination rates of 1.60 and 1.59 kg. $m^{-2}h^{-1}$. The present study also has some limitations that need to be addressed in future studies. For instance, the stability and durability of the membranes under long-term exposure to solar irradiation and seawater were not evaluated. Additionally, some key parameters such as polymer concentration, nozzle-to-collector distance, particle-to-fiber loading ratio defining the properties of the membranes were not yet optimized. Future studies should focus on these aspects to improve the applicability and feasibility of the novel method and the resulting membranes for solar water desalination.

2.5 References

[1] M.M. Mekonnen, A.Y. Hoekstra, Four billion people facing severe water scarcity - Supplementary, Sci. Adv. 2 (2016) e1500323. https://doi.org/10.1126/sciadv.1500323.

[2] I.A. Shiklomanov, J.C. Rodda, World water resources at the beginning of the twenty-first century, Cambridge University Press, Cambridge, 2003.

[3] United Nations, The United Nations World Water Development Report 2022: Groundwater: Making the invisible visible, Paris, 2022. https://doi.org/10.1111/1740-9713.01654.

[4] W. Aeschbach-Hertig, T. Gleeson, Regional strategies for the accelerating global problem of groundwater depletion, Nat. Geosci. 5 (2012) 853–861. https://doi.org/10.1038/ngeo1617.

[5] United Naions World Water Assessment Programme (WWAP), The United Natios World Water Development Report 2018: Nature-Based Solutions for Water, Paris, 2018.

[6] E. Jones, M. Qadir, M.T.H. van Vliet, V. Smakhtin, S. mu Kang, The state of desalination and brine production: A global outlook, Sci. Total Environ. 657 (2019) 1343–1356. https://doi.org/10.1016/j.scitotenv.2018.12.076.

[7] N.C. Darre, G.S. Toor, Desalination of Water: a Review, Curr. Pollut. Reports. 4 (2018) 104–111. https://doi.org/10.1007/s40726-018-0085-9.

[8] H.T. Do Thi, T. Pasztor, D. Fozer, F. Manenti, A.J. Toth, Comparison of desalination echnologies using renewable energy sources with life cycle, PESTLE, and multi-criteria decision analyses, Water. 13 (2021) 3023.

[9] H.M. Wilson, Tushar, S. Raheman Ar, N. Jha, Plant-derived carbon nanospheres for high efficiency solar-driven steam generation and seawater desalination at low solar intensities, Sol. Energy Mater. Sol. Cells. 210 (2020) 110489. https://doi.org/10.1016/j.solmat.2020.110489.

[10] N.S. Fuzil, N.H. Othman, N.H. Alias, F. Marpani, M.H.D. Othman, A.F. Ismail, W.J. Lau, K. Li, T.D. Kusworo, I. Ichinose, M.M.A. Shirazi, A review on photothermal material and its usage in the development of photothermal membrane for sustainable clean water production, Desalination. 517 (2021) 115259. https://doi.org/10.1016/j.desal.2021.115259.

[11] Z. Wang, Y. Liu, P. Tao, Q. Shen, N. Yi, F. Zhang, Q. Liu, C. Song, D. Zhang, W. Shang, T. Deng, Bio-inspired evaporation through plasmonic film of nanoparticles at the air-water interface, Small. 10 (2014) 3234–3239. https://doi.org/10.1002/smll.201401071.

[12] M.M. Ghafurian, H. Niazmand, F.T. Dastjerd, O. Mahian, A study on the potential of carbon-based nanomaterials for enhancement of evaporation and water production, Chem. Eng. Sci. 207 (2019) 79–90. https://doi.org/10.1016/j.ces.2019.05.043.

[13] I. Zada, W. Zhang, P. Sun, M. Imtiaz, N. Iqbal, U. Ghani, R. Naz, Y. Zhang, Y. Li, J. Gu, Q. Liu, D. Pantelić, B. Jelenković, D. Zhang, Superior photothermal black TiO_2 with random size distribution as flexible film for efficient solar steam generation, Appl. Mater. Today. 20 (2020) 100669. https://doi.org/10.1016/j.apmt.2020.100669.

[14] L. Zhang, B. Tang, J. Wu, R. Li, P. Wang, Hydrophobic Light-to-Heat Conversion Membranes with Self-Healing Ability for Interfacial Solar Heating, Adv. Mater. 27 (2015) 4889–4894. https://doi.org/10.1002/adma.201502362.

[15] H.M. Wilson, S. Raheman A. R, H.W. Lim, S.J. Lee, Conversion of Hazardous Diesel Soot Particles into a Novel Highly Efficient 3D Hydrogel for Solar Desalination and Wastewater Purification, ACS Omega. 8 (2022) 2740-2751. https://doi.org/10.1021/acsomega.2c07430.

[16] L. Zhang, B. Bai, N. Hu, H. Wang, Low-cost and facile fabrication of a candle soot/adsorbent cotton 3D-interfacial solar steam generation for effective water evaporation, Sol. Energy Mater. Sol. Cells. 221 (2021) 110876. https://doi.org/10.1016/j.solmat.2020.110876.

[17] A.M. Saleque, S. Ma, S. Ahmed, M.I. Hossain, W. Qarony, Y.H. Tsang, Solar Driven Interfacial Steam Generation Derived from Biodegradable Luffa Sponge, Adv. Sustain. Syst. 5 (2021) 2000291. https://doi.org/10.1002/adsu.202000291.

[18] M.U. Rashid, Z. Tahir, S. Kim, J.I. Jang, Y.S. Kim, Selective Deposition of Candle Soot on a Cellulose Membrane for Efficient Solar Evaporation, ACS Omega. 6 (2021) 31366–31374. https://doi.org/10.1021/acsomega.1c05348.

[19] C. Xiao, W. Liang, L. Chen, J. He, F. Liu, H. Sun, Z. Zhu, A. Li, Janus Poly(ionic liquid) Monolithic Photothermal Materials with Superior Salt-Rejection for Efficient Solar Steam Generation, ACS Appl. Energy Mater. 2 (2019) 8862–8870. https://doi.org/10.1021/acsaem.9b01856.

[20] H.M. Wilson, S. Rahman AR, T. Garg, N. Jha, Recycling of hazardous diesel soot particles into a high performance solar evaporation device, Appl. Surf. Sci. 487 (2019)

951–961. https://doi.org/10.1016/j.apsusc.2019.05.080.

[21] H.M. Wilson, S. Rahman A.R., A.E. Parab, N. Jha, Ultra-low cost cotton based solar evaporation device for seawater desalination and waste water purification to produce drinkable water, Desalination. 456 (2019) 85–96. https://doi.org/10.1016/j.desal.2019.01.017.

[22] H. Sun, Y. Li, J. Li, Z. Zhu, W. Zhang, W. Liang, C. Ma, A. Li, Facile Preparation of a Carbon-Based Hybrid Film for Efficient Solar-Driven Interfacial Water Evaporation, ACS Appl. Mater. Interfaces. 13 (2021) 33427–33436. https://doi.org/10.1021/acsami.1c06226.

[23] F. Trupp, M. Barella, R. Cibils, S. Goyanes, In situ syringe rotation system for heavy microparticle suspension stability in electrospinning technique, Rev. Sci. Instrum. 94 (2023). https://doi.org/10.1063/5.0131947.

[24] T. Lei, J. Xiong, J. Huang, T. Zheng, X. Cai, Facile transformation of soot nanoparticles into nanoporous fibers via single-step electrospinning, AIP Advances, 7 (2017) 085212. https://doi.org/10.1063/1.4996397.

[25] X. Li, T. Xu, Z. Liang, V.S. Amar, R. Huang, B.K. Maddipudi, R. V. Shende, H. Fong, Simultaneous electrospinning and electrospraying for the preparation of a precursor membrane containing hydrothermally generated biochar particles to produce the value-added product of carbon nanofibrous felt, Polymers (Basel). 13 (2021) 1–10. https://doi.org/10.3390/polym13050676.

[26] M. Shimada, Characteristics and Behavior of Nanoparticles and Its Dispersion Systems: Phoretic Phenomena, in: M. Naito, T. Yokoyama, K. Hosokawa, K. Nogi (Eds.), Nanoparticle Technol. Handb., Third Edit, Elsevier B.V., 2018: pp. 113–176. https://doi.org/10.1016/B978-0-444-64110-6.00003-2.

[27] M.D. Wright, A.P. Fews, P.A. Keitch, D.L. Henshaw, Small-ion and nano-aerosol production during candle burning: Size distribution and concentration profile with time, Aerosol Sci. Technol. 41 (2007) 475–484. https://doi.org/10.1080/02786820701225812.

[28] G. Collins, J. Federici, Y. Imura, L.H. Catalani, Charge generation, charge transport, and residual charge in the electrospinning of polymers: A review of issues and

complications, J. Appl. Phys. 111 (2012) 044701. https://doi.org/10.1063/1.3682464.

[29] P. Chylek, S.G. Jennings, R. Pinnick, Aerosols: Soot, in: G.R. North, J. Pyle, F. Zhang (Eds.) Encycl. Atmos. Sci. Second 2nd Edition (2015) 86–91. https://doi.org/10.1016/B978-0-12-382225-3.00375-3.

[30] C.J. Cleveland, C. Morris Eds., Section 10 - Solar, in: Handb. Energy, Elsevier, 2013: pp. 405–450. https://doi.org/10.1016/B978-0-08-046405-3.00010-3.

[31] F. Faizal, M.P. Khairunnisa, S. Yokote, I.W. Lenggoro, Carbonaceous nanoparticle layers prepared using candle soot by direct- and spray-based depositions, Aerosol Air Qual. Res. 18 (2018) 856–865. https://doi.org/10.4209/aaqr.2017.10.0426.

[32] R.N. Wenzel, Resistance of solid surfaces to wetting by water, Ind. Eng. Chem. 28 (1936) 988–994. https://doi.org/10.1021/ie50320a024.

[33] J. Pagels, A. Wierzbicka, E. Nilsson, C. Isaxon, A. Dahl, A. Gudmundsson, E. Swietlicki, M. Bohgard, Chemical composition and mass emission factors of candle smoke particles, J. Aerosol Sci. 40 (2009) 193–208. https://doi.org/10.1016/j.jaerosci.2008.10.005.

[34] X. Hu, X. Chen, M. Giagnorio, C. Wu, Y. Luo, C. Hélix-Nielsen, P. Yu, W. Zhang, Beaded electrospun polyvinylidene fluoride (PVDF) membranes for membrane distillation (MD), Journal of Membrane Science, 661 (2022) 120850. https://doi.org/10.1016/j.memsci.2022.120850.

[35] Y. Yang, Z. Jia, J. Liu, Q. Li, L. Hou, L. Wang, Z. Guan, Effect of electric field distribution uniformity on electrospinning, J. Appl. Phys. 103 (2008) 104307. https://doi.org/10.1063/1.2924439.

[36] M. Kim, Y.S. Wu, E.C. Kan, J. Fan, Breathable and flexible piezoelectric ZnO@PVDF fibrous nanogenerator for wearable applications, Polymers (Basel). 10 (2018) 745. https://doi.org/10.3390/polym10070745.

[37] M.T. Timko, Z. Yu, J. Kroll, J.T. Jayne, D.R. Worsnop, R.C. Miake-Lye, T.B. Onasch, D. Liscinsky, T.W. Kirchstetter, H. Destaillats, A.L. Holder, J.D. Smith, K.R. Wilson, Sampling artifacts from conductive silicone tubing, Aerosol Sci. Technol. 43 (2009) 855–865. https://doi.org/10.1080/02786820902984811.

[38] Y. Meride, B. Ayenew, Drinking water quality assessment and its effects on residents

health in Wondo genet campus, Ethiopia, Environ. Syst. Res. 5 (2016) 1–7. https://doi.org/10.1186/s40068-016-0053-6.

[39] R. Dallaev, T. Pisarenko, D. Sobola, F. Orudzhev, S. Ramazanov, T. Trčka, Brief Review of PVDF Properties and Applications Potential, Polymers (Basel). 14 (2022) 1–29. https://doi.org/10.3390/polym14224793.

Chapter 3: Heat and Flow Phenomena in Liquid-Filled Porous Tobacco Substrate: Visualization by Optical Coherence Tomography

Abbreviation

CT	Computed tomography
HTP	Heated tobacco product
NIR	Near infrared
NMR	Nuclear magnetic resonance
SD	Standard deviation
SD-OCT	Spectral domain-optical coherence tomography
SLD	Superluminescent diode

3.1 Introduction

Visualizing liquid transport in porous media is important in applications such as microfluidic analytical devices [1], food packaging [2], and inkjet printing [3]. Visualizing *in-plane* liquid spreading is common [4-6], but visualization of *trans-plane* liquid penetration is challenging due to factors such as the complex geometry of the multilayered porous structure and liquid volatility [7].

To help visualize liquid transmission in multilayered planes, previous studies have proposed methods such as X-ray computed tomography [8], micro-CT [9], nuclear magnetic resonance (NMR) [10], digital camera-based light reflection measurement [11], light transmission and impedance spectroscopy [3], micromodels combined with confocal laser scan microscopy [12], and optical coherence tomography (OCT) [13-16]. X-ray and micro-CT offer non-destructive visualization of liquid flow in porous media, such as smart textiles [8] and powder beds [9],with a spatial resolution of around 5-150 μm [17]. However, repeated observations may cause potential health hazards due to exposure to X-ray radiation. NMR is another example of a non-invasive imaging technique. Nonetheless, the quality of the obtained data is heavily dependent on the intricate sample preparation, which can limit the practicality of this approach. Digital camera-based imaging technique offers practicality and a wide range of applicability. Nevertheless, it mainly relies on a 2D surface imaging system which may not accurately capture the behavior of liquid flow in a 3D system. Micromodels are often adapted to study fluid flow and transport phenomena at the pore-scale level of an opaque porous media [12]. The transparent nature of a micromodel allows a straightforward observation of liquid flow in the pore channel. However, the simplification of a pore network by the fabricated pore models raises an issue with the accuracy of its modeling in comparison to a complex natural system.

OCT captures cross-sectional images of materials by emitting a beam of light into the sample and measuring the intensity of the light that scattered back to the detector. OCT can reach a penetration depth of up to 1 mm with a resolution of up to 1 μm [18]. In previous studies, OCT has been used to monitor viscous liquid sorption into paper [13], drying of colloid droplets [15, 16], and evaporation of water from porous tobacco substrates [14]. To the best of my knowledge, all studies on liquid flow using OCT technique were conducted under ambient conditions. This limits the system's ability to study dynamic processes, such as the effect of changing temperature, on the liquid flow in porous media.

In this chapter, a porous tobacco layer is used as a model to study the dynamic of liquid flow in thin porous material. Porous tobacco layer comprised of fibrous structure made

of cellulose with fiber diameter of around 30-50 μm and average inter-fiber pore diameter of ~5 μm with a thickness of ~200 μm [19]. Additionally, the materials are abundant and inexpensive. Dynamics of liquid flow at an elevated temperature in porous tobacco layer can serve as an inspiration to many natural and engineering phenomena.

Besides being a model for this study, porous tobacco layer has an actual application which involves interaction with liquid and heat: heated tobacco products. A new concept of heated tobacco products (HTP)—inspired by the evaporation of nicotine in tobacco leaves at temperatures below 300°C (far below the combustion temperature of conventional cigarettes)—has attracted attention in recent years [20, 21]. Viscous liquid such as glycerol is used as humectants and as the main aerosol former, i.e. without the presence of glycerol, the gas-vapor mixtures cannot condense as inhalable aerosol droplets [22, 23]. A detailed study on the transport of glycerol in tobacco sheets during heating is yet to be conducted [19]. This knowledge is needed to understand the control of aerosol formation from heated tobacco products so that the system (i.e., heated tobacco device) can be designed to have little impact on indoor air quality. However, it should be noted that lower indoor emissions of HTP compared to conventional cigarettes may not necessarily correlate to lower health risks [21].

This chapter aims to demonstrate, for the first time, the use of optical coherence tomography (OCT), integrated with a specially designed heating chamber and an air pump, to monitor the behavior of viscous liquids (e.g., glycerol) in a porous tobacco-based layer during heating. The OCT method is flexible, can be integrated with other systems, and can provide tomographic images of samples under atmospheric pressure.

3.2 Materials and methods

The setup for real-time observation of liquid transport in porous biomass under heating is shown in Figure 3.1. It consists of a spectral-domain optical coherence tomography (SD-OCT) system coupled with a specially-designed heating chamber connected to an air pump's suction line. The light source in the OCT system is a near-infrared superluminescent diode (SLD) with a wavelength of 1470 nm and a bandwidth of 44 nm. The depth resolution of the OCT tomogram is 22 μm. The tomogram was obtained by scanning the beam focused on the sample's surface with a galvanometer mirror. The horizontal scanning range was 500 μm with a spot size (diameter of a focused beam of light on the sample surface) of 5 μm. The OCT system scanned the sample in 10 seconds, from start to finish, for each run.

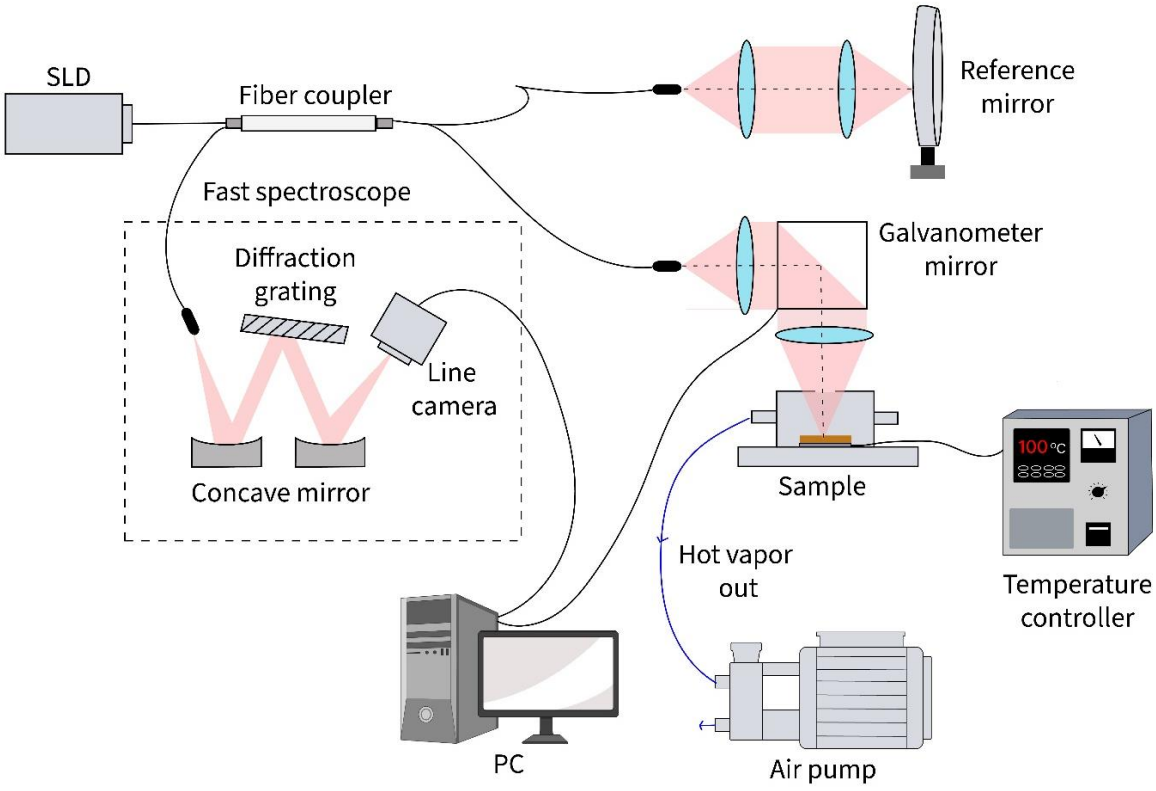

Figure 3. 1 A spectral-domain optical coherence tomography (SD-OCT) system coupled with a heating chamber (with a biomass sample) and an air pump. SLD is a near-infrared superluminescent diode

A reconstituted tobacco sheet [JT, Japan] was used because the reconstitution process yielded a chemically homogenous sample. The tobacco substrate—a densely connected fiber with a heterogeneous inter-fiber pore size of several micrometers—218 ±3 5 µm thick and 2.5 x 2.5 cm large. It was fixed on top of the ceramic heater [Sakaguchi E.H Voc Corp., Japan with heat-resistant tape. The heating temperature was controlled by a desktop-type temperature control unit [Shimaden Co., Ltd., Japan] and was set to heat to 100, 120, and 200°C. The ceramic heater and the sample were mounted inside the heating chamber, which was then placed under the objective lens of the OCT system, as illustrated in Figure 3.1. The temperature profiles of the top and bottom surfaces of the tobacco substrates during the experiment were measured using a T-type ultrafine (φ = 0.127 mm) thermocouple [As One Corp., Japan] and recorded in a data logger [Graphtec Corp., Japan].

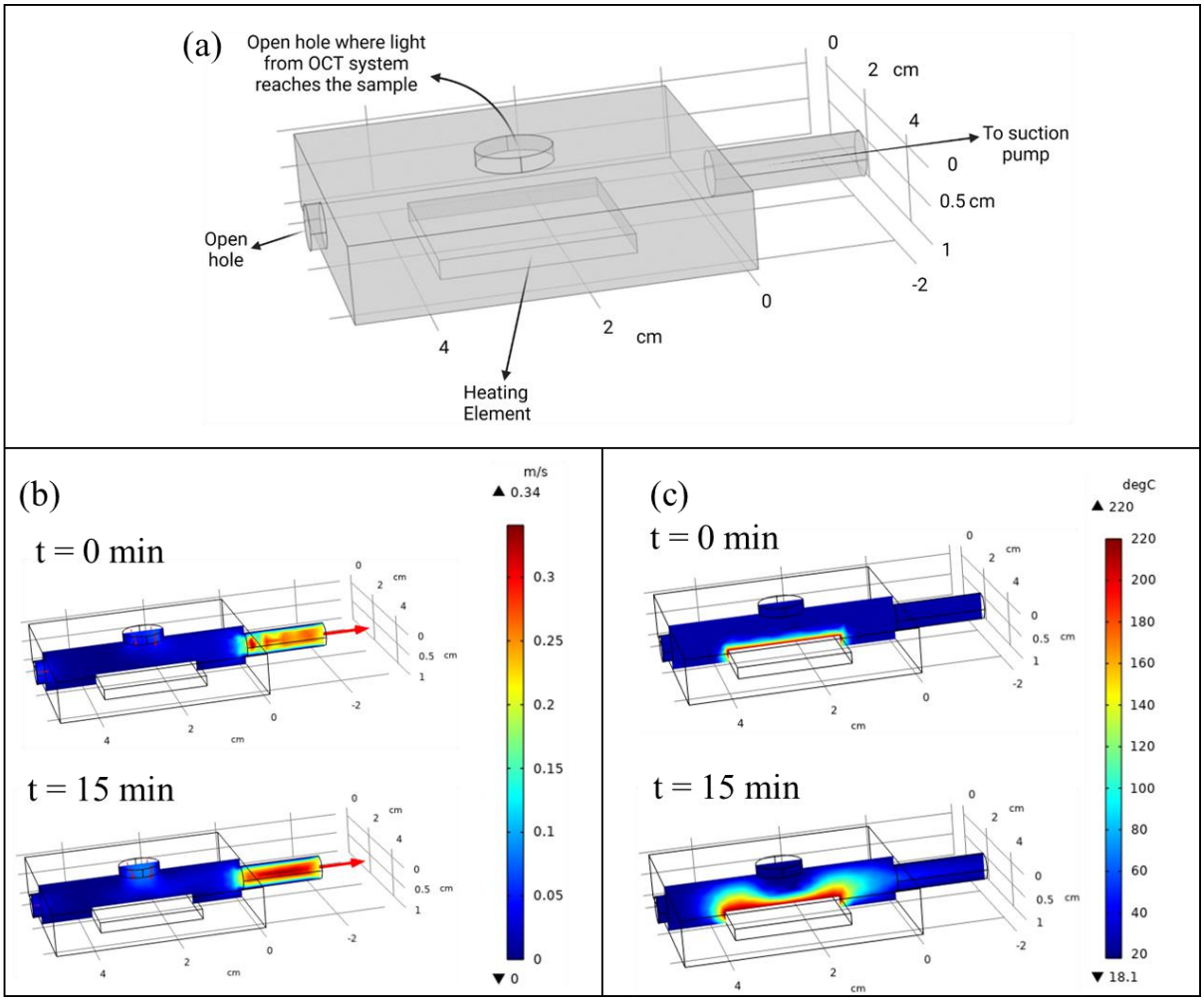

Figure 3.2 (a) Geometry of the heating chamber, for heater temperature set at 200°C and suction velocity of 0.2 m/s; (b) calculated velocity profile inside the chamber and (c) calculated temperature profile in the chamber after/before operating the suction-pump

The time-dependent temperature and airflow profile in the chamber during the experiment were simulated using a heat/fluid dynamics analysis software (COMSOL Multiphysics®). Figure 3.2 (a) shows the chamber's geometry and dimensions. For the numerical simulation, the heating element was set at 200°C. The hot vapour inside the chamber was pumped at 0.2 m/s from the right side of the chamber. One side of the chamber and the hole at the top of the chamber were set as open boundaries. The simulation proved that even at temperatures as high as 200°C, suction flow as low as 0.2 m/s prevented the runaway hot vapour from flowing upward toward the objective lens. [Figure 3.2(b),(c)] In this experiment, the suction flow rate, set at 6 l/min, caused no condensation on the glass plate temporally placed above the upper hole of the chamber. This setup was essential to prevent hot vapour flow to the optical lens, which could affect the results and damage the lens.

At the beginning of each observation, the dry sample was scanned before dropping 20 µl of glycerol (99.5% purity and 290°C boiling point at 1 atm). [Wako Pure Chemicals Industries Ltd., Japan] Heating started simultaneously with the dropping of glycerol on the sample; the observation was completed in 15 minutes.

The output from the OCT analysis system is backscattered light intensity ($I_{(z)}$) as a function of depth (z) and horizontal scanning length/transverse length. The raw data from the OCT system was processed in MATLAB® to construct the matrix for producing the tomographic image and to calculate the attenuation coefficient (μ_t) based on Lambert-Beer's law [99].

$$I_{(z)} = I_0 \exp[-2\,(\mu_s' + \mu_a)\,z] \tag{3.1}$$

$$-\frac{1}{2}\frac{d}{dz} log \frac{I_{(z)}}{I_0} = \mu_s' + \mu_a = \mu_t \tag{3.2}$$

I_0 is the incident light intensity, z is the optical path length, μ_a is the absorption coefficient, and μ_s' is the equivalent scattering coefficient. The constructed matrix for the tomographic image was then plotted in OriginPro (OriginLab) to produce the final contour of the tomogram.

Duncan's Multiple Range Test was conducted to estimate the transitional points for the transport (penetration and evaporation) of glycerol in porous biomass using the International Business Machines Corporation's Statistical Package for the Social Sciences (IBM SPSS) software. A thin film of platinum particles were coated using the sputtering process (Smart Coater, JEOL Ltd., Japan) and observed the morphology before and after heating with a scanning electron microscope (SEM JSM 6510, JEOL Ltd., Japan).

3.3 Results and discussion

Barontini et al. [25, 26] noted that coupling Thermogravimetric Analysis (TGA) and Fourier Transform Infrared Spectroscopy (FTIR) gas analysis of tobacco at low heating rates resulted in four regions of weight loss. Region I (30-120°C) indicates moisture release; regions II (120–250°C) and III (250–370°C) indicate two stages—thermal decomposition and evaporation; and region IV (370-550°C) indicates further thermal decomposition and combustion. In this study, the heating temperature was set at 100, 120, and 200°C to study in detail the phenomena in regions I and II of previous studies [25, 26].

Figure 3.3 (a-c) shows the temperature at the top and bottom surfaces of the tobacco substrates at each temperature set point with suction from the air pump. There was a

significant difference between the bottom (direct contact with the heater) and the top (solid-air interface) surface temperatures of the tobacco substrates. The lower temperature at the top was due to forced convection at the solid-air interface activated by air-pump suction. The evaporation of compounds such as water, glycerol, and nicotine require energy, resulting in the cooling of the substrate [22]. Additionally, the Knudsen effect and phonon (heat carrier in solid) scattering at the solid-gas interphase within the pores of the sample's structure decreased the effective thermal conductivity of the sample [27], resulting in a lower temperature at the surface away from the heat source.

When glycerol was first dropped on the tobacco substrates surface, glycerol did not spontaneously wet and spread on the surface. The glycerol formed a sessile droplet with a diameter of ~3 mm (see Figure A2.1). A contact angle at the glycerol, substrate, and air interface was observed. The surface tension of glycerol was high, and the effect of viscous resistance was dominant at about 25°C (μ = ~812 cP). At this stage, gravity counteracted viscous resistance because of the high mass per unit area of the glycerol.

As heating progresses, the contact angle disappears gradually. The time needed for the contact angle to disappear based on video observation is ~35 s for 100ºC heating and ~25 s for 120 and 200ºC heating. This time corresponds to tobacco surface temperature of 74.8, 85.2, and 95.5ºC (Figure 3.3 (a-c)), and by assuming that the glycerol temperature equals to surface temperature, the glycerol viscosity is ~36, ~23, and ~16 cP for 100, 120, and 200ºC respectively. The decrease in the viscosity of glycerol due to the increase in temperature, as fitted from the glycerol viscosity data at various temperatures provided by [28], can be seen in Figure 3.3(d). Significant reduction in viscous flow resistance due to heating promotes glycerol spreading (movement of liquid in the x-axis direction) and penetration (movement of liquid in the y-axis direction), predominantly due to capillary forces.

Observation by the camera also revealed the time needed by liquid glycerol to spread to a maximum surface area. For heating temperatures of 100, 120, and 200ºC, it took 240, 155, and 90 s, respectively, for glycerol to spread in-plane before a further change in surface area due to liquid spreading was undetected by the camera (see figure A2.2). The OCT system characterizes the change in the trans-planar (depth direction) of the substrate due to liquid flow. Because the scanning area of OCT is much smaller than the initial diameter of the glycerol on the surface of the sample, we expect that the variation in liquid distribution due to liquid spreading on the sample will not strongly influence the cross-sectional OCT

scanning result. However, variations in scattered light from the sample may be observed by OCT when the point of observation is too far off the initial point of spreading.

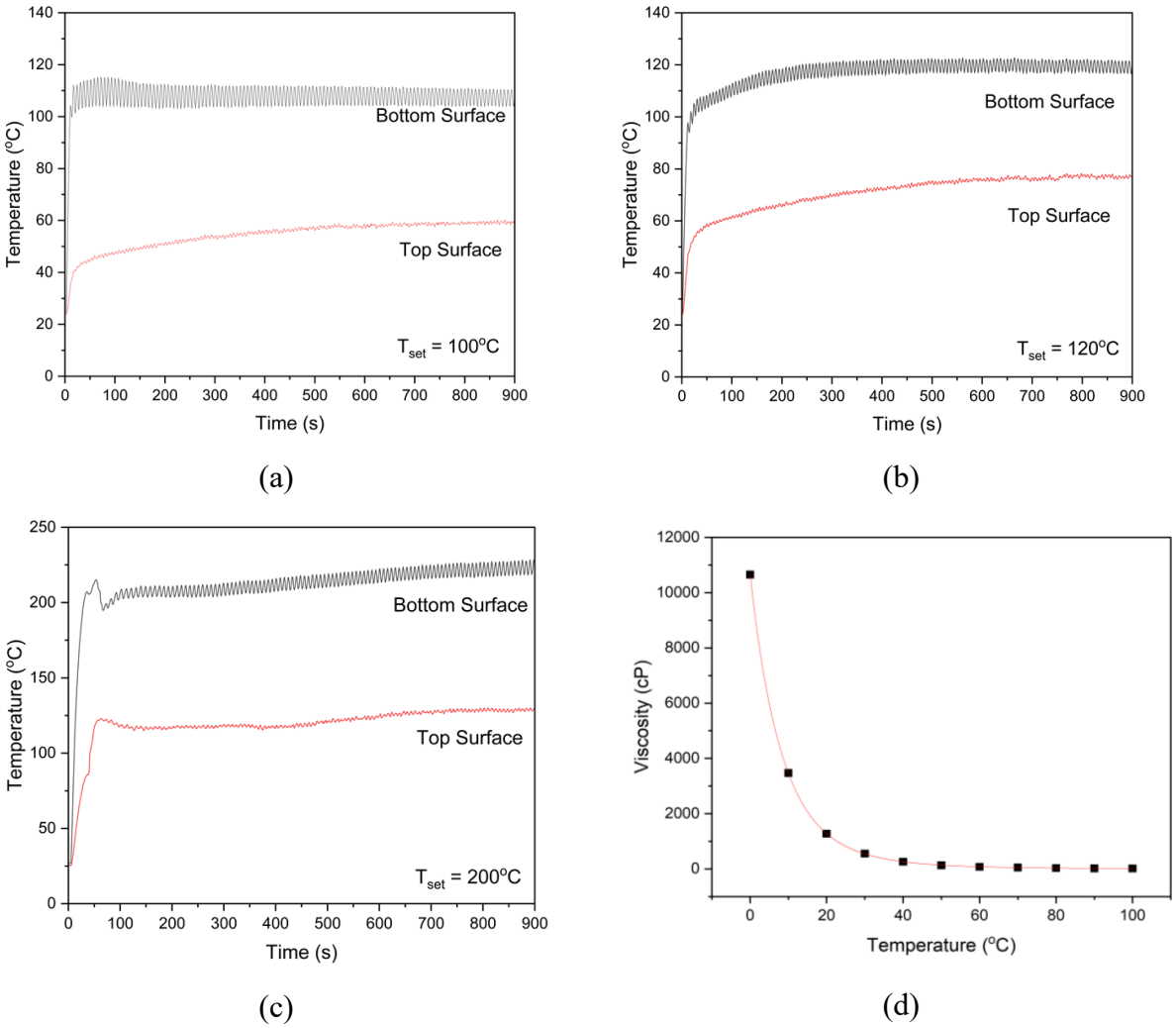

Figure 3.3 The temperature profile of the upper part of samples during heating; (a) 100°C, (b) 120°C, (c) 200°C, and (d) temperature dependence of glycerol viscosity (data fitted for Glycerol 99.5% w/w from Segur & Oberstar [28])

Figure 3.4 shows four OCT tomograms of the porous tobacco substrates during the experiment. OCT tomograms help visualize the liquid flow in the media by capturing the cross-section image of the sample at each point in time. It is important to understand that the sample, a porous tobacco substrate, was produced by the papermaking process and is primarily composed of cellulose from tobacco stems and leaf scraps [29, 30]. On average, the cellulose content of a large tobacco leaf stalk is 31–34%, while the tobacco leaf itself contains 16–17% cellulose [100]. Therefore, we assumed that cellulose was the major

component of the sample. The refractive index (n) of cellulose is around 1.4613 (at λ = 1052 nm) [32].

At initial conditions, all tomograms show a bright (whitish) image on the surface of the sample due to air distribution inside the cellulose matrix of the tobacco substrates. Light scattering occurred when light traveled from the air (n = 1) to the tobacco substrates; the difference in the refractive indices of the two media caused intense scattering creating a bright tomogram.

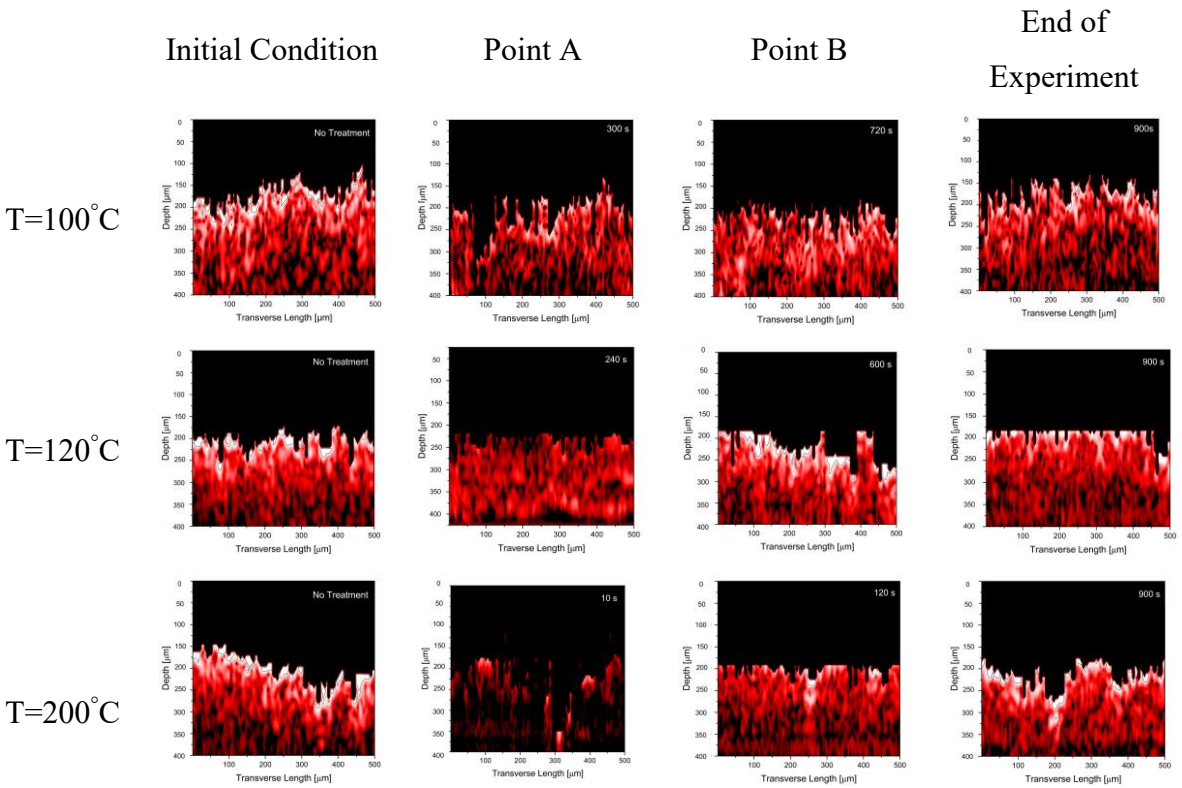

Figure 3.4 OCT tomograms of cross-sections of samples before, during, and after heating at different temperatures

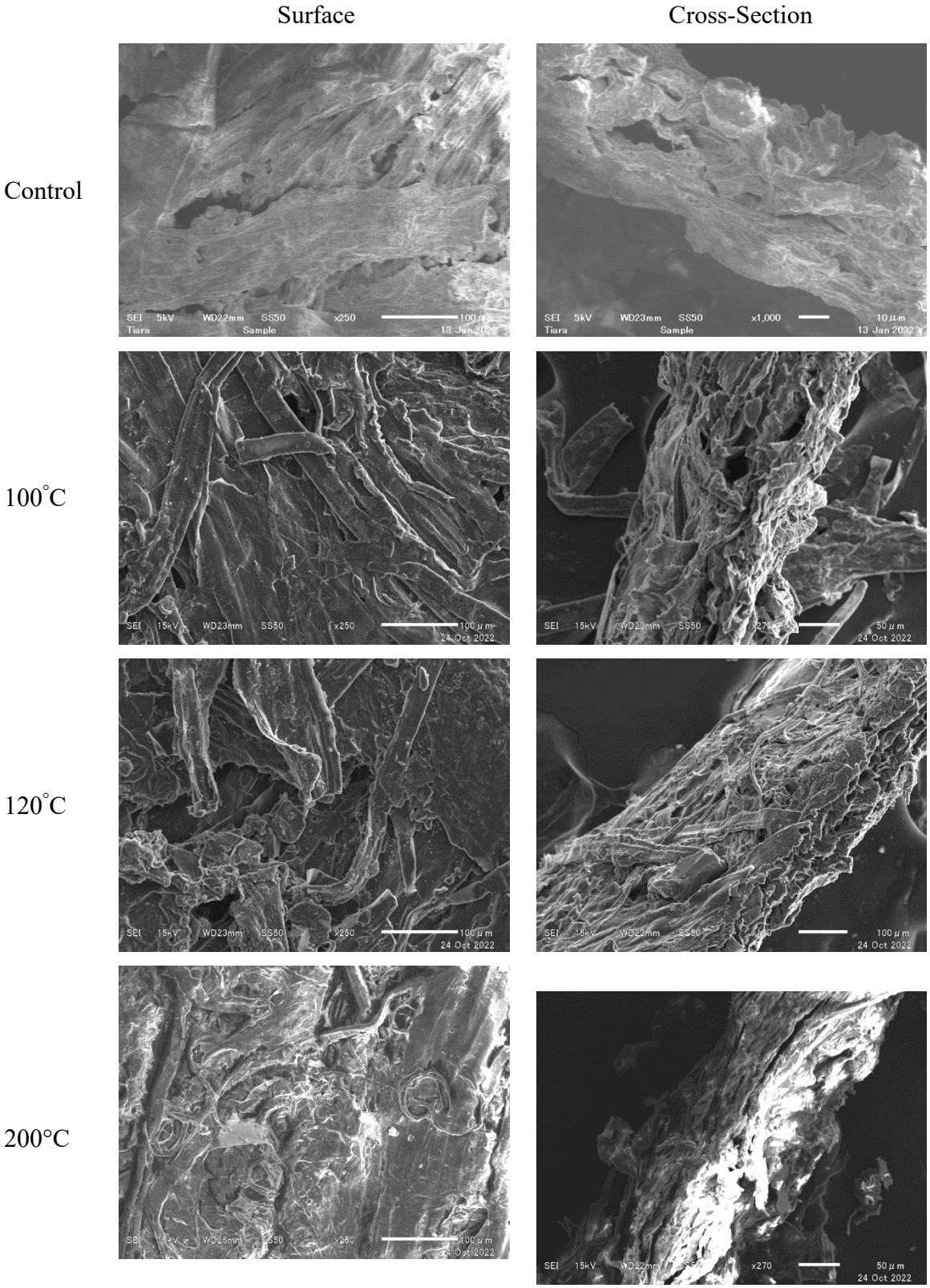

Figure 3. 5 SEM images of the surface and cross-section of samples: before (Control) and after heating at various temperatures

The brightness of the tomogram reduces with time until approximately point A where the glycerol penetration is around its peak. At this point, the majority of the air inside the cellulose matrix had been displaced by the glycerol which had spread and penetrated due to capillary forces. The refractive index of glycerol is very close to the refractive index of cellulose in the near-infrared region—1.4631 (at λ = 1050 nm) [33]. The closeness of the refractive indices of glycerol and cellulose caused refractive index matching. As a result, the light was transmitted more effectively and deeper into the sample instead of being scattered on the surface. This resulted in lower backscattered light intensity [34-36]. Additionally, the glycerol absorbed some of the incident light, decreasing the intensity of the backscattered light further. The absorption coefficient of glycerol at 1470 nm wavelength is 10.113 cm^{-1} [37]. Makino et al. [14] used SD-OCT with two NIR wavelengths to see the evaporation process of water from the porous tobacco substrate under ambient conditions. They noted that the presence of water in the pores of the medium darkens the appearance of the tomographic image due to refractive index matching. Their finding supported the observation made in this chapter.

It was also observed that the higher heating temperature in point A produced a darker tomogram, probably because the surface tension of glycerol dropped significantly, helping to wet tobacco substrates and displace air "completely" in the cellulose matrix. Hence, the effect of refractive index matching became more pronounced and backscattering intensity decreased significantly [34].

After point A, evaporation became more dominant than liquid penetration. Capillary action distributed the liquid glycerol over a wide surface area, increasing the contact between the glycerol and air. This condition, coupled with the heating, allowed the majority of the glycerol to evaporate out of the sample far below its boiling point. Further heating evaporated more glycerol allowing air to re-enter the cellulose matrix. The presence of air in the cellulose matrix increased the backscattering intensity and terminated the effect of refractive index matching. This produced a brighter tomogram, as shown in point B and "end of experiment" tomograms.

Liquid penetration and evaporation from the biomass substrates caused changes in the sample's morphology as seen, to an extent, in the appearance of the time-lapsed tomogram at each temperature. The "unnatural" straight cuts on the surface of samples at 120°C (e.g., first image from right) and 200°C (e.g., second image from right) are attributed to the swelling of cellulose fibers when the glycerol penetrated the sample [7, 34], and/ or coiling of the

samples when the glycerol evaporated. These morphological changes caused the sample to rise beyond the field of view of the OCT lens, resulting in “unnatural” tomograms.

SEM was also used to observe the change in the microstructure of the sample. [Figure 3.5] The SEM images suggest that the penetrating and evaporating glycerol shrunk some pores of tobacco substrates and “destroyed” some of the cellulose fiber networks. This effect became stronger at higher temperatures. At the end of the heating experiment at 200°C, the tobacco substrates turned dark brown (Figure A2.2).

The movement of glycerol inside the tobacco substrates is quantified by calculating the attenuation coefficient using the scattered intensity data from the OCT system according to equation 2. The attenuation coefficient characterizes the strength of backscattering from the sample and is widely used to differentiate “healthy” and “non-healthy” tissues in clinical analysis [38-40]. A high attenuation coefficient represents high backscattering intensity while a low attenuation coefficient represents the contrary. In previous research [14], the movement of liquid water in porous tobacco substrates under ambient condition has been successfully quantified by the attenuation coefficient.

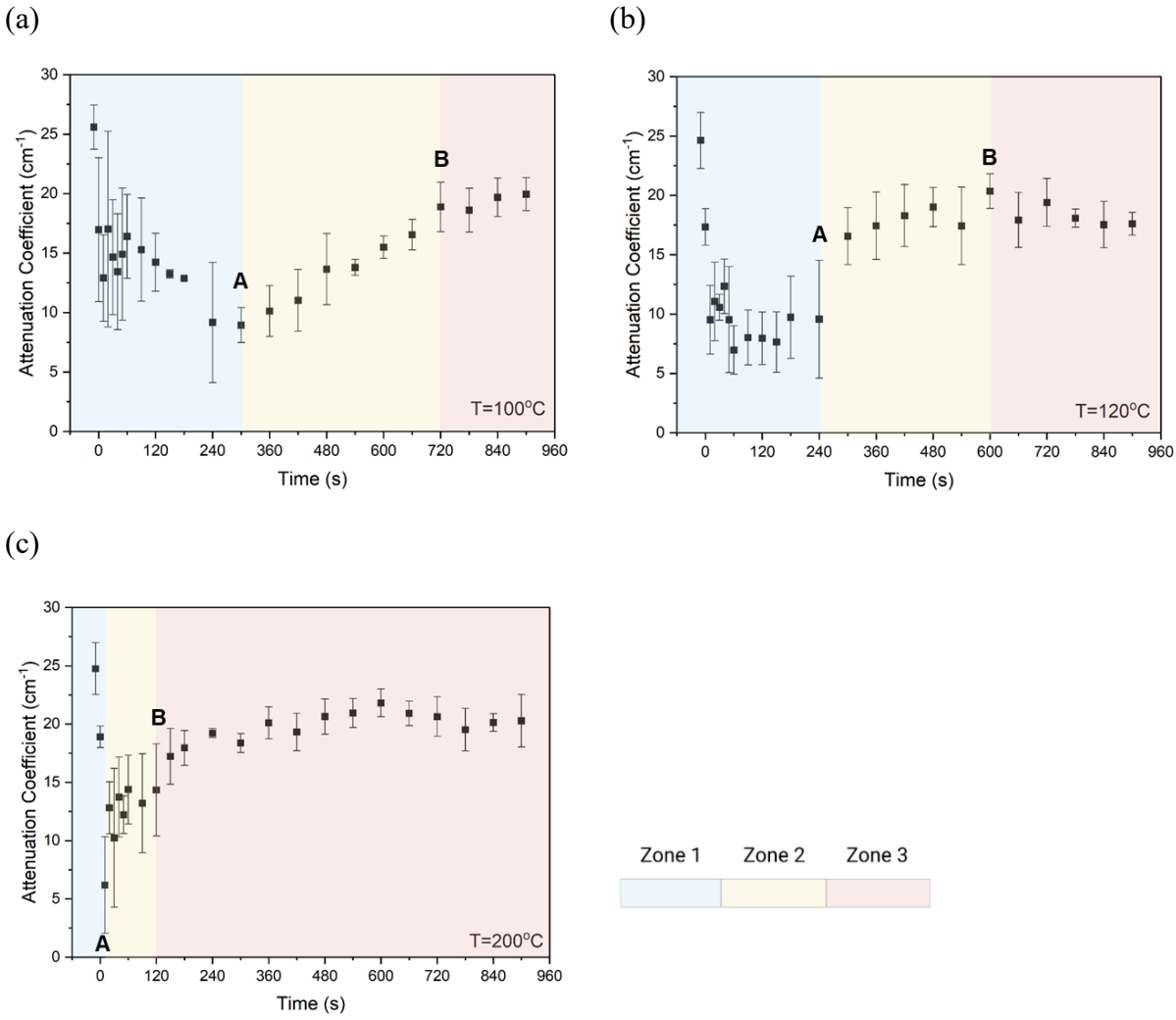

Figure 3. 6 Temporal change in attenuation coefficient of tobacco substrates after dropping glycerol at; (a) 100˚C, (b) 120˚C, and (c) 200˚C. Values are mean ± standard deviation (SD) of three independent experiments

The attenuation coefficient plotted against elapsed time for each temperature is shown in Figure 3.6 (a-c). Point A and B for each temperature were estimated using Duncan's test. The attenuation coefficient data (n = 3) at several time intervals of each heating temperature was used as the input. Duncan's test assigned each point in the data set to one or more groups. The data that were significantly different from each other ($p < 0.05$) were assigned to different groups. Similar data shared the same group.

Point A is a time approximation where maximum penetration occurs before further heat transfer in an evaporation-dominant zone. Point A is the latest time in which the obtained attenuation coefficient is significantly different from the attenuation coefficient of the

tobacco substrates at the initial condition (untreated sample). In Duncan's test result, critical point A belongs to the group farthest from the group where the attenuation coefficient of the untreated sample belonged.

Point B is a time approximation where liquid evaporation starts to slow down because most of the free liquid has evaporated. Point B is the earliest time in which the obtained attenuation coefficient becomes non-significantly different from the attenuation coefficient of the tobacco substrates at the initial condition (untreated sample). In Duncan's test result, critical point B belongs to the same group as the untreated sample.

It should be noted that point A and B are just approximation based on the significant difference relative to the initial condition that we propose in this first study. Variations in the timing of points A and B may occur. Additional study to address this issue is needed.

The two points divide the attenuation data into 3 different zones, namely zone 1, 2, and 3. Zone 1 (blue) is the penetration-dominant zone and begins immediately when heating starts after dropping the glycerol. Liquid penetration reaches a maximum at around point A, which occurs at ~300, ~240, and ~10 seconds for temperatures 100, 120, and 200°C, respectively. Heat transfer in this region is mainly sensible heat transfer and the energy gained by the sample increases the temperature of the sample and the glycerol within it. The temperature increase decreases the glycerol's viscous resistance making penetration due to capillary force dominant. Interestingly, there were little variations in the temperature difference between the top/upper and bottom surface (ΔT) of all samples during point A; average ΔT at point A = 53.1 ± 3.8°C.

Fabritius and Myllyla [13] tracked the sorption of glycerol in a paper medium using OCT at ambient temperature. By observing the OCT tomogram, they found that there is a 6.1 s delay before the capillary penetration begins. They noted that glycerol takes 10.3 s to penetrate from the front side to the backside of 420 μm paper. There is a deviation between the result of the observation in their study and the Washburn equation for the capillary flow of liquids in the porous medium due to the non-uniform pore size distribution of their medium. Additionally, the effect of substrate (multi-layered biomass) temperature on the penetration of glycerol was investigated previously by Asanuma et al. [19] by using colloidal fluorescence particles and fluorescence microscopy. They found that for the same 1-minute heating observation, glycerol droplet that is exposed to a higher temperature can penetrate deeper layers faster than the glycerol at a lower temperature. They also found that glycerol can spread more in the x-axis direction when the heating temperature is lower. Their

observation validated the finding in this chapter regarding the relationship between heating temperature and maximum penetration time. However, similar to the study by Fabritius et al. both studies identified the wetting front of the liquid but did not discuss the possibility that the pores behind the visible wetting front are not fully saturated. We expect that the gradual decrease of the attenuation coefficient before reaching to a maximum suggested a characterization of the state of intra-fiber pore-filling behind the wetting front.

Cellulose fiber in tobacco substrates are typically made of micrometre-sized inter-fiber pores and nanometre-sized intra-fiber pores [3]. Inter-fiber pores are pores constructed from entangling individual cellulose fibers, while intra-fiber pores are the internal cavities in individual cellulose fiber. Liquid can be absorbed in both the inter-fiber and the intra-fiber pores [7], but the inter-fiber pores are more permeable because they are larger [3]. Hence, glycerol penetrates under capillary pressure into the inter-fiber pores and diffuses into the intra-fiber pores due to the concentration gradient. A detailed discussion on this phenomenon can be found in [7].

Energy accumulation in the sample after point A promotes glycerol evaporation due to latent heat transfer. Zones 2 (yellow; between A and B) and 3 (light red; after B) are evaporation-dominant zones. Zone 2 begins approximately after point A and ends at around point B; ~720, ~600, and ~120 seconds for temperatures 100, 120, and 200°C, respectively. Evaporation in zone 2 is considered the evaporation of free liquid in the sample matrix. Free liquid in this case is the glycerol which remained on the upper surface of the sample and in the inter-fiber pores.

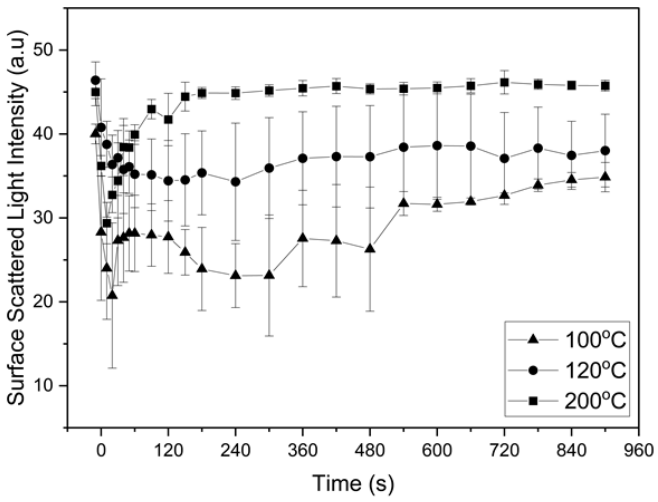

Figure 3. 7 Scattered light intensity from the surface of the sample at various temperatures. Values are mean ± standard deviation (SD) of three independent experiments

After point B, there are slow and subtle changes in the attenuation coefficient. The drying rate is expected to decrease from point B because the liquid movement to the exposed surface is unable to replenish the liquid at the surface. At this point, most of the free liquid has evaporated and the “bound” liquid combined with the “trapped” liquid begins to evaporate. “Trapped” liquid is defined as a liquid that is not “bound” to the fibers but is difficult to transport to the exposed surface. Liquid trapped in nanoscale pores is considered a non-freezing bound liquid [41].

To reduce the effect of structural change in our data interpretation, an analysis of light interaction with the surface of the sample is included. The upper sample surface is chosen because it is the first point of contact for the incident light before volumetric structural change further modifies the interaction between light and the sample. Additionally, the upper surface of the sample is assumed to be the main transport direction for the evaporating liquid, meaning if the surface is dry before the experiment is completed, it is reasonable to assume that there is no evaporation mass flux from below the surface and evaporation has terminated. To understand this phenomenon better, we plotted the backscattering intensity from the sample surface against the elapsed time at each temperature [Figure 3.7].

In Figure 3.7, the sample is considered dry only at 200°C after point B because the backscattered light intensity from the sample’s surface after the point B was almost the same as that of the “dry” (initial) sample, and there was no notable change until the end of the heating experiment. In addition, the attenuation coefficient is stable after point B even though it does not return to the “original" attenuation coefficient value of the dry sample.

At 100 and 120°C, both the attenuation coefficient and backscattered light intensity from the surface value did not return to the sample's initial value. This indicates that the samples may not have been completely dried. The changes in attenuation coefficient after point B indicate slow evaporation of trapped liquid and bound liquid from the sample. The bound liquid is defined as the initial water [41] present in the sample, plus the glycerol bound to the hydrophilic surfaces of cellulose fiber by hydrogen bonds.

The phenomenon at the boundary between the sample’s upper surface and the surrounding air is influenced by conduction from the heater to the sample and forced convection due to the air pump's suction flow. In some applications, such as food dehydration, convective drying results in low-porosity and high-density materials, which are undesired for some purposes [42]. For further studies, the dimensionless approach, for example, the Nusselt number (*Nu*), gives our research another advantage. For instance, $Nu > 1$ indicates that

convective heat transfer influences the system more than conductive heat transfer. By increasing laminar flow in the chamber, convective heat transfer can be minimized.

The results of this chapter could have implications for other porous materials, such as paper and fabrics, where capillary forces play a role in the penetration and spreading of liquids. The integration of a heating system and the use of attenuation coefficients calculated from OCT results to characterize liquid penetration and evaporation is expected to shed light on a better understanding of dynamic liquid flow in a medium with a non-uniform pore size whose behavior deviates from the Washburn equation.

In the future, it is expected that a heating system such as the one proposed in the present study, can be integrated with functional extensions of OCT such as phase-sensitive/ polarization-sensitive and Doppler OCT for a more thorough understanding on the dynamics of temperature-dependent liquid flow phenomena in hundreds of micrometre-thick porous materials. Polarization-sensitive (PS) OCT provides not just imaging based on tissue reflectivity but also enables the mapping of sample polarization properties with depth resolution [43]. By analysing the changes in polarization as the light passes through the porous material, polarization-sensitive OCT can distinguish between areas with and without the liquid. Doppler OCT on the other hand, allows the quantification of velocity as well as the direction of flow within a tissue by applying Doppler principle, in addition to structural imaging [44]. By measuring the Doppler frequency shift, one can try to quantify the temperature-dependent velocity of liquid imbibition in porous materials. Additionally, on a more recent developments, the speckle patterns (i.e random pattern of bright and dark spots that appear when coherent light interacts with a rough or scattering surface) from OCT [45] can be further analysed to characterize liquid-filled porous materials.

3.4 Conclusion

Optical coherence tomography (OCT) system coupled with a heating chamber connected to an air pump suction line has allowed an unprecedented, non-destructive, and real-time observation of the penetration and evaporation of viscous liquid in porous biomass during heating. The movement of liquid in a porous tobacco substrates can be observed through the OCT tomogram at several time lapses and can be quantified by the attenuation coefficient of the sample at a given temperature and time. By testing the time-lapse attenuation coefficient data using a statistical procedure (Duncan's multiple range test), we were able to approximate the transitional points in penetration and evaporation at each temperature. The proposed analytical system is an attractive alternative for tracking liquid

transport in porous biomass when contact heating is applied, and is also useful for understanding inward and outward mass transfer.

3.5 References

[1] A.W. Martinez, S.T. Phillips, G.M. Whitesides, E. Carrilho, Diagnostics for the developing world: Microfluidic paper-based analytical devices, Anal. Chem. 82 (2010) 3–10. https://doi.org/10.1021/ac9013989.

[2] B. Malhotra, A. Keshwani, H. Kharkwal, Antimicrobial food packaging: Potential and pitfalls, Front. Microbiol. 6 (2015) 1–9. https://doi.org/10.3389/fmicb.2015.00611.

[3] M.G. Wijburg, S. Wang, A.A. Darhuber, Transport and evaporation of aqueous co-solvent solutions in thin porous media, Colloids Surfaces A Physicochem. Eng. Asp. 656 (2023) 130268. https://doi.org/10.1016/j.colsurfa.2022.130268.

[4] W. Yang, J. Xu, Drop spreading and penetrating on micro/nano particle sintering porous with multiscale structure, Colloids Surfaces A Physicochem. Eng. Asp. 516 (2017) 9–22. https://doi.org/10.1016/j.colsurfa.2016.12.005.

[5] A. Clarke, T.D. Blake, K. Carruthers, A. Woodward, Spreading and Imbibition of Liquid Droplets on Porous Surfaces, Langmuir. 18 (2002) 2980–2984.

[6] Y. Huang, Q. Chen, R. Wang, Visualization study on capillary-spreading behavior of liquid droplet in vertically aligned carbon nanotube array, Int. J. Heat Mass Transf. 120 (2018) 1055–1064. https://doi.org/10.1016/j.ijheatmasstransfer.2017.12.122.

[7] S. Chang, W. Kim, Dynamics of water imbibition through paper with swelling, J. Fluid Mech. (2020). https://doi.org/10.1017/jfm.2020.219.

[8] G. Zhang, R. Parwani, C.A. Stone, A.H. Barber, L. Botto, X-ray Imaging of Transplanar Liquid Transport Mechanisms in Single Layer Textiles, Langmuir. 33 (2017) 12072–12079. https://doi.org/10.1021/acs.langmuir.7b02982.

[9] T. Munuhe, A. Lebrun, L. Zhu, R. Ma, Using micro-ct to investigate nanofluid droplet sorption in dry powder beds, Powder Technol. 305 (2017) 232–240. https://doi.org/10.1016/j.powtec.2016.09.079.

[10] M. Bencsik, H. Adriaensen, S.A. Brewer, G. McHale, Quantitative NMR monitoring of liquid ingress into repellent heterogeneous layered fabrics, J. Magn. Reson. 193 (2008) 32–36. https://doi.org/10.1016/j.jmr.2008.04.003.

[11] T. Karppinen, I. Kassamakov, J. Aaltonen, H. Pajari, E. Hæggstrom, Measuring liquid penetration in the thickness direction of paper, Eur. Phys. J. Appl. Phys. 32 (2005) 65–

71. https://doi.org/10.1051/epjap.

[12] Q. Zhang, N.K. Karadimitriou, S.M. Hassanizadeh, P.J. Kleingeld, A. Imhof, Study of colloids transport during two-phase flow using a novel polydimethylsiloxane micro-model, J. Colloid Interface Sci. 401 (2013) 141–147. https://doi.org/10.1016/j.jcis.2013.02.041.

[13] T. Fabritius, R. Myllylä, Liquid sorption investigation of porous media by optical coherence tomography, J. Phys. D. Appl. Phys. 39 (2006) 4668–4672. https://doi.org/10.1088/0022-3727/39/21/025.

[14] T. Makino, H. Ujino, I.W. Lenggoro, T. Iwai, Imaging and quantitative analysis of water evaporation process using spectral-domain optical coherence tomography under illumination with two near-infrared wavelengths, Opt. Rev. 30 (2023) 158–165. https://doi.org/10.1007/s10043-023-00792-1.

[15] H. Huang, Y. Huang, W. Lau, H.D. Ou-Yang, C. Zhou, M.S. El-Aasser, Integrating optical coherence tomography with gravimetric and video analysis (OCT-Gravimetry-Video method) for studying the drying process of polystyrene latex system, Sci. Rep. 8 (2018) 1–13. https://doi.org/10.1038/s41598-018-30914-8.

[16] E.J.G. Sewalt, J. Kalkman, J.R. van Ommen, G.M.H. Meesters, V. van Steijn, Revealing how maltodextrin-containing droplets dry using optical coherence tomography, Food Res. Int. 157 (2022) 111049. https://doi.org/10.1016/j.foodres.2022.111049.

[17] A. du Plessis, C. Broeckhoven, A. Guelpa, S.G. le Roux, Laboratory x-ray micro-computed tomography: A user guideline for biological samples, Gigascience. 6 (2017) 1–11. https://doi.org/10.1093/gigascience/gix027.

[18] D.P. Popescu, L.P. in. Choo-Smith, C. Flueraru, Y. Mao, S. Chang, J. Disano, S. Sherif, M.G. Sowa, Optical coherence tomography: Fundamental principles, instrumental designs and biomedical applications, Biophys. Rev. 3 (2011) 155–169. https://doi.org/10.1007/s12551-011-0054-7.

[19] Y. Asanuma, T.N. Pratiwi, M. Wada, T. Iwai, I.W. Lenggoro, Liquid Transport of Heated Glycerol-Water Mixtures with Colloidal Fluorescent Particles through Multiple Biomass Layers, E-Journal Surf. Sci. Nanotechnol. 20 (2022) 13–19. https://doi.org/10.1380/ejssnt.2022-008.

[20] V. Cozzani, F. Barontini, T. McGrath, B. Mahler, M. Nordlund, M. Smith, J.P. Schaller, G. Zuber, An experimental investigation into the operation of an electrically heated tobacco system, Thermochim. Acta. 684 (2020) 178475.

https://doi.org/10.1016/j.tca.2019.178475.

[21] M. Jankowski, G.M. Brożek, J. Lawson, S. Skoczyński, P. Majek, J.E. Zejda, New ideas, old problems? Heated tobacco products – A systematic review, Int. J. Occup. Med. Environ. Health. 32 (2019) 595–634. https://doi.org/10.13075/ijomeh.1896.01433.

[22] M. Nordlund, A.K. Kuczaj, Modeling Aerosol Formation in an Electrically Heated Tobacco Product, 10 (2016) 307–319.

[23] Y. Tong, Y. Xiong, Q. Yan, S. Gao, X. Le, P. Wei, H. Shu, Z. Wang, X. Tang, P. Li, Z. Xiong, Y. Wang, Effects of glycerol and propylene glycol on smoke release of heat-not-burn tobacco products, IOP Conf. Ser. Earth Environ. Sci. 1802 (2021). https://doi.org/10.1088/1742-6596/1802/2/022025.

[24] T. Tsugita, T. Iwai, Optical coherence tomography using images of hair structure and dyes penetrating into the hair, Ski. Res. Technol. 20 (2014) 389–398. https://doi.org/10.1111/srt.12129.

[25] F. Barontini, M. Rocchi, A. Tugnoli, V. Cozzani, J. Tetteh, M. Jarriault, I. Zinovik, Quantitative analysis of evolved gas in the thermal decomposition of a tobacco substrate, Chem. Eng. Trans. 32 (2013) 703–708. https://doi.org/10.3303/CET1332118.

[26] F. Barontini, A. Tugnoli, V. Cozzani, J. Tetteh, M. Jarriault, I. Zinovik, Volatile products formed in the thermal decomposition of a tobacco substrate, Ind. Eng. Chem. Res. 52 (2013) 14984–14997. https://doi.org/10.1021/ie401826u.

[27] V. Apostolopoulou-Kalkavoura, P. Munier, L. Bergström, Thermally Insulating Nanocellulose-Based Materials, Adv. Mater. 33 (2021). https://doi.org/10.1002/adma.202001839.

[28] J.B. Segur and H. E. Oberstar, Viscosity of Glycerol and Its Aqueous Solutions, Ind. Eng. Chem. 43 (1951) 2117-2120. http://dx.doi.org/10.1021/ie50501a040.

[29] H. Liu, Z. Liu, H. Liu, L. Hui, F. Zhang, P. Liu, X. An, Y. Wen, S. Wu, Using cationic nanofibrillated cellulose to increase the precipitated calcium carbonate retention and physical properties during reconstituted tobacco sheet preparation, Ind. Crops Prod. 130 (2019) 592–597. https://doi.org/10.1016/j.indcrop.2019.01.021.

[30] W. Gao, K. Chen, Physical properties and thermal behavior of reconstituted tobacco sheet with precipitated calcium carbonate added in the coating process, Cellulose. 24 (2017) 2581–2590. https://doi.org/10.1007/s10570-017-1270-5.

[31] G. Kulic, V. Radojicic, Analysis of cellulose content in stalks and leaves of large leaf tobacco, J. Agric. Sci. Belgrade. 56 (2011) 207–215.

https://doi.org/10.2298/jas1103207k.

[32] N. Sultanova, S. Kasarova, I. Nikolov, Dispersion properties of optical polymers, Acta Phys. Pol. A. 116 (2009) 585–587. https://doi.org/10.12693/APhysPolA.116.585.

[33] J. Rheims, J. Köser, T. Wriedt, Refractive-index measurements in the near-IR using an Abbe refractometer, Meas. Sci. Technol. 8 (1997) 601–605. https://doi.org/10.1088/0957-0233/8/6/003.

[34] T. Fabritius, R. Myllylä, Investigation of swelling behaviour in strongly scattering porous media using optical coherence tomography, J. Phys. D. Appl. Phys. 39 (2006) 2609–2612. https://doi.org/10.1088/0022-3727/39/12/021.

[35] M. Brezinski, K. Saunders, C. Jesser, X. Li, J. Fujimoto, Index matching to improve optical coherence tomography through blood, Circulation. 103 (2003) 1999–2003. https://doi.org/10.1161/01.cir.103.15.1999.

[36] J.M.S. Saarela, S.M. Heikkinen, T.E.J. Fabritius, A.T. Haapala, R.A. Myllylä, Refractive index matching improves optical object detection in paper, Meas. Sci. Technol. 19 (2008). https://doi.org/10.1088/0957-0233/19/5/055710.

[37] K. Wang, W. Wen, Y. Wang, K. Wang, J. He, J. Wang, P. Zhai, Y. Yang, P. Qiu, Order-of-magnitude multiphoton signal enhancement based on characterization of absorption spectra of immersion oils at the 1700-nm window, Opt. Express. 25 (2017) 5909. https://doi.org/10.1364/oe.25.005909.

[38] P. Gong, M. Almasian, G. van Soest, D.M. de Bruin, T.G. van Leeuwen, D.D. Sampson, D.J. Faber, Parametric imaging of attenuation by optical coherence tomography: review of models, methods, and clinical translation, J. Biomed. Opt. 25 (2020) 1. https://doi.org/10.1117/1.jbo.25.4.040901.

[39] G. Thepass, H.G. Lemij, K.A. Vermeer, Attenuation Coefficients from SD-OCT Data: Structural Information beyond Morphology on RNFL Integrity in Glaucoma, J. Glaucoma. 26 (2017) 1001–1009. https://doi.org/10.1097/IJG.0000000000000764.

[40] J. Lu, A.J. Deegan, Y. Cheng, T. Liu, Y. Zheng, S.P. Mandell, R.K. Wang, Application of OCT-Derived Attenuation Coefficient in Acute Burn-Damaged Skin, Lasers Surg. Med. 53 (2021) 1192–1200. https://doi.org/10.1002/lsm.23415.

[41] S. Park, R.A. Venditti, H. Jameel, J.J. Pawlak, Hard-to-remove water in cellulose fibers characterized by thermal analysis: A model for the drying of wood-based fibers, Tappi J. 6 (2007) 10–16. https://imisrise.tappi.org/TAPPI/Products/07/JUL/07JUL10.aspx.

[42] B.D.A. Porciuncula, L.A. Segura, J.B. Laurindo, Processes for controlling the structure

and texture of dehydrated banana, Dry. Technol. 34 (2016) 167–176. https://doi.org/10.1080/07373937.2015.1014911.

[43] B. Baumann, S. O. Baumann, T. Konegger, M. Pircher, E. Götzinger, F. Schlanitz, C. Schütze, H. Sattmann, M. Litschauer, U. Schmidt-Erfurth, C. K. Hitzenberger, Polarization sensitive optical coherence tomography of melanin provides intrinsic contrast based on depolarization, Biomed. Opt. Express. 3 (2012) 1670-1683. https://doi.org/10.1364/BOE.3.001670.

[44] Y. Li, J. Chen, Z. Chen, Advances in Doppler optical coherence tomography and angiography, Transl. Bio. 1 (2019) e201900005. https://doi.org/10.1002/tbio.201900005.

[45] V. B. Silva, D. A. D. Jesus, S. Klein, T. van Walsum, J. Cardoso, L. S. Brea, P. G. Vaz, Signal-carrying speckle in optical coherence tomography: a methodological review on biomedical applications, J. Biomed. Opt. 27 (2022) 030901. https://doi.org/10.1117/1.JBO.27.3.030901.

Chapter 4: Conclusion

The heat and flow phenomena in liquid-filled thin porous materials have been investigated both in an hydrophobic porous membrane and a hydrophilic, swellable porous material. A one step method to functionalize a porous material matrix through incorporation of particles based on simultaneous electrospinning and carbon-based particle production from candle burning is proposed for the first time. Additionally, a liquid flow visualization technique for porous materials under heating based on optical coherence tomography is also proposed for the first time. A combination of the tunable design and liquid flow visualization technique is expected to contribute to the advancement of the state-of-the-art knowledge towards fabrication of porous materials with robust design. The significant findings in this study are summarized in this chapter.

In **Chapter 2**, a new technique involving the simultaneous burning of candles and electrospinning was used to integrate soot particles into fibrous polymer membranes. The position of the soot particles within the polymer fibers was controlled by adjusting the injection location of the aerosol particles during electrospinning. The study demonstrated that the placement of the soot particles had no impact on the performance of photothermal conversion. When the resulting solar distillation membranes were applied to the water surface, there was a significant 194.5% improvement in heat localization compared to water samples without membranes. The membranes exhibited water evaporation and desalination rates of up to 1.60 and 1.59 $kg.m^{-2}h^{-1}$ respectively under 1-sun solar irradiation.

In **Chapter 3**, a novel approach utilizing an optical coherence tomography (OCT) system, combined with a heating chamber connected to an air pump suction line, has enabled the non-destructive and real-time observation of the penetration and evaporation of viscous liquid within porous biomass during heating. The OCT tomogram allows for the visualization of liquid movement within tobacco substrates over different time intervals, and the quantification is achieved through the attenuation coefficient of the sample at specific temperatures and times. By subjecting the time-lapse attenuation coefficient data to a statistical procedure, such as Duncan's multiple range test, we were able to estimate the transitional points during penetration and evaporation at each temperature. This analytical system provides an appealing alternative for tracking liquid transport in porous biomass under contact heating conditions, while also contributing to the comprehension of inward and outward mass transfer processes.

To conclude, this dissertation demonstrates a new way to design thin porous materials and to visualize the interaction between the thin porous materials with liquid under heating. The findings in this dissertation can aid the development of a thin porous material with rationale design.

Acknowledgements

Alhamdulillah, all praises to Allah the almighty, the most gracious, and the most merciful. Without His blessings and guidance, surely the completion of this dissertation will not be possible.

I would like to express my deepest gratitude to my supervisor, Prof. Wuled Lenggoro, for his invaluable advice and continuous support during my PhD journey. I learn a lot about seeing a wider view of things from his insights and experiences. I would like to also thank Prof. Toshiaki Iwai for his insights and caring thoughts which strengthen me during my hard times. I will always remember his undying passion for sports. Also, to Prof. Kentaro Iwami and Prof. Nobuyuki Akai, thank you for allowing me to be a part of your laboratory during my lab rotation period and for all your help to troubleshoot the problems in my research. To Prof. Godai Miyaji, Dr. Masao Gen, Dr. Nobuyuki Ishikawa, Dr. Yoshimi Hakamada, Dr. Yuji Ogawa, Dr. Hongtao Ma, and everyone in Meidensha team, I will be forever grateful for all of our talks and fruitful discussions. To Dr. Yosuke Asanuma, Ms. Tomomi Hasegawa, Mr. Mitsuki Wada, Mr. Takuma Takahashi, Mr. Keisuke Niwa, and Mr. Iori Nakaya from Lenggoro laboratory, thank you very much for helping me a lot to orient my life in Japan. I will always remember your kindness and I hope the ease you gave me will be returned to you in your every endeavor a million times more. To Dr. Mayumi Tsukada, Mr. Anca Awal Sembada, and all Lenggoro lab members whom I cannot mention one by one, thank you for all of your help during my stay in Lenggoro laboratory.

A special thanks to MEXT scholarship for the financial support I received throughout my study in Japan. I hope the finding of this research can give a little contribution back to the Japanese society.

There are no words that can describe my gratitude to both of my parents for their love, prayers, support, and their confidence in me. To my father, Mr. Muhammad Arifin Hasibuan, I really wish you were here to share this moment with me. Thank you for never stop believing in me and for never wanting to make me worry about anything even when you are actually in pain. To my mother, Ms. Nur Fathonah, thank you for your never-ending love and prayers. It is always your words that calm me in every storm I have in life, and for this, I would be forever grateful. To my sister, Adinda Nur Salsabila, thank you for your strength and bravery in facing everything that comes to our family during my absence in Indonesia.

To the sister I found in Japan, Dr. Marshila Kaha, thank you very much for all the love and caring that you have given me. I cannot imagine a day without your good words and good food. To Dr. Noraiza Suhaimi and Dr. Rasyidah Hanan, thank you for trying your best to support me in every way you can. To all the international students community in TUAT, thank you for all the joy and memories that you have given me. Life in Japan wouldn't be as enjoyable without your presence.

Appendix 1

1. Experiment to deposit hydrophobic only-, hydrophilic only-, and a mixture of hydrophobic and hydrophilic soot particles on a prefabricated PVDF membrane

Hydrophobic only-, hydrophilic only-, and a mixture of both particles were deposited onto a prefabricated PVDF membrane to check the effect of the deposition of each type of particle on the contact angle of the membrane. Different types of soot particles were obtained by varying the position of the flame relative to slide glass 1. Soot particle produced from the tip of the flame has hydrophilic property, while the one produced from the middle of the flame is hydrophobic [1]. Slide glass 1 helps to promote incomplete combustion to produce candle soot particles and to dissipate heat produced by candle flame. Heat dissipation at slide glass 1 helps to lower the deposition temperature at slide glass 2. The measured temperature at slide glass 2 after 5 minutes was ~60^{o}C. PVDF membrane was attached to the slide glass without any application of glue. The membrane could be firmly attached by the electrostatic force between the membrane and the slide glass. Soot particle deposition was conducted for 5 minutes for each experiment. The mixed hydrophobic and hydrophilic particles were introduced by adjusting the candle so that slide glass 1 could be positioned at the tip or the middle of the flame interchangeably for every 1 minute until the fourth minute, then every 30 seconds until the fifth minute. The appearance of the membrane after being deposited with soot particle with different wettability can be seen in Figure A1.2(a) and the corresponding contact angle is shown in Figure A1.2(b). The morphology of PVDF membrane after the deposition of soot particles by the method shown in Figure A1.1 is depicted in Figure A1.3. Soot particle deposition by the method shown in Figure A1.1 did not cause observable change in the morphology of the fiber's surface.

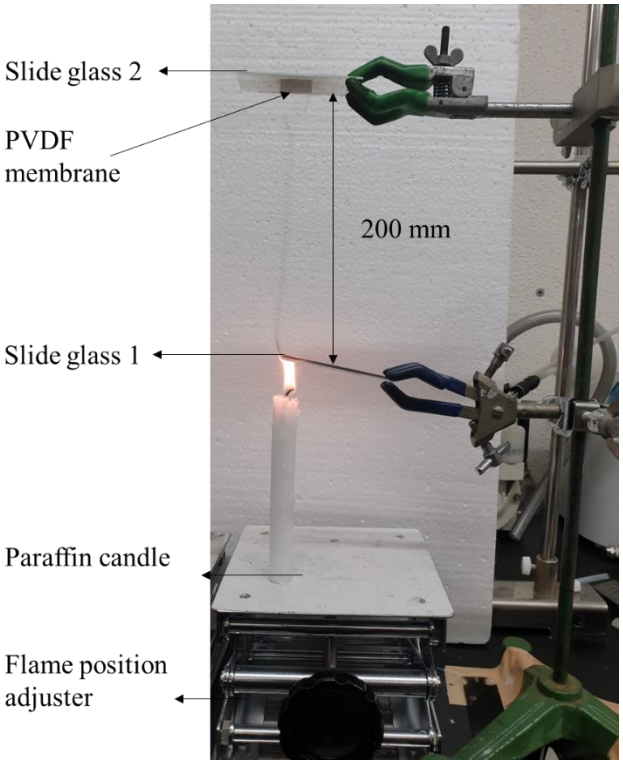

Figure A1. 1 Experiment set up to deposit hydrophobic only-, hydrophilic only-, and a mixture of hydrophilic and hydrophobic soot candle soot particles

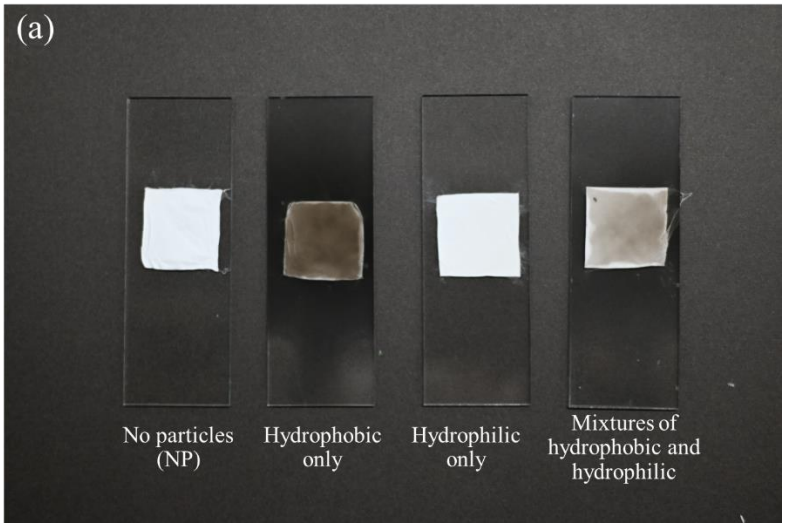

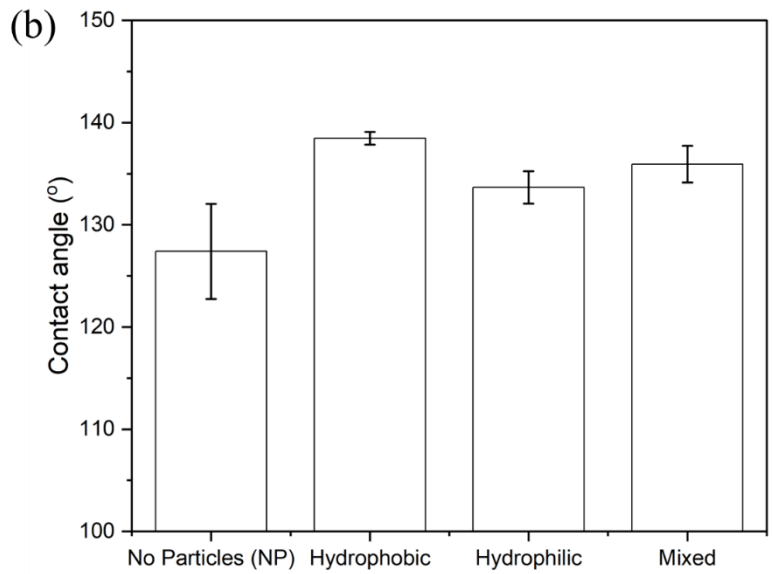

Figure A1. 2 (a) The appearance of the PVDF membrane after the deposition of soot particles, (b) Contact angle of the PVDF membrane before and after deposition of soot particles with different property

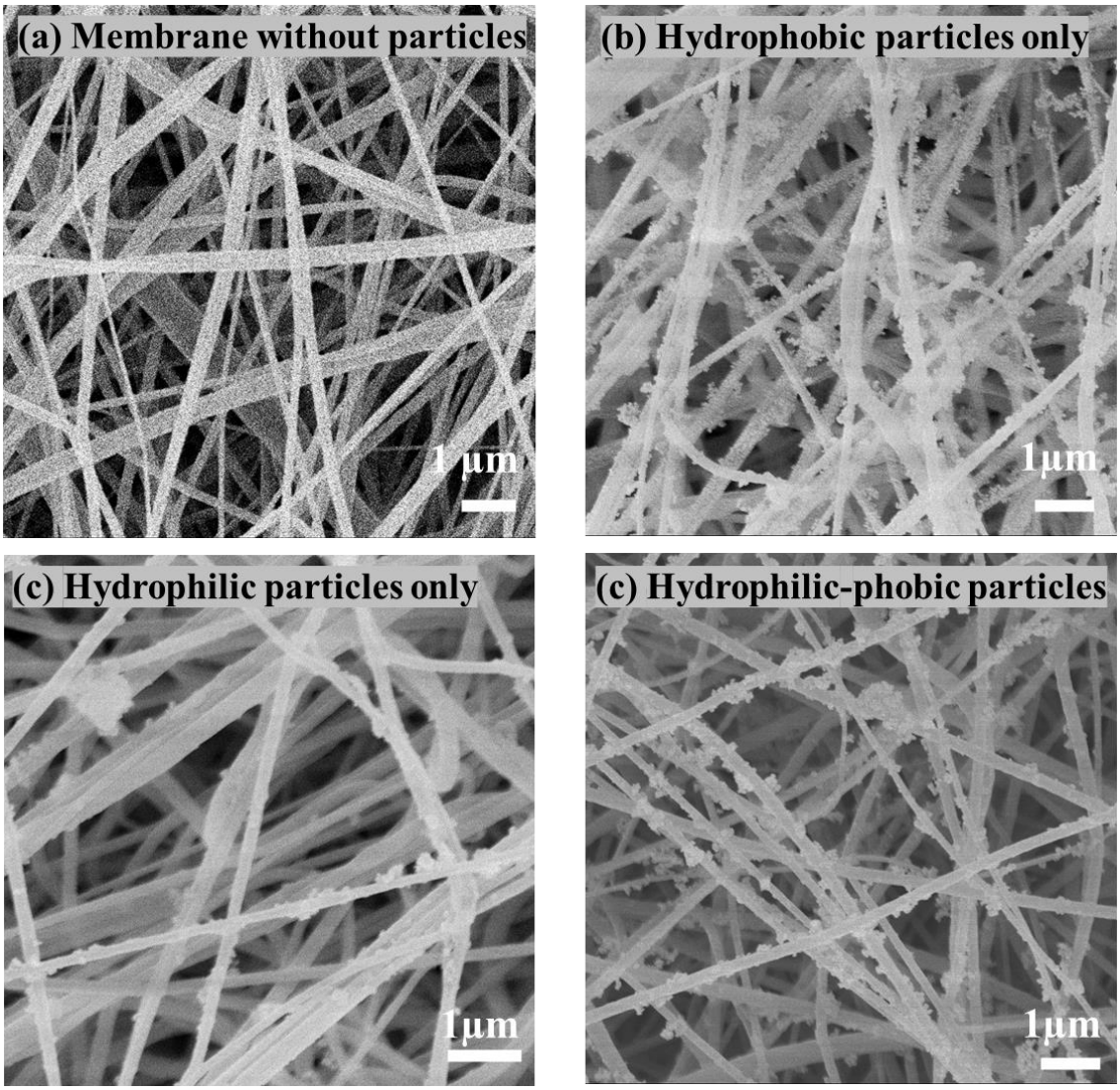

Figure A1. 3. FE-SEM micrograph of PVDF membrane after deposition of soot particles by the method shown in Figure S2

2. FE-SEM observation of the fiber's cross-section

FE-SEM observation of the fiber's cross-section was conducted to check whether the particles can be positioned at the fiber's interior. For this analysis, the flat membranes were rolled to form a cylinder. The rolled-up membranes were then immersed into liquid nitrogen to harden the structure prior to sectioning. This was done to avoid the destruction of the fibers structure due to the pressure given by the cutter. The rolled-up membranes were cut into several millimeter sections which were then fixed to a carbon tape on top of the FE-SEM stub. A layer of gold nanoparticles was coated on the samples prior to FE-SEM analysis using a sputtering device (IB-3 Ion Coater, Eiko Engineering Ltd., Japan) to enhance the sample's electroconductivity. The pictures of the membrane fixed on top of the

FE-SEM stub can be shown in figure A1.4.

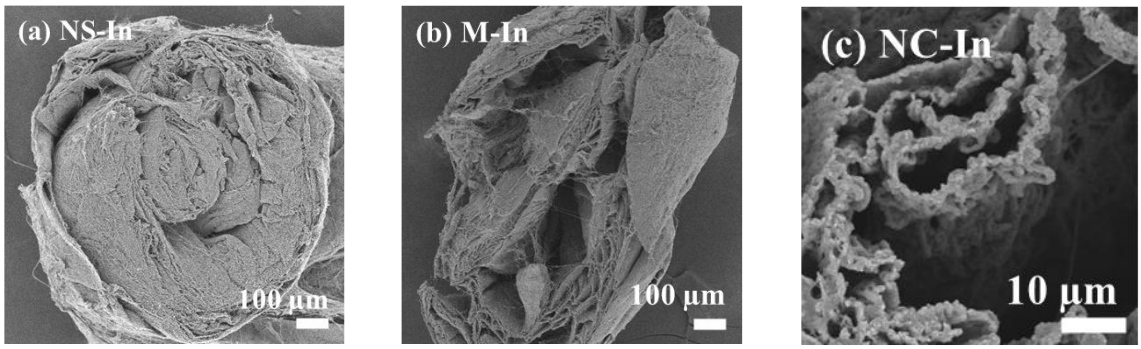

Figure A1.4. The appearance of the membranes (a: NS-In, b: M-In, c: NC-In) after being rolled up, cut, and fixed on FE-SEM stubs

As observation of particles having sizes between a few tens of nanometers to sub-micrometer in the cross-section of sub-micrometer fiber is challenging, we opted to check the presence of particles in the interior of micro-structured beads that were present in our as-fabricated membranes (Figure A1.5). The micro-meter scale size of these beads eases the process of detecting particles having sizes between a few tens of nanometers to sub-micrometer in the bead's interior. The beads were formed due to the instability of the jet in the competition between the surface tension of polymer solution and electrostatic repulsion during the electrospinning [2]. The FE-SEM observation of the bead's cross-section (Figure A1.6) shows that some particles having sizes between a few tens of nanometers to sub-micrometer are found in the bead's interior for the NS-In and M-In membranes (indicated by red arrows). As for the NC-In membrane, aggregated soot particles were found to surround the exterior of the beads) and little to none of the particles were found in the bead's interior. We believe that if particles can enter the interior of micrometer-sized polymer beads structures using our one-step membrane fabrication method, the particles can also penetrate into the interior of a sub-micrometer polymer fibers, especially for the NS- and M-membranes.

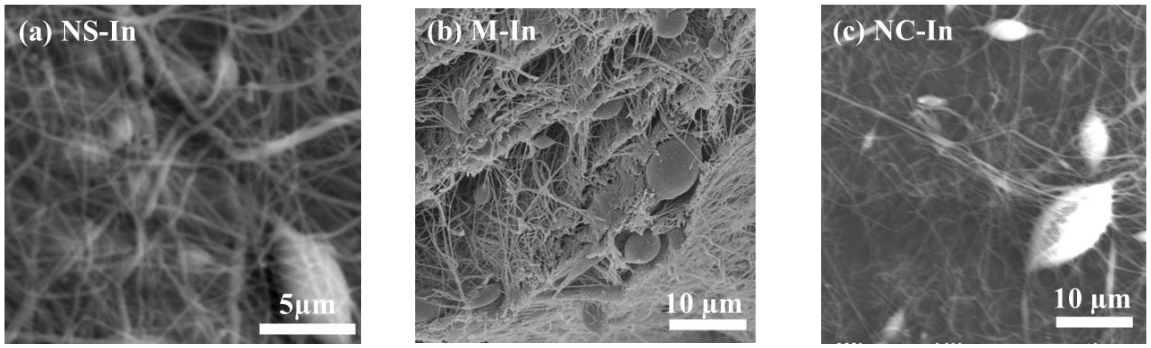

Figure A1.5. Beaded microstructures found in the membranes (a: NS-In, b: M-In, c: NC-In)

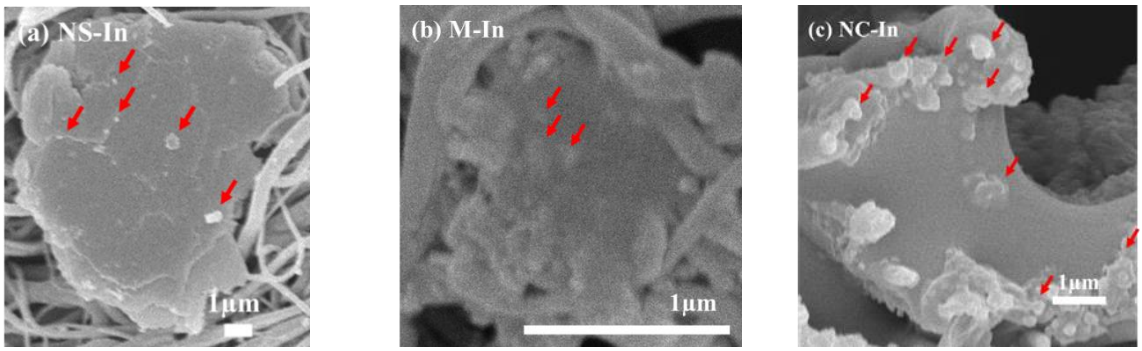

Figure A1.6. Particles having sizes between a few tens of nanometers to sub-micrometer can be found in the interior and exterior of a micrometer beads (red arrows the particles) (a: NS-In, b: M-In, c: NC-In)

3. The temperature profile at the polymer jet trajectory above the particle source (inside and outside of the membranes)

The introduction of particles directly from a burning candle elevated the temperature at the jet trajectory. The increase in temperature was measured by a T-type thermocouple connected to a data logger. The average temperature of the jet trajectory when the candle was placed inside the electrospinning chamber was 51°C. The fluctuation in the temperature was caused by the candle position adjustment by the syringe pump as well as the flickering of the candle flame. It should be noted that the candles ran out after ~20 minutes of burning, so the candles were changed around 6 times until 2 hours of electrospinning were completed. The changing of the candles also affected the temperature profile. The candles for the "Out" experiment were also changed around 6 times. However, the change did not fluctuate the temperature of the jet trajectory as much as the "In" membranes. The average temperature of the jet trajectory during the "Out" experiment was around 27°C. The "chamber" temperature shows the temperature at arbitrary point in the chamber that is not around the soot particles introduction point.

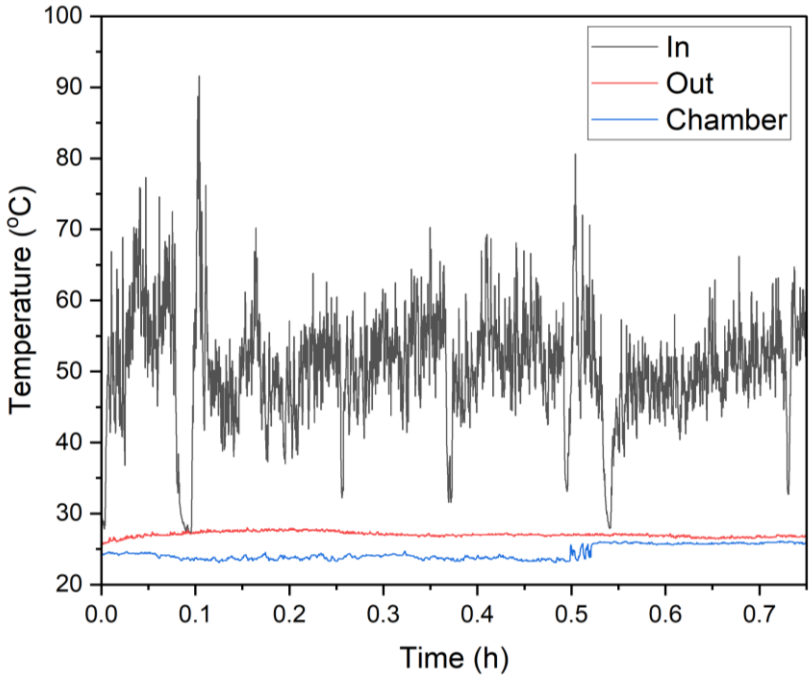

Figure A1. 7 The temperature of the jet trajectory above the source of the particles at different experiment conditions

4. Surface and bulk water temperature of each sample under the illumination of 1 sun simulated solar light

Because there were some variations at the initial temperature of the water (~1°C for both surface and bulk water temperature), a direct conclusion from Figure A1.8 cannot be drawn. The rate of surface temperature increase at every 0.1 hour time interval was calculated based on Figure A1.8 to justly characterize the photothermal conversion ability of each membrane.

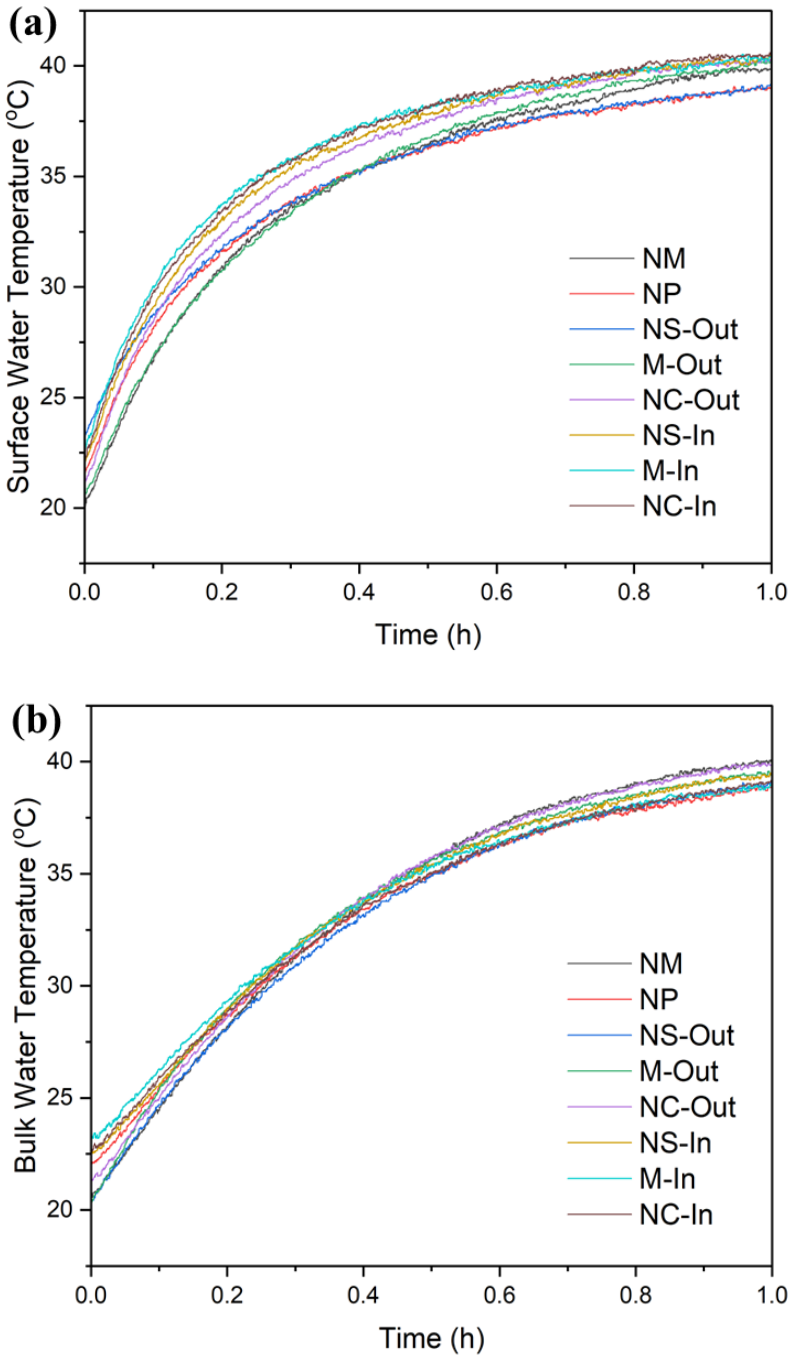

Figure A1. 8 The temperature profile of the samples under 1 sun solar light illumination; (a) surface water temperature, (b) bulk water temperature

5. Membranes' surface temperature measured by a thermal camera

The membrane's surface temperature was measured using a thermal camera, assuming that the emissivity of the membrane was around 0.95. This value is approximated from the emissivity of the soot particles produced from candle burning [3].

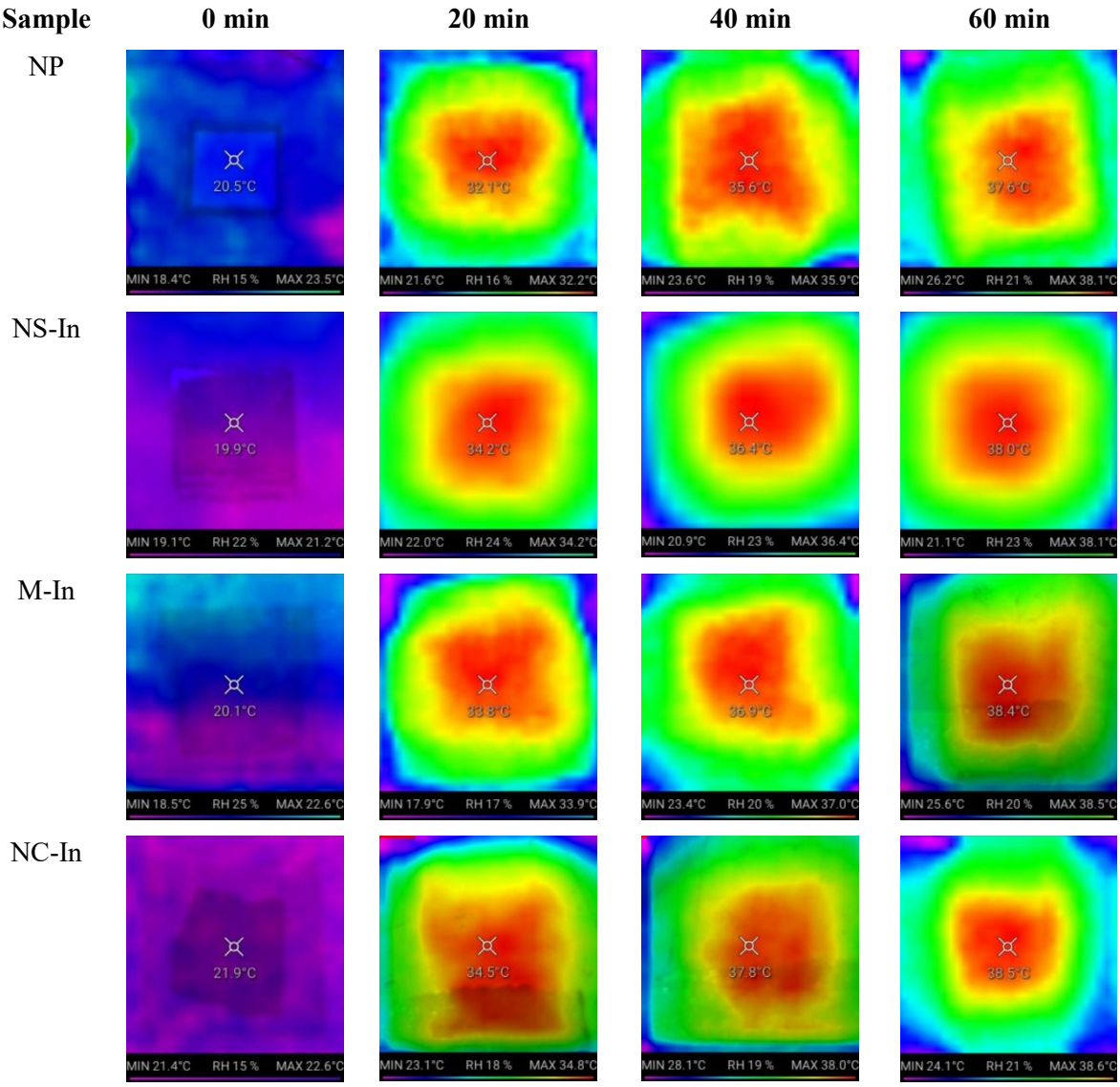

Figure A1. 9 The change of membranes' surface temperature under 1 sun of simulated solar light as captured by IR thermography

6. Electrospinning productivity as reflected by the membrane thickness

The membrane's thickness was measured using a micrometer screw with an accuracy of up to 0.01 mm. Figure A1.10 shows the thickness of each membrane. The statistical analysis result ($p \leq 0.05$) showed that the thickness of the membranes with particles produced inside the electrospinning chamber (In-membranes) have a comparable thickness as the NP membrane. However, the Out-membranes' thickness is significantly lower than the NP membrane, despite the number of particles that can modify the electric field of the polymer jet being significantly smaller than the In-membranes. The reason for this is the presence of a silicone rubber conductive tube (used for transporting particles into the electrospinning

chamber) which can strongly affect the electric field around the jet. Many of the polymer fibers were deposited around the conductive tube rather than the collector during the experiment. Reduction of the deposited polymer mass in the collector results in a thin membrane.

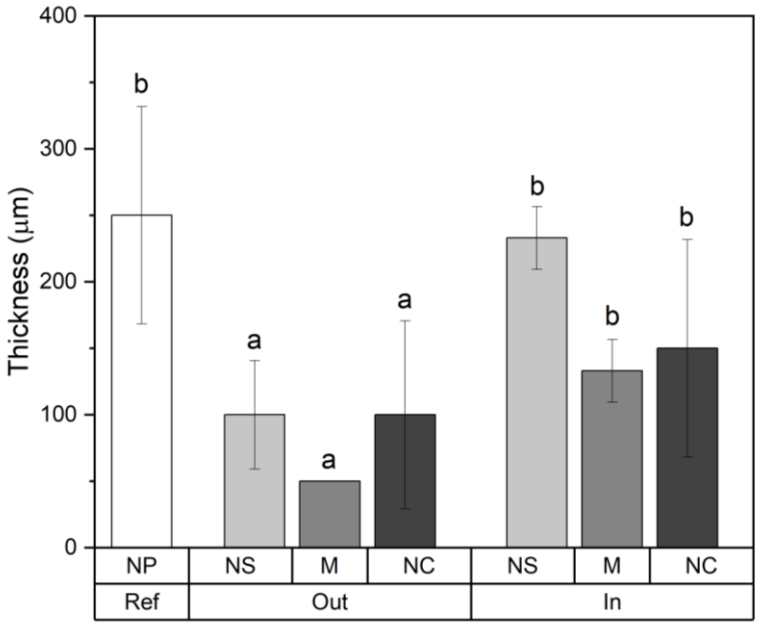

Figure A1. 10 The thickness of the electrospun membranes

A silicone rubber conductive tube was chosen as the conduit to flow particles from the funnel to the electrospinning chamber due to its flexibility, good thermal stability, and ability to prevent a build-up of charge on the tube walls, thereby reducing loss of particles due to electrostatic reason.

7. Brief summary of comparison of cycle performance of the membrane fabricated in the present study with other previous studies

Table A1.1. Comparison of cycle performance in this study and pervious studies

Matrix/ particle	Test liquid	Cycle	Evaporation rate at the end of cycle ($kg.m^{-2}.h^{-1}$)	Reference
Cotton cloth/ diesel soot	Deionized water	10	~1.5	[4]
Cotton cloth/ candle soot	Deionized water	10	~1.3	[5]
Poly-ionic monolith/	Pure water	10	-	[6]

carbon soot				
PVA sponge/ soot from camphor pellet	Water	50	~1.6	[7]
Luffa sponge/ candle soot	Freshwater	21	~1.3	[8]
PVA/ kerosene lantern soot	Distilled water	10	~1.5	[9]
Cotton/ candle soot	Deionized water	15	~1.3	[10]
Hydrogel/ diesel soot	Water	10	~3	[11]
PVDF-HFP/ graphitic carbon spheres	Salt solution 3.5 wt. %	20	~1.8	[12]
Cellulose filter/ candle soot	Salt solution	2 cycles, 8 hours	~0.8 after 8 hours, then return to ~1.2 after being let in the dark	[13]
SS mesh/ polypyrrole	Deionized water	0	n/a	[14]
PVDF fibrous matrix/ candle soot	NaCl solution 3.24 wt. %	2 cycles, 5 hours	~1.2 at the end of first cycle, then ~0.8 at the beginning until the end of second cycle	Our study

8. Analyzing particle loss from solar distillation membranes to the water body

To detect the presence of soot particles in the water sample after the evaporation test, we collected the remaining water sample (not-evaporated water sample) after each cycle of the evaporation test and analyzed the absorbance at a wavelength of 300 nm by an analytical apparatus using fluorescence in the ultraviolet range (M1000 Pro, Tecan Japan Co., Ltd.). Each water sample was ultrasonicated at 43 kHz for 5 minutes before the absorbance test to ensure the stability of soot particles, if any, in the suspension. 300 nm wavelength was chosen because all carbonaceous particles shows absorption peak at ~220 nm, 250 nm, and 300 nm along with other peaks [15]. Triplicate absorbance measurements were conducted for each test water sample. The data was then processed using Duncan's multiple range test ($p \leq 0.05$) in SPSS software (IBM SPSS Statistics Ver. 25, IBM Corp., USA) to find the condition in

which the absorbance value was significantly different from the reference sample (only distilled water without membranes). Additionally, a conversion curve was created to correlate the absorbance reading to the concentration of soot particles in the suspension. Eight suspensions with a known soot particle concentration, i.e 10^{-5}, 10^{-6}, 10^{-7}, 10^{-8}, 10^{-9}, 10^{-10}, 10^{-11}, and 10^{-12} g particles/ g distilled water were prepared to obtain absorbance data to generate a conversion curve (Figure A1.11). The equation obtained from the trendline of the conversion curve was used to convert absorbance data from each water sample into particle concentration value.

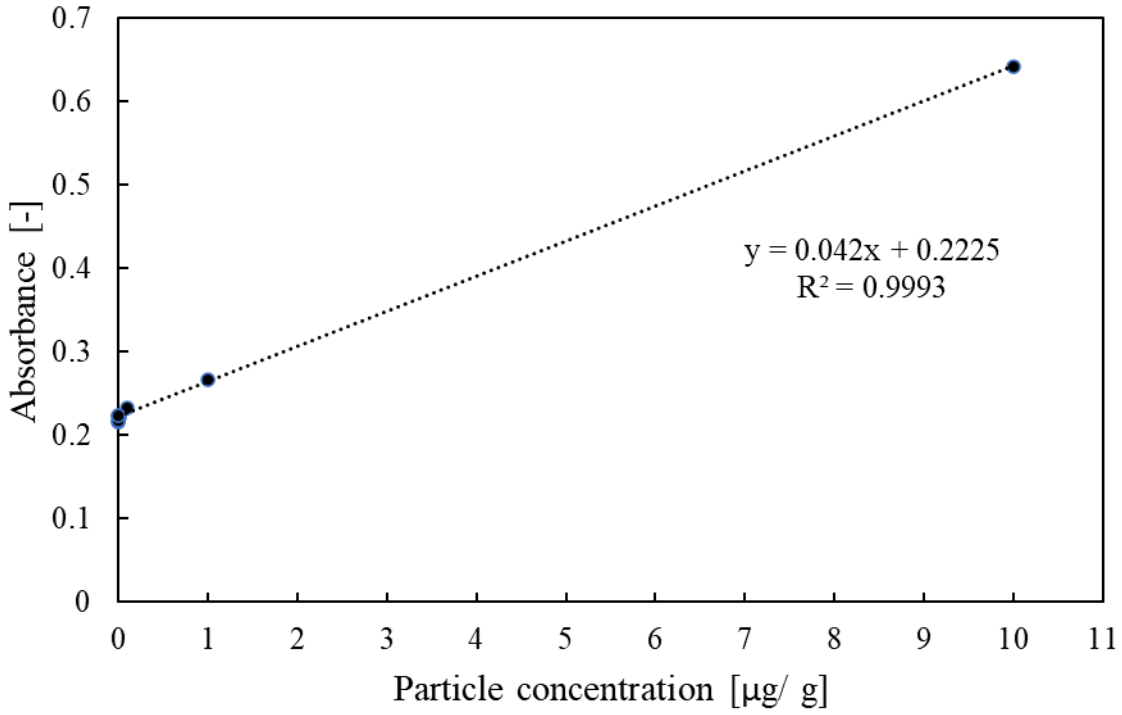

Figure A1.11. Conversion curve correlating absorbance and concentration of carbonaceous particles

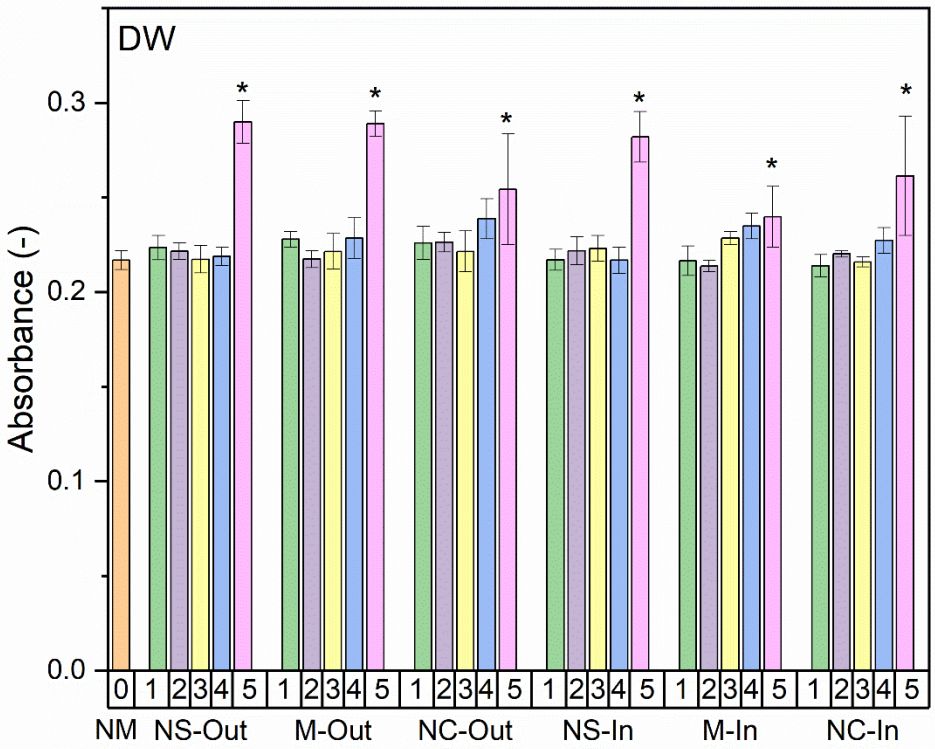

Figure A1.12. The measured absorbance from the remaining water sample (average ± SD). The star index shows the data that is significantly different from the reference (NM)

Based on statistical analysis, the absorbance value given by the reference sample (NM) is not significantly different from the absorbance value given by suspension with soot particle concentration of 10^{-8} g/g. Hence our technique can only detect the presence of soot particles with the concentration higher than 10^{-8} g/g. From statistical analysis result presented in Figure A1.12, we could observe that significant particle release was found after 5 hours of evaporation test in distilled water for all types of membranes. The absorbance data of all membranes at t=5 hours are converted into particle concentration using equation obtained in Figure A1.11. The conversion result can be seen in Figure A1.13.

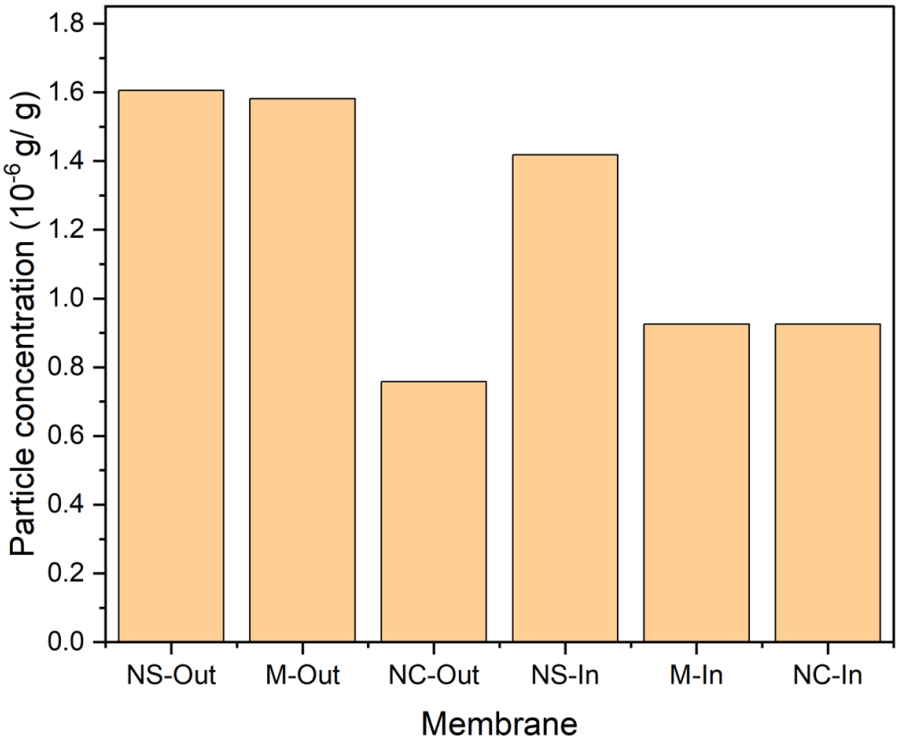

Figure A1.13. Concentration of particles detected in the remaining water sample after 5 hours of evaporation test

We were not able to establish a conversion curve for soot particles in 3.24% wt. NaCl solution due to the problems in the stability of soot particles in NaCl solution. Here we would like to provide the absorbance reading and the statistical test result for NaCl solution which was used in the two cycles of evaporation test in Figure A1.14 and A1.15. It is shown that there is a decrease in absorbance in most of the samples where significant change of absorbance was detected in comparison to the absorbance value of the reference membrane (NM). Further study is needed to obtain a conclusion regarding the decrease in absorbance in 300 nm wavelength in relation to particle release from the membrane.

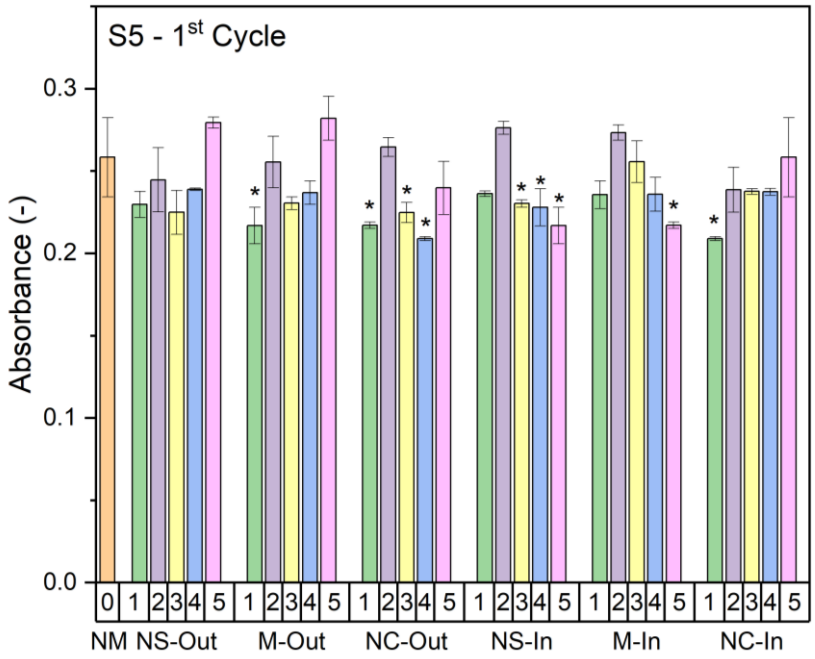

Figure A1.14. The measured absorbance from the remaining S5 solution in the first cycle (average ± SD). The star index shows the data that is significantly different from the reference (NM)

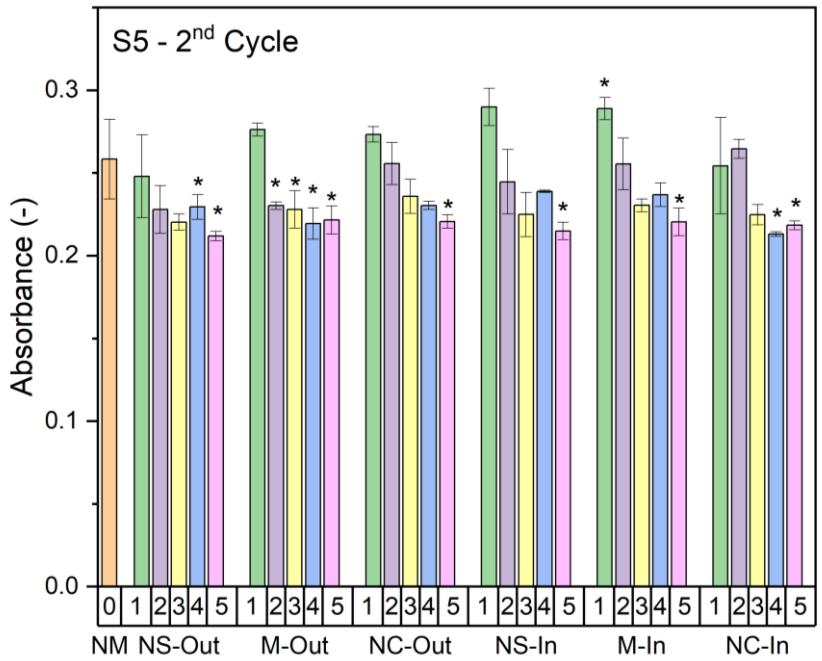

Figure A1.15. The measured absorbance from the remaining S5 solution in the second cycle (average ± SD). The star index shows the data that is significantly different from the reference (NM)

Reference

[1] F. Faizal, M.P. Khairunnisa, S. Yokote, I.W. Lenggoro, Carbonaceous nanoparticle layers prepared using candle soot by direct- and spray-based depositions, Aerosol and Air Quality Research, 18 (2018) 856–865.

[2] X. Hu, X. Chen, M. Giagnorio, C. Wu, Y. Luo, C. Hélix-Nielsen, P. Yu, W. Zhang, Beaded electrospun polyvinylidene fluoride (PVDF) membranes for membrane distillation (MD), Journal of Membrane Science, 661 (2022) 120850.

[3] J. M. Jones, P. E. Mason, and A. Williams, A compilation of data on the radiant emissivity of some materials at high temperatures, Journal of the Energy Institute, 92 (2019) 523–534.

[4] H.M. Wilson, S. Rahman A.R., A.E. Parab, N. Jha, Ultra-low cost cotton based solar evaporation device for seawater desalination and waste water purification to produce drinkable water, Desalination, 456 (2019) 85–96.

[5] H. M. Wilson, S. Rahman AR, T. Garg, and N. Jha, Recycling of hazardous diesel soot particles into a high performance solar evaporation device, Applied Surface Science, 487, (2019) 951–961.

[6] C. Xiao, W. Liang, L. Chen, J. He, F. Liu, H. Sun, Z. Zhu, A. Li, Janus Poly(ionic liquid) Monolithic Photothermal Materials with Superior Salt-Rejection for Efficient Solar Steam Generation, ACS Applied Energy Materials, 2 (2019) 8862–8870.

[7] H.M. Wilson, Tushar, S. Raheman Ar, N. Jha, Plant-derived carbon nanospheres for high efficiency solar-driven steam generation and seawater desalination at low solar intensities, Solar Energy Mateials and Solar Cells, 210 (2020) 110489.

[8] A.M. Saleque, S. Ma, S. Ahmed, M.I. Hossain, W. Qarony, Y.H. Tsang, Solar Driven Interfacial Steam Generation Derived from Biodegradable Luffa Sponge, Advanced Sustainability Systems, 5 (2021) 2000291.

[9] H. Sun, Y. Li, J. Li, Z. Zhu, W. Zhang, W. Liang, C. Ma, A. Li, Facile Preparation of a Carbon-Based Hybrid Film for Efficient Solar-Driven Interfacial Water Evaporation, ACS Applied Materials & Interfaces, 13 (2021) 33427–33436.

[10] L. Zhang, B. Bai, N. Hu, H. Wang, Low-cost and facile fabrication of a candle soot/adsorbent cotton 3D-interfacial solar steam generation for effective water evaporation, Solar Energy Materials Solar Cells, 221 (2021) 110876.

[11] H.M. Wilson, S. Raheman A. R, H.W. Lim, S.J. Lee, Conversion of Hazardous Diesel Soot Particles into a Novel Highly Efficient 3D Hydrogel for Solar Desalination and

Wastewater Purification, ACS Omega, 8 (2022) 2740-2751.

[12] W. Li, L. Deng, H. Huang, J. Zhou, Y. Liao, L. Qiu, H. Yang, L. Yao, Janus Photothermal Membrane as an Energy Generator and a Mass-Transfer Accelerator for High-Efficiency Solar-Driven Membrane Distillation, ACS Applied Materials & Interfaces, 13 (2021) 26861–26869.

[13] M.U. Rashid, Z. Tahir, S. Kim, J.I. Jang, Y.S. Kim, Selective Deposition of Candle Soot on a Cellulose Membrane for Efficient Solar Evaporation, ACS Omega, 6 (2021) 31366–31374.

[14] L. Zhang, B. Tang, J. Wu, R. Li, P. Wang, Hydrophobic Light-to-Heat Conversion Membranes with Self-Healing Ability for Interfacial Solar Heating, Advanced Materials, 27 (2015) 4889–4894.

[15] J. P. Singh, T. Nandi, S. K. Ghosh, and N. E. Prasad, Preparation and Isolation of Carbon Nanorods and ‘ Carbon Nanoflowers ’ through Combustion of Candle Wax for Heat Transfer Application, Combustion Science and Technology, 192 (2020) 1066–1087.

Appendix 2

1. The appearance of glycerol droplet on the surface of porous tobacco substrates

When the glycerol was first dropped on the surface of tobacco substrates, the glycerol formed a sessile droplet with a contact angle at the glycerol, substrate, and air interface. The droplet diameter is ~3 mm.

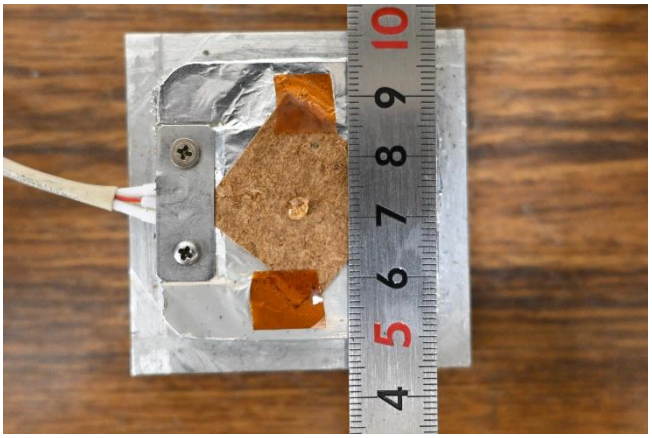

Figure A2. 1 The appearance of glycerol droplet on the surface of porous tobacco substrates

2. The evolution of glycerol droplet with elapsed time at various heating temperature

100°C	**120°C**	**200°C**
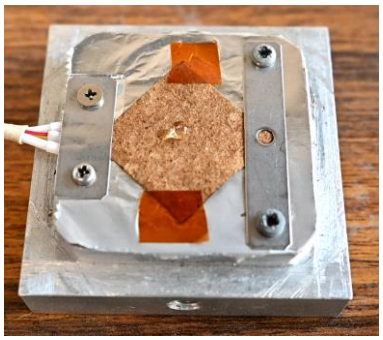	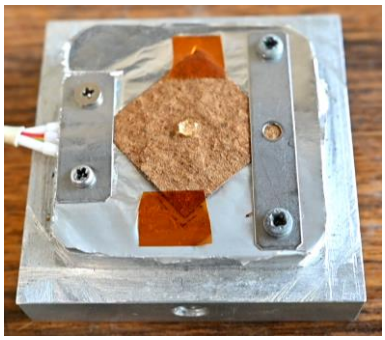	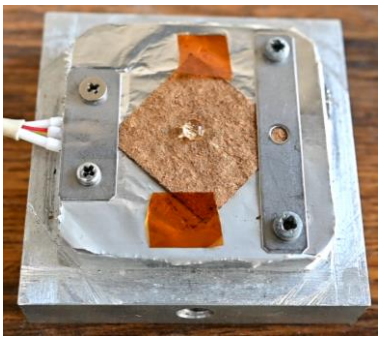
After dropping glycerol	After dropping glycerol	After dropping glycerol
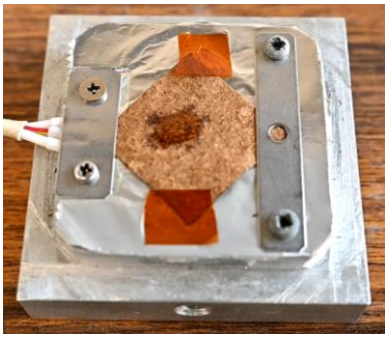	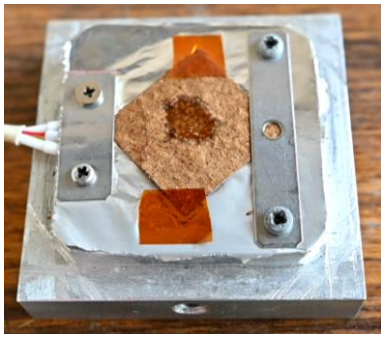	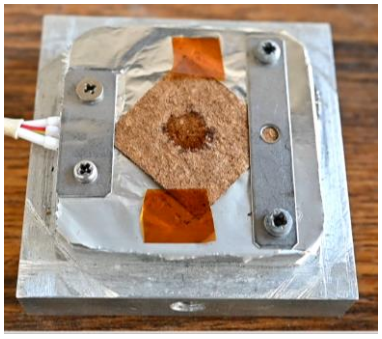

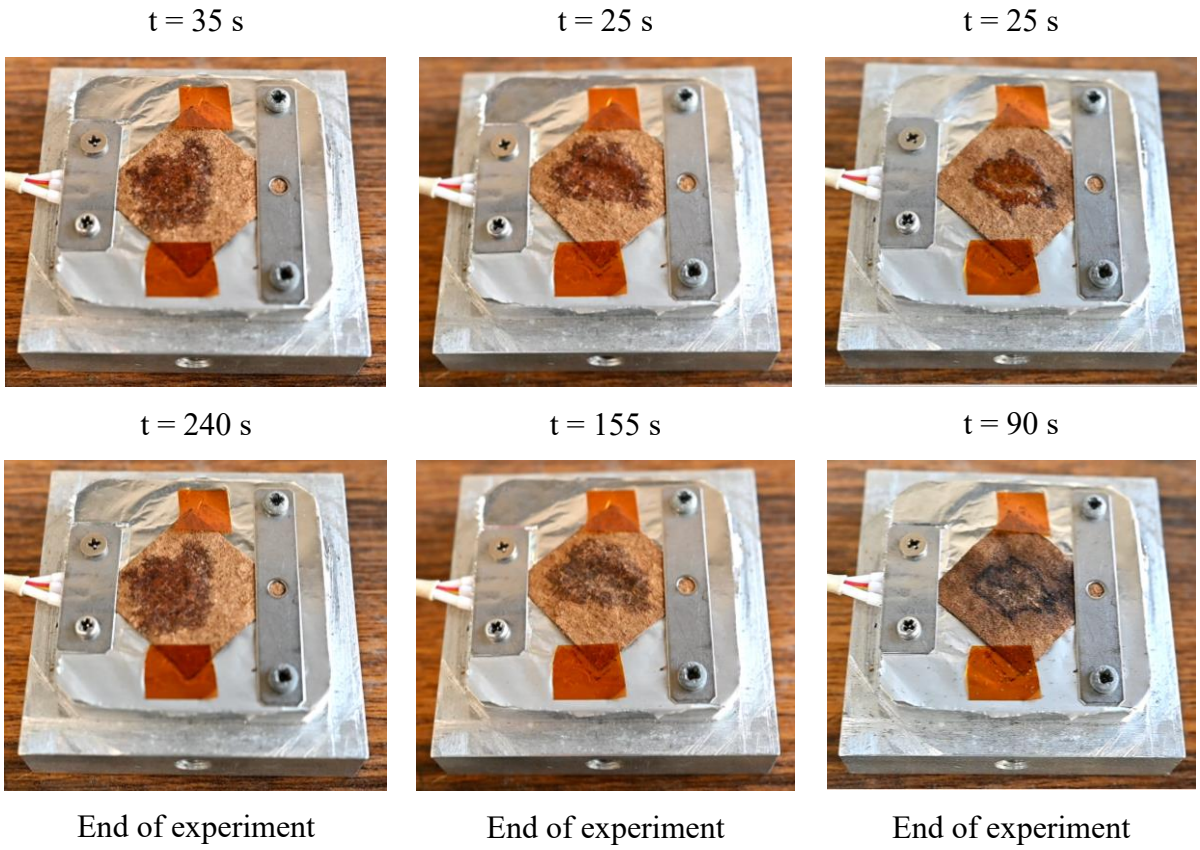

Figure A2.2 The evolution of glycerol droplet with elapsed time at heating temperature of 100, 120, and 200°C

Figure A2.2 shows the evolution of glycerol droplet with elapsed time at various heating temperatures. The contact angle at glycerol, substrate, and air interface becomes unobservable by a video camera at 35 s for 100°C and 25 s for 120 and 200°C. The video camera observation shows the in-plane spreading of glycerol on the substrate. The maximum spreading surface area of glycerol was reached after 240, 155, and 90 s for heating temperatures of 100, 120, and 200°C. A change of colour into darker brown was observed at the end of the experiment of tobacco substrate heating at 200°C.